Technische Universität München

TUM School of Engineering and Design

Process-Property Relationships in Material Extrusion Additive Manufacturing

Patrick Henry Consul

Vollständiger Abdruck der von der TUM School of Engineering and Design der Technischen Universität München zur Erlangung des akademischen Grades eines

Doktors der Ingenieurwissenschaften (Dr.-Ing.)

genehmigten Dissertation.

Vorsitz:

Prof. Dr.-Ing. Gisela Detrell Domingo

Prüfende der Dissertation:

1. Prof. Dr.-Ing. Klaus Drechsler
2. Prof. Oana Ghita, Ph.D.

Die Dissertation wurde am 14.05.2025 bei der Technischen Universität München eingereicht und durch die TUM School of Engineering and Design am 29.10.2025 angenommen.

Technische Universität München
TUM School of Engineering and Design
Lehrstuhl für Carbon Composites
Boltzmannstraße 15
D-85748 Garching bei München

Tel.: +49 (0) 89 / 289 – 15092
Fax.: +49 (0) 89 / 289 – 15097
Email: info.lcc@ed.tum.de
Web: www.asg.ed.tum.de/lcc

ACKNOWLEDGEMENTS

When I first embarked on this PhD journey, I saw it as a stepping stone toward a career in a large corporation. It seemed like the logical progression—a solid academic foundation leading to a structured, well-defined role in industry. But over the course of these seven years, I learned and grew in ways I hadn't anticipated. The scientific discoveries were, of course, important, but just as transformative was the realisation that I thrived in the freedom of research. As long as I could secure the necessary funding, I had the autonomy to explore what I found interesting. What once seemed like a natural career trajectory started to feel limiting, and I realized that the autonomy and creativity I have experienced during my PhD are things I'm not willing to give up anymore.

This journey led to the founding of a company together with my colleagues, Benno Böckl and Ting Wang. What started as academic exploration has now become a business, evolving the target metrics from the citations and papers written to revenue generated and successful customers. None of this would have been possible without the many people who supported me, both scientifically and personally, through all the ups and downs.

Academically, I owe a great deal to those who guided, challenged, and encouraged me. Prof. Klaus Drechsler, my doctoral supervisor, provided the freedom and resources to explore topics that were new to me and to the institute itself. Thomas Wettemann, who first supervised my master's thesis and later brought me to the institute, played a key role in my journey and continued to support me as a group leader towards the end of my time there. Dr. Swen Zaremba, my initial group leader, remained a mentor even after stepping into his role as deputy head of the institute. He introduced me to his network and, more importantly, taught me how to build consortia and secure funding—a valuable lesson that is now proving just as useful in sales. Prof. Oana Ghita, who graciously agreed to mentor my thesis, brought deep expertise and thoughtful discussions that helped shape my research. Beyond formal supervision, my colleagues in the field were instrumental in shaping my thinking through countless discussions—whether over coffee, beer, in hallways, meetings, or the lab. I am grateful to Matthias Feuchtgruber, Alexander Matschinski, Bernhard Bauer, Nevine Tagscherer, Dominik Leubecher, Luciano Avila Gray, Daniel Amrein and many others for the camaraderie, debates, and shared frustrations that made the journey all the more enriching.

My work would not have been possible without financial support, and I am grateful to the European Commission, which funded part of my research through a CleanSky2 project in the Horizon 2020 program, as well as the Bavarian Ministry of Economic Affairs, Regional Development, and Energy, which supported another project in the "Bayrisches Verbundforschungsprogramm." Their support enabled me to pursue research freely and develop ideas that have now evolved into something beyond academia.

On a more personal note, I want to thank my parents, Waltraud & Heinz Consul, for supporting me throughout my education, enabling me to pursue my studies and encouraging me along the way. I'm sure they weren't initially thrilled about the PhD—probably suspecting it was an elaborate excuse to avoid getting a "real job"—but they never showed anything but support. A special thank you goes to Diana Weichert, who has been by my side since my master's thesis. She has patiently endured years of weekends lost to analysing results, making diagrams, or writing papers. Often postponing activities and vacations because it was always a "really critical phase right now". Often picking up the slack at home while I was buried in research. Her patience and unwavering support have meant more than I can express.

This PhD has been an unforgettable chapter of my life, one I will always look back on fondly, made possible by the contributions, big and small, of so many people. But while it has been a rewarding journey, I think everyone involved, myself included, is relieved that it is finally over. I suspect some may have even started to believe it never would. Now, a new chapter begins, and I look forward to the next challenges ahead.

ABSTRACT

Additive Manufacturing, especially Material Extrusion, is evolving from a prototyping tool into a scalable technology capable of producing functional, high-performance components. Material Extrusion allows for the layer-by-layer deposition of thermoplastics and fibre-reinforced composites, providing design freedom, cost efficiency, and waste reduction. However, challenges such as mechanical anisotropy, incomplete interlayer bonding, and complex crystallisation behaviour continue to hinder industrial adoption.

This dissertation addresses these challenges by exploring the process-property relationships influencing fibre alignment, interlayer bonding, and crystallisation kinetics in Material Extrusion. It examines both the behaviour of fibres in the melt flow and the dissolution of layer interfaces during the welding of the matrix between the layers of the short fibre-reinforced composite material.

The research demonstrates that shear rates in the melt flow play a critical role in fibre alignment, with optimal rates enhancing strength and stiffness. In contrast, excessive shear rates can result in misalignment and surface defects.

The study employs the fusion bonding model to analyse the highly non-isothermal nature of the Material Extrusion process. It validates its predictions by using mechanical relaxation time to forecast welding outcomes. It introduces the concept of pseudo-amorphous polymer behaviour, showing that because of it, superior interlayer bonding develops under sub-melting conditions, which results in a higher degree of healing through delayed crystallisation.

These findings support theoretical models and provide actionable guidelines for process optimisation by focusing on shear rates, substrate temperatures, and deposition power. Recommendations for process enhancement and machine design to reduce anisotropy and improve mechanical performance are derived from the results.

It emphasises the industrial applications of Material Extrusion in the aerospace, automotive, and medical sectors. Specific applications include composite tooling, lightweight automotive components, and biocompatible implants, where Material Extrusion's unique advantages help meet performance and sustainability goals.

This work advances the theoretical understanding of extrusion dynamics, bonding mechanisms, and crystallisation behaviour, bridging gaps between academic models and industrial practice. The work shows that, by keeping the melt flow shear rates in a process window, the mechanical strength and stiffness along the extrusion lines can be maximised, and that pseudo-amorphous polymer behaviour can be exploited to improve the welding of the layers. Both aspects improve the mechanical properties and the Material Extrusion process's repeatability, reliability and robustness. The proposed framework establishes a foundation for the broader adoption of Material Extrusion in producing customised, high-performance, and sustainable components.

KURZZUSAMMENFASSUNG

Die additive Fertigung, insbesondere die Materialextrusion, entwickelt sich von einem Werkzeug für den Prototypenbau zu einer skalierbaren Technologie, mit der funktionale Hochleistungskomponenten hergestellt werden können. Die Materialextrusion ermöglicht das schichtweise Auftragen von Thermoplasten und faserverstärkten Verbundwerkstoffen und bietet damit Designfreiheit, Kosteneffizienz und Abfallreduzierung. Herausforderungen wie mechanische Anisotropie, unvollständige Zwischenschichtbindungen und komplexes Kristallisationsverhalten behindern jedoch nach wie vor die industrielle Anwendung.

Diese Dissertation befasst sich mit diesen Herausforderungen, indem sie die Prozess-Eigenschafts-Beziehungen untersucht, die die Faserausrichtung, die Zwischenschichtbindung und die Kristallisationskinetik bei der Materialextrusion beeinflussen. Untersucht werden sowohl das Verhalten der Fasern im Schmelzfluss als auch die Auflösung der Schichtgrenzen während des Verschweißens der Matrix zwischen den Schichten des kurzfaserverstärkten Verbundwerkstoffs.

Die Ergebnisse zeigen, dass die Scherraten im Schmelzfluss eine entscheidende Rolle bei der Faserausrichtung spielen, wobei optimale Raten die Festigkeit und Steifigkeit erhöhen. Im Gegensatz dazu können zu hohe Schergeschwindigkeiten zu Fehlausrichtungen und Oberflächenfehlern führen.

In der Studie wird das “Fusion Bonding” Modell verwendet, um den stark nicht-isothermen Materialextrusionsprozess zu analysieren. Die Vorhersagen wurden validiert, indem die mechanische Relaxationszeit zur Vorhersage von Schweißergebnissen verwendet wurde. Die Studie führt das Konzept des pseudo-amorphen Polymerverhaltens ein und zeigt, dass dadurch eine bessere Zwischenschichtbindung auch unterhalb der Schmelztemperatur entsteht, was zu einem höheren Heilungsgrad durch verzögerte Kristallisation führt.

Diese Ergebnisse stützen theoretische Modelle und liefern umsetzbare Leitlinien für die Prozessoptimierung, wobei der Schwerpunkt auf Scherraten, Substrattemperaturen und Auftragsleistung liegt. Aus den Ergebnissen werden Empfehlungen für die Prozessverbesserung und den Maschinenentwurf zur Verringerung der Anisotropie und zur Verbesserung der mechanischen Leistung abgeleitet.

Der Schwerpunkt liegt auf den industriellen Anwendungen der Materialextrusion in den Bereichen Luft- und Raumfahrt, Automobilbau und Medizin. Zu den spezifischen Anwendungen gehören Werkzeuge aus Verbundwerkstoffen, leichte Automobilkomponenten und biokompatible Implantate, bei denen die einzigartigen Vorteile der Materialextrusion dazu beitragen, Leistungs- und Nachhaltigkeitsziele zu erreichen.

Diese Arbeit trägt zum theoretischen Verständnis der Extrusionsdynamik, der Bindungsmechanismen und des Kristallisationsverhaltens bei und schließt die Lücke zwischen

akademischen Modellen und der industriellen Praxis. Die Arbeit zeigt, dass die mechanische Festigkeit und Steifigkeit entlang der Extrusionslinien maximiert werden kann, indem die Schmelzfluss-Scherraten in einem Prozessfenster gehalten werden, und dass das pseudo-amorphe Polymerverhalten zur Verbesserung der Verschweißung der Schichten genutzt werden kann. Beide Aspekte verbessern die mechanischen Eigenschaften sowie die Wiederholbarkeit, Zuverlässigkeit und Robustheit des Materialextrusionsprozesses. Der vorgeschlagene Rahmen bildet die Grundlage für eine breitere Anwendung der Materialextrusion bei der Herstellung maßgeschneiderter, leistungsstarker und nachhaltiger Komponenten.

Table of Contents

Nomenclature

Symbol	Unit	Description
a	mm	Contact width of extrusion line
α	%	Choe & Lee rate of crystallisation
α_{het}	%	Choe & Lee rate of heterogeneous crystallisation
α_{hom}	%	Choe & Lee rate of homogeneous crystallisation
A	s	Fusion Bonding, VFT relationship, constant
A_d	mm²	Area of extrusion line cross-section
A_e	mm²	Area of nozzle orifice
B	-	Fusion Bonding, VFT relationship, constant
C		Fusion Bonding, intimate contact, constant of surface structure
c_p		Specific heat capacity
D	mm	Nozzle diameter
D_b	%	Fusion Bonding, degree of bonding
D_h	%	Fusion Bonding, degree of healing
D_{ic}	%	Fusion Bonding, degree of intimate contact
E_a	J/mol	Choe & Lee activation energy for homogeneous crystallisation
E_d	J/mol	Choe & Lee activation energy for heterogeneous crystallisation
η''	Pa s	Rheology, complex viscosity, loss component
G'	Pa	Rheology, loss modulus
G''	Pa	Rheology, storage modulus

Symbol	Unit	Description
$\dot{\gamma}_{xz}$	s^{-1}	Shear rate in XZ plane
h	mm	Layer height
H	J/g, or J	Enthalpy
$H_{10\,K\,min-1}$	J/g	Melting enthalpy measured after cooling at 10 K/min
H_m	J/g	Melting enthalpy
$H_{Specimen}$	J/g	Melting enthalpy measured in specimen
k	s^{-n}	Avrami crystallisation rate constant at the specific temperature
k_1	s^{-1}	Choe & Lee rate constant 1
k_2	m/s	Choe & Lee rate constant 2
k_ϕ	s^{-m}	Fusion Bonding, intimate contact, wetting spreading constant
K_0	K/s^n	Avrami crystallisation rate constant, temperature dependent
m	-	Ozawa exponent
m_ϕ	-	Fusion Bonding, intimate contact, wetting, spreading behaviour exponent
M	g/mol	Molar mass
M_c	g/mol	Critical molar mass
M_e	g/mol	Entanglement molar mass
μ_{mf}	Pa s	Fusion Bonding, intimate contact, fibre-matrix viscosity
n	-	Avrami exponent
n_d	-	Avrami exponent for crystal dimension

Symbol	Unit	Description
n_n	-	Avrami exponent for nucleation type
ω	rad/s	Rheology, angular frequency
P	Pa	Fusion Bonding, intimate contact, pressure field function
ϕ	%	Fusion Bonding, intimate contact, wetting function
ψ_1	s^{-1}	Choe & Lee material parameter 1
ψ_2	s^{-1}	Choe & Lee material parameter 2
r	mm	Radius of bead edge
R	J mol^{-1} K^{-1}	Gas constant
R_A	µm	Line roughness, average
ρ	kg/m³	Density
S_A	µm	Surface roughness, average
σ	MPa	Strength
t	s	Time
t_{onset}	s	Time to crystallisation onset
t_{rep}	s	Fusion Bonding, reptation time
t_m	s	Fusion Bonding, mechanical relaxation time
T	K or °C	Temperature
T_0	K or °C	Fusion Bonding, VFT relationship, threshold temperature
T_∞	K or °C	Choe & Lee crystallisation stopping temperature
T_c	K or °C	Crystallisation temperature

Symbol	Unit	Description
$\dot{T}_{crit}$	K/s or K/min	Critical cooling rate that supresses crystallisation
T_g	K or °C	Glass transition temperature
T_m	K or °C	Melting temperature
v_e	mm/s	Extrusion velocity
v_d	mm/s	Deposition velocity
$\dot{V}$	mm³/s	Volume flow rate
X_r	%	Relative degree of crystallinity
X_{Thr}	%	Threshold for degree of crystallinity

Abbreviations

Abbreviation	Description
ABS	Acrylonitrile butadiene styrene
AM	Additive manufacturing
CAD	Computer aided design
CF	Carbon fibre
CO2	Carbon dioxide
CTE	Coefficient of thermal expansion
DIC	Digital image correlation
DSC	Differential scanning calorimetry
FC	Fast crystallising, used for material classification
FDM	Fused Deposition Modelling, trademark by Stratasys
FFF	Fused Filament Fabrication
GF	Glass fibre
I	Isophthaloyl, kinked, meta substitution in PEKK
IC	Intermediately crystallising, used for material classification
IR	Infrared
LFAM	Large format additive manufacturing
LM-PAEK	Low melting polyaryletherketone
MEX	Material extrusion
PAEK	Polyaryletherketone
PBF	Powder Bed Fusion
PC	Polycarbonate

Abbreviation	Description
PEEK	Polyetheretherketone
PEI	Polyetherimide
PEKK	Polyetherketoneketone
PESU	Polyethersulfone
PETG	Polyethyleneterephthalate-Glycol
PP	Polypropylene
PU	Polyurethane
SC	Slow crystallising, used for material classification
T	Terephthaloyl, straight, para substitution in PEKK
VFT	Vogel-Fulcher-Tamman
X	Direction tangential of toolpath
XY	Plane of X and Y, layer plane
XZ	Plane of X and Z, wall plane
Y	Direction perpendicular of toolpath in layer plane
Z	Direction perpendicular to layer plane

List of Figures

List of Tables

1 Introduction

Additive Manufacturing (AM), once synonymous with "3D printing," is evolving from its initial image as a rapid prototyping tool into a versatile, mature technology capable of producing functional end-use components. The growing preference for the term "Additive Manufacturing" over "3D printing" signifies a shift from consumer-oriented goals to advancements relevant to the industry. This change is now also starting in Material Extrusion AM (MEX), where scalability, process precision, and materials engineering are crucial for achieving widespread industrial adoption.

MEX, particularly in large-format applications, presents unique opportunities and challenges. This method allows for the layer-by-layer deposition of high-performance thermoplastics and fibre-reinforced composites, enabling users to create large, customised components at lower costs and reduced lead times compared to traditional subtractive manufacturing. However, a significant barrier to achieving isotropic mechanical performance is the mechanical anisotropy of MEX-manufactured parts. This anisotropy arises from fibre misalignment, incomplete interlayer bonding, and complex crystallisation behaviour. To overcome these limitations, it is essential to understand how extrusion dynamics, interlayer diffusion, and phase transitions impact the material properties of printed components.

This dissertation addresses the critical need to quantify and optimise the process-property relationships that determine MEX part prop

erties. By linking theoretical considerations with experimental findings, this research proposes a comprehensive framework for optimising MEX process parameters and advancing the production of mechanically robust, functional components.

1.1 Research Objectives

This thesis aims to understand the relationships between MEX process parameters and the resulting material properties, focusing on fibre alignment, interlayer bonding, and crystallisation behaviour. Specifically, the work addresses three interrelated hypotheses:

1. Material Flow Behaviour and Fiber Alignment: Jeffery's equation predicts fibre alignment within the extrusion line cross-section from the occurring shear rate.
2. Interlayer Bonding and Mechanical Relaxation: The mechanical relaxation time of polymers approximates the time required for molecular diffusion during interlayer bonding, with a temperature dependence that follows a Vogel-Fulcher-Tammann (VFT) relationship.

3. Crystallisation Kinetics and Low-Temperature Bonding**:** Pseudo-amorphous polymers can achieve robust interlayer bonding at temperatures below their melting point, provided the cooling rate delays crystallisation.

By addressing these hypotheses, this research seeks to better understand how MEX parameters can be adjusted to reduce anisotropy, enhance interlayer adhesion, and utilise pseudo-amorphous behaviour for improved part performance.

1.2 Outline

Chapter 2: State of the Art in Material Extrusion AM provides an overview of MEX technologies, including large format additive manufacturing (LFAM), the challenges associated with processing thermoplastics and fibre-reinforced composites, as well as the current limitations in achieving isotropic mechanical properties.

Chapter 3: Theoretical Considerations introduces the relevant theoretical models, including extrusion flow mechanics, fibre alignment theory, crystallisation kinetics, and fusion bonding models.

Chapter 4: Experimental Design outlines the hypotheses, research approach, and experimental methodology, detailing the material selection, sample preparation, and testing methods used to investigate the process-property relationships in MEX.

Chapter 5: Experimental Results and Discussion presents and interprets the experimental findings, focusing on how variations in shear rates, temperature profiles, and rheological properties influence fibre alignment, bonding strength, and crystallisation behaviour.

Chapter 6: Discussion compares the theoretical and experimental insights, linking key findings to practical guidelines for optimising MEX process settings. This chapter also explores implications for future process and machine design.

Chapter 7: Conclusion and Outlook summarises this research's contributions, emphasising the findings' relevance and originality in advancing the industrial adoption of MEX.

In summary, this dissertation contributes to the evolution of extrusion-based AM by addressing the fundamental challenges that limit its mechanical performance. A systematic exploration of flow dynamics, interlayer diffusion, and crystallisation suppression aims to provide actionable insights that support the broader goal of producing high-performance, fibre-reinforced thermoplastic components for industrial applications.

2 State of the Art in Material Extrusion

AM, as direct automated manufacturing from digital model data to physical parts without moulds, dies, or workpieces, promises significant benefits for the production and the product. Some of the benefits to the supply chain, the design & engineering or production, often reported in the literature, include:

- Economies of scope, low cost for parts already for small production volumes or individual production [1], [2], [3], [4], [5], [6], [7], [8]
- Freedom of design and complexity [1], [2], [3], [8], [9], [10]
- Smart materials, embedded components & functionalisation [1], [2], [8], [10], [11]
- Mass customisation [2], [5], [6], [8]
- Tool and mould-free production with reduced lead times [2], [4], [6], [8]
- Part consolidation by printed assemblies [2], [9], [10], [11]
- Highly efficient process with low material waste and lightweight designs [1], [2], [8]

Lower costs, faster lead times, scale effects from single-piece production, digital inventories, waste-free production in the supply chain and integrated, smarter products down to the material all together promised to be the next industrial revolution that, at the height of the hype cycle, many believed it to be.

AM started as early as 1984 with Charles Hull's Stereolithography, the namesake of the STL data format used to this day, used by early adopters for accurate prototypes and even master patterns for investment casting. It was followed in 1988 by Scott Crump's Fused Deposition Modelling (FDM), offering design validation and proof-of-concept models without the hazardous resin vats of Stereolithography. Powder Bed Fusion (PBF) appeared a year earlier, in 1987, and was first used as Selective Laser Sintering of thermoplastics, the first of the technologies to be used for functional parts. PBF likely kicked off the hype in 2015, when GE Aviation started serial production of fuel nozzles using Direct Metal Laser Sintering, replacing an assembly of 20 parts with a single printed piece, offering higher performance at lower weight.

Charles Hull and Scott Crump had separately founded "3D Systems" and "Stratasys", commercialising their inventions, and both IPO'd in 1994. However, it wasn't until the breakthrough of GE kicked off the hype by announcing its plan for the fuel nozzle 2012-

2013 that the company valuations peaked, as seen in the market capitalisation charts of Figure 2-1 and Figure 2-2 below.

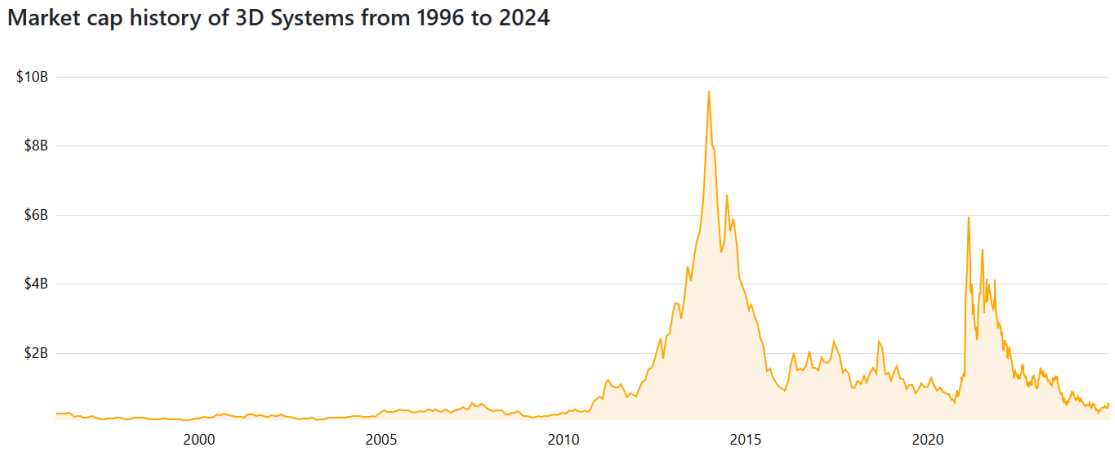

Figure 2-1: Historical market capitalisation of 3D Systems from companiesmarketcap.com [12]

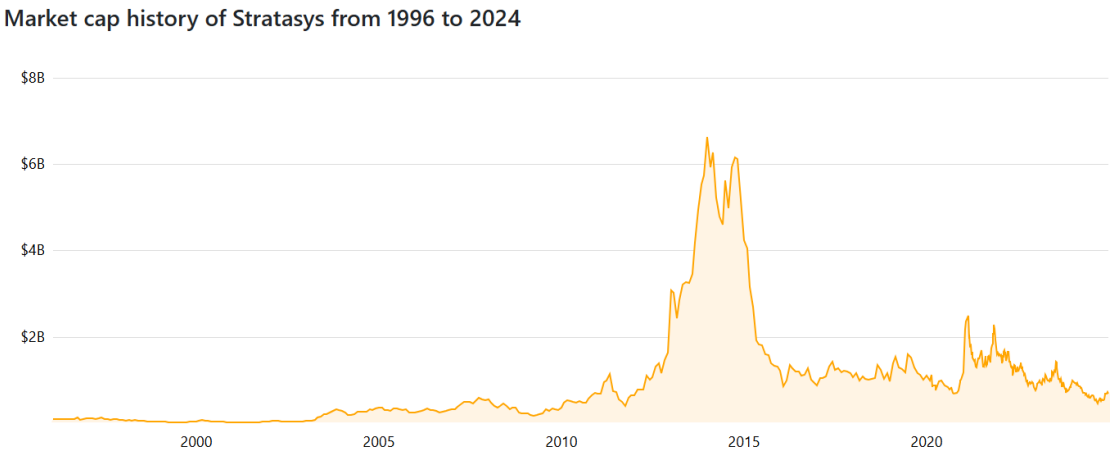

Figure 2-2: Historical market capitalisation of Stratasys from companiesmarketcap.com [13]

Both companies benefitted from the expectations that AM technologies would be transitioning into high-value serial production, offering all the benefits listed above. However, the market soon corrected when GE's results showed neither company's technology could serve the application.

With increasing globalisation and economies of scale outpricing AM's economies of scope, the technologies stayed in their trough of disillusionment until, in 2020, the COVID-19 pandemic put a sudden end to global supply chains. With hopes of AM's strengths offering decentralised production, expectations peaked again, only to be disillusioned with the technologies not being able to replace the world's production chains in the short or mid-term. Even though more and more viable production niches were identified, large-scale adoption still did not occur.

Nano Dimension, a technology provider on the stock exchange, went public at the end of the first hype cycle in 2015. It built on the momentum of the 2020 hype by success-

fully printing electronic components for the defence company Hensoldt AG and announcing a joint venture in 2021. However, even Nano Dimension has been unable to spark an industrial revolution. Despite having a trifecta of proprietary technology, high-value and high-tech applications, and a market shift towards decentralised production, Nano Dimension has faced challenges in realising its potential, and the markets have re-evaluated their expectations for these three technology pioneers.

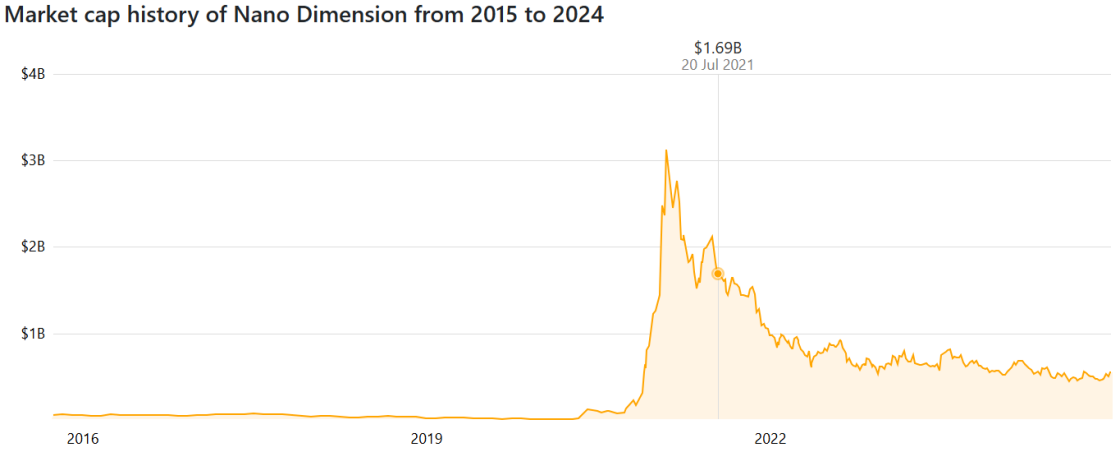

Figure 2-3: Historical market capitalisation of Nano Dimension from companiesmarketcap.com [14]

The reality is that while AM offers the benefits listed at the beginning of this chapter, it rarely provides all of them simultaneously. In fact, AM is not a single cure-all technology but rather a broad term that covers several different approaches to producing a part from 3D model data, usually layer by layer, as described by DIN EN ISO/ASTM 52900 [15]. Each of these has its strengths & challenges, can process different materials from different feedstocks, and each has found its niche applications, where, as GE has shown with the fuel nozzle, it can outperform conventional manufacturing techniques. The nozzles are still made additively, and many more parts of a turbine are now made the same way.

As the chapter title suggests, this work deals with MEX rather than PBF, aiming to help find the industrial applications where it can break into industrial serial production. To help clarify the distinction between the technologies, the next chapter will provide an overview of the different technologies classified as AM.

2.1 Overview of Additive Manufacturing Technologies

DIN EN ISO/ASTM 52900 classifies all AM technologies into seven clusters by the method in which the material is applied:

1. Binder Jetting – BJT:

Which selectively deposits a liquid bonding agent, called a binder, to join material in a powder bed. Materials include metal and ceramics by printing a green body, de-powdering, cleaning, and sintering. But also sand, which can be used after cleaning for casting moulds and cores.

2. Directed Energy Deposition – DED:
   Which uses focused thermal energy and a feedstock simultaneously to deposit material along a toolpath. The predominant material is metal, but also Automated Fiber Placement (AFP) for composite manufacture can be considered DED. The feedstock is typically a metal powder, wire, or composite tape in the case of AFP.
3. Material Extrusion – MEX:
   Which has the broad description of dispensing material through a nozzle or orifice. Typical materials include thermoplastics, composites, silicones, and resins, but concrete and, combined with a binder, metal or ceramic powders to create green bodies. Feedstocks also vary, with thermoplastics being supplied as filaments or pellets, concrete and ceramics in pastes, resins and silicones as liquids.
4. Material Jetting – MJT:
   Which deposits droplets of ink or resin that are cured to build the part. Using conductive and non-conductive inks, this technology can print electronic components.
5. Powder Bed Fusion – PBF:
   Which uses thermal energy, generally a laser, to selectively melt and fuse powder layered in a powder bed. While the process started with selective laser sintering of polymers, it has since evolved to predominantly process metals.
6. Sheet Lamination – SHL:
   Which forms parts by stacking and bonding sheets, layer by layer. Typical materials are paper, metals, polymers and composites. Bonding between the layers typically occurs by adhesives, thermal bonding or ultrasonic welding.
7. Vat Photopolymerisation – VP:
   This cures a liquid photopolymer in vat selectively using light-activated photopolymerisation, often using a laser or display to cure the resin where desired.

Each process category has its own material & feedstock options, strengths & challenges and has found its respective niche.

DED and MEX, among these processes, are the only ones that deposit material only where needed along a toolpath, as opposed to powder beds, vats or sheets, which are predetermined by the machine size.

Machines and CAM software for these technologies are often similar to CNC milling machines, which also use a toolpath in layers to remove material. As in CNC machining, they too can work in 2,5D, stacking flat layers, in 3D stacking curved layers with fixed tool orientation or in 5D, by stacking flat layers with changing tool orientation, often oriented perpendicular to the pass plane.

This similarity between subtractive CNC milling and additive DED or MEX has often led to combining the technologies in hybrid machines. DED is frequently used to repair large metallic structures, where damaged surfaces are removed by milling, the area is rebuilt using DED, and finally post-processed by milling again. This is used, for example, to extend the life of turbine fuel nozzles and turbine blades. MEX, which primarily uses polymers, can be scaled to much larger machines with a wide range of output rates from a few grams to several hundred kilograms per hour. Larger output machines have found a niche in mould manufacturing using hybrid machines. Typical moulds include autoclave tooling for composites, models for sand casting, and even thermoforming moulds. But also direct-use parts, such as robot grippers, are made using large MEX machines, where the design freedom and lightweight composite materials enable lighter grippers that can be used by smaller robots to be made faster, and the robots to operate more efficiently.

While each AM technology brings unique strengths and applications, this work focuses on MEX, one of the most versatile and widely adopted AM processes. It owes its popularity to its simplicity, cost-effectiveness, and accessibility, making it the predominant technology for desktop 3D printers and a fast-growing technology in industrial applications. Directly depositing material along a defined toolpath, MEX offers flexibility in material usage and scalability for diverse applications. However, despite its advantages, MEX still has its challenges. The following chapter delves into the principles and processes of Material Extrusion, laying the groundwork for understanding its capabilities, limitations, and potential for industrialisation.

2.2 Material Extrusion Additive Manufacturing

MEX originated from Scott Crump's invention of FDM, which initially used filament or rod form thermoplastics to create parts by depositing molten material along a toolpath. Crump's innovation remains foundational, and the basic principles of FDM are now applied across a broader range of materials and scales.

This work focuses on industrially relevant thermoplastics and their short fibre-reinforced composites, high output rates, and scalability by transitioning from filament-fed systems to pellet-fed, single-screw extruder-based machines. Despite differences in feedstock, both approaches share fundamental principles and face similar challenges.

2.2.1 Process Principle

Fused Filament Fabrication (FFF) is the generic term for the trademarked FDM. The principle can still be explained with the sketches of the original patent US5121329 from 1989 [16], seen in Figure 2-4.

FFF processes a thermoplastic filament, or short fibre-reinforced thermoplastic composites, coiled onto a filament spool (114).

The filament is driven by a mechanism called an extruder (142), typically a motor driving a gear, or coupled gears, that pinch the filament (134) and push it into the hotend (122) at the set feed rate.

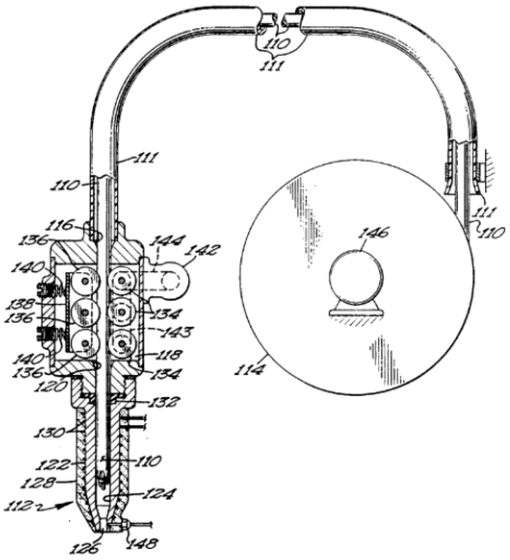

Figure 2-4: Principle of FFF from US5121329

In the hotend, the material transitions from solid filament (110) to liquid (124). It is pushed into the nozzle (126) to be deposited along the toolpath in layers to form the three-dimensional part.

The filament is compressed between the pinch zone and the nozzle by the force necessary to press the material through the reduced cross-section of the nozzle. This can lead to material oozing out of the nozzle after extrusion is stopped, for example, during a travel move between parts or sections of the toolpath.

While the standard approach today is to retract the filament to relieve the stress in it, the original invention outlined different mechanisms to shut the nozzle to prevent the material from oozing, as seen in Figure 2-5, including ball-spring combinations (96) or needle valves (166) that could also be included in nozzles with more than one hotend feeding into them (154).

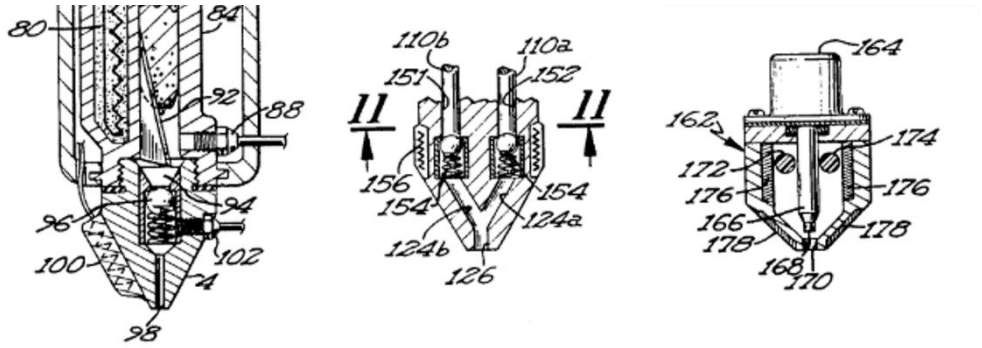

Figure 2-5: Different nozzle shut mechanisms originally proposed by US5121329 [16]

Once the material has exited the nozzle, it will quickly cool down to the temperature of the build chamber. This can either be room temperature or an elevated temperature. The

cooling down of the material is necessary for the material to become stable and support the consecutive layers. As Figure 2-6 shows on the left, when printing in a chamber at room temperature, a temperature gradient across the part height can be hundreds of degrees over only a few layers.

As Figure 2-6-right shows, this means that the deposition leads to the contact of the hot, freshly extruded material with much colder material of the layer below. The temperature of the layer below at the deposition time is called the substrate or re-coat temperature.

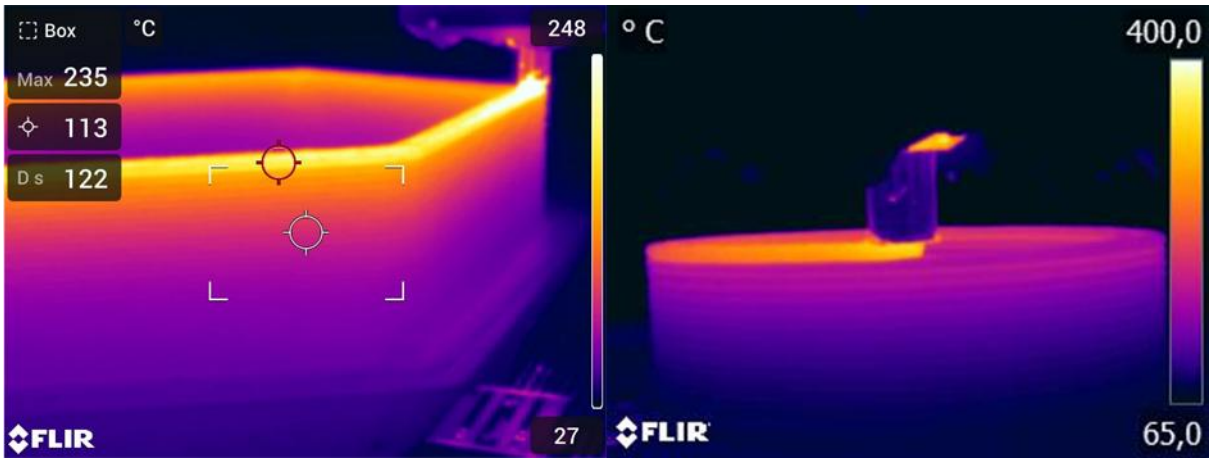

Figure 2-6: Examples of the infrared images of a MEX print, showing a hot top layer extruded on colder layers below.

These temperature gradients are the root cause of many of the challenges in MEX, which will be explained in more detail in chapter 2.3.3.2.

To generate the toolpath, a 3D model of the part is converted into a layered toolpath using Computer Aided Manufacturing (CAM) software, commonly referred to as a slicer. As the name suggests, the software slices the model into layers of a specified thickness, corresponding to the target resolution of the print. Each layer represents a typically horizontal cross-section of the part, and the slicer calculates the toolpath within each layer to determine the nozzle's movement during printing.

The printed part can achieve different functional properties by varying the toolpath pattern within the layers. For example:

- Infill patterns: Adjusting the internal structure (e.g., grid, honeycomb, or solid) influences the strength, stiffness, and weight of the part.
- Wall thickness: Modifying the number of perimeters around the part's edge affects surface finish and impact resistance.
- Layer height: Reducing layer height improves surface smoothness and dimensional accuracy while increasing it reduces print duration.

The flexibility of slicing strategies allows the designer to optimise the part’s performance, balancing material usage, mechanical properties, and production speed.

When printing, the layers start on a build platform and, from there, are stacked onto each other. Layer height is determined by the distance of the nozzle to the layer or platform below, with the nozzle, which often has a flat bottom, acting as a doctor knife that calibrates the layer height by wiping the layer flat.

Figure 2-7 shows different strategies to build these layers.

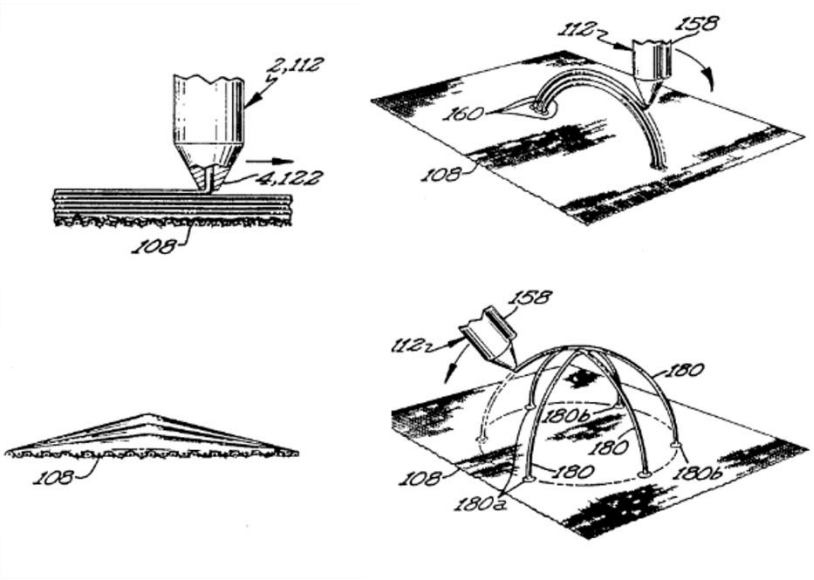

Figure 2-7: Different layering strategies in FFF from US5121329 [16]

At the top left, the typical approach is to print flat, two-dimensional layers of constant thickness on a flat build plate stacked vertically. It is referred to as 2.5D printing. But even the original patent foresaw other approaches. Figure 2-7 at the top right shows a 3D approach, where the layers are of constant thickness, but the nozzle moves vertically as well, while maintaining a constant orientation. Similarly, the bottom left shows vertical nozzle movement but with variable layer height by extruding more or less material. This can benefit the model's surface quality, with the steps of the layers not being visible on curved surfaces. Finally, the bottom right shows 5D printing, with the nozzle moving in all three directions and tilting perpendicular to the layers. This further improves the finish of the curved surfaces and reduces the need for support. 3D and 5D printing can improve part strength by aligning load paths with extrusion lines, leveraging fibre orientation, and avoiding loads across weak layer interfaces. In these cases, the slices of the Computer-Aided Design (CAD) model are not horizontal but follow a guiding surface or are generated across guiding curves.

These approaches have clear parallels to milling strategies, showing the synergies between these manufacturing technologies.

While the sketches of Figure 2-7 considered a still flat build platform and printing in mid-air, this is often done by starting flat and increasingly changing orientation, a combination of the bottom left and the two approaches on the right. Or by printing on a non-flat base body.

The process parameters set are typically:

- the temperature of the hotend, sometimes in multiple zones,
- the movement speed of the nozzle, also called print speed,
- the layer height
- and the line width, which is determined by the amount of material fed into the hotend and the movement speed of the nozzle, with material flowing to the sides under the nozzle.

The feed rate of the material into the hotend is automatically calculated from these.

2.2.2 Large Format Additive Manufacturing

LFAM operates on the same fundamental principles as FFF. However, the extrusion head is different. By replacing the filament feeding system with a single screw extruder, LFAM can increase the output from mere grams per hour to several kilograms or even hundreds of kilograms per hour, as shown in Figure 2-8. This increase is aided by the use of pellet feedstock, which is directly plasticised and extruded by the screw mechanism.

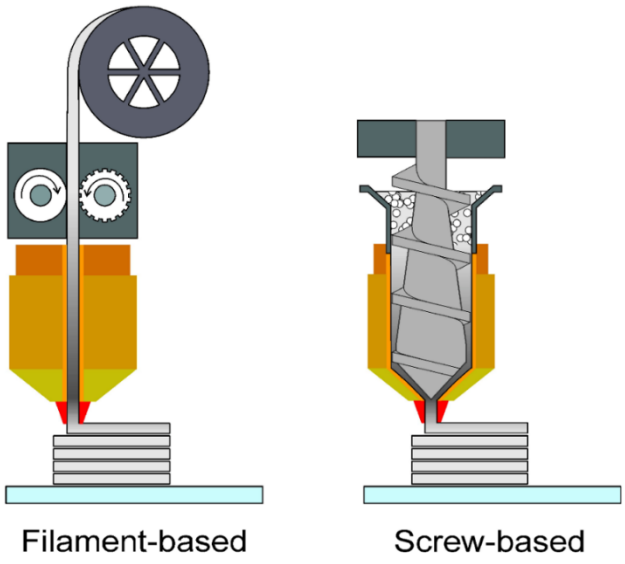

Figure 2-8: Sketch of FFF and LFAM type extrusion heads from Gonzalez-Gutierrez [17]

In filament-fed systems, the filaments are typically 1.75 or 2.85 mm in diameter and are melted and extruded over short distances using conductive heating in the hotend. In contrast, pellet-fed systems use pellets similar to those used in injection moulding or continuous extrusion. These pellets are melted over much longer distances using a combination of conductive heating from the extruder barrel and shear friction generated by the rotating screw.

Using pellets instead of filaments offers advantages to the material range. They allow the processing of materials too rigid to be coiled into filaments, such as high-performance composites and flexible polymers that would deform or compress under the pressure generated between the pinch wheels and the nozzle, clogging the feed.

Pellets also offer cost savings as producing filaments requires tight diameter tolerances, significantly increasing manufacturing costs. Pellets, by comparison, are readily available at a fraction of the cost, making them a more economical choice for large-scale production.

Like FFF systems, material oozing from the nozzle is challenging in LFAM. However, screw extruders cannot pull the material back to prevent unwanted extrusion, as is done with retraction. Additionally, screw extruders have non-linear behaviour under dynamic conditions as pressure builds or decreases. Similar to the nozzle-shutting mechanisms of Figure 2-5 in LFAM, mechanical solutions are also used, and they are easier to implement due to the larger nozzle sizes.

One of the most effective solutions is the use of a gear pump, a component that addresses both flow control and nozzle shut-off, as shown in Figure 2-9. The gear pump consists of two meshing gears housed in a casing, creating a high-pressure outlet and a low-pressure inlet.

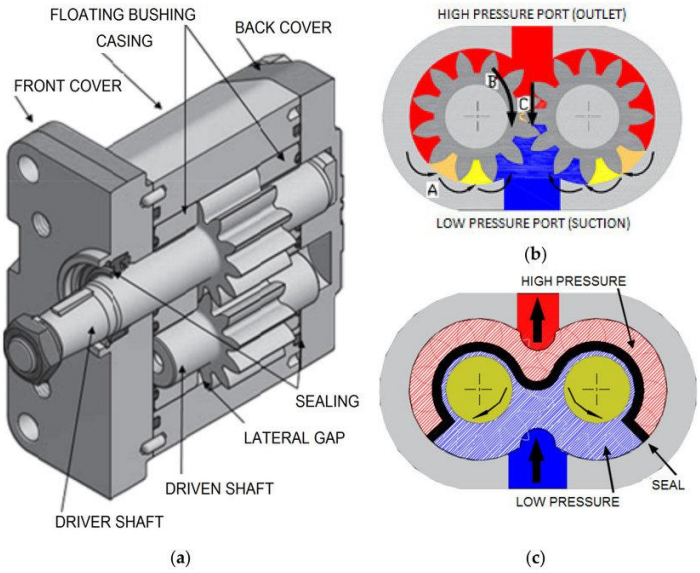

Figure 2-9: Working principle and model of a gear pump, from Torrent [18]

The movement of the polymer through the gaps between the gear teeth is tightly controlled. The nearly linear volumetric output of the gear pump offers better flow control compared to the non-linear behaviour of screw extruders under dynamic conditions. Also, halting the gear rotation effectively stops the flow to the nozzle. The use of a gear pump also allows the use of high-compression screws, which melt material more effi-

ciently. However, these screws exhibit more non-linear flow characteristics under varying extrusion speeds, making the gear pump indispensable for smoothing out material flow during the typically very dynamic operating conditions of MEX.

Despite these advantages, gear pumps cannot eliminate oozing, as residual pressure in the outlet line can still drive the material through the nozzle. Retraction is not recommended in LFAM systems with gear pumps, as reverse flow pushing against the extruder could result in sharp pressure spikes, potentially damaging the system.

Whether FFF or LFAM, the processes share the same foundational principles of layer-by-layer deposition along a predefined toolpath. Maintaining appropriate temperatures both in the extrusion head and in the part during processing is critical for material flow, layer bonding, and dimensional accuracy. While at a much larger scale, material still flows out of the nozzle and into the extrusion line, orienting fibres and fillers through the same mechanisms.

For both these processes, the following work will use a coordinate system nomenclature based on the extrusion as it exits the nozzle at the deposition point:

- X is defined as tangent to the toolpath.
- Y is defined perpendicular to the toolpath tangent to the layer plane.
- Z is defined perpendicular to the layer plane.

This differs from the machine coordinate system defined in DIN EN ISO/ASTM 52900, but to explain the process-property relationships in MEX due to extrusion dynamics and their effect on microstructure and mechanical behaviour, decoupling the coordinate system from the machine's global orientation provides a consistent reference for analysing material flow and deposition behaviour, irrespective of part orientation within the build chamber.

2.2.3 Current Challenges

MEX has come a long way since its invention in the 80s, but it still faces several challenges that hinder its adoption in industrial production. Some of the most frequently investigated challenges of AM are:

- Anisotropic material properties [7], [9], [19], [20], [21], [22], [23]
- Surface quality and accuracy [2], [8], [10], [11], [23], [24]
- Design constraints like overhangs & feature size resulting in material waste for supports and postprocessing [7], [10], [11], [24]
- Low production speed [1], [2], [11], [22]
- Quality repeatability issues [1], [2]
- Poor experience resulting in highly skilled labour requirements [2], [9]

The often-reported challenge of anisotropic material properties and quality repeatability issues are significant obstacles to the mass adoption of AM in the industry. Unpredictable material properties make a production process unsuitable for many applications as a design-to-load approach, enabling lightweight design and efficiency improvements, is impossible without significant effort for product property assurance. In surveys done by AM service providers Sculpteo and Hubs in 2021, this was represented in their customers' answers. 53% of participants answered that quality assurance is the most significant challenge in their current application [25]. In the other survey, which challenges prevented the use of AM in more applications, 38% answered that high costs for AM, quality assurance and post-processing were the main challenges, and 29% saw achievable quality as the limiting factor [26].

The materials used by both these processes will be introduced and explained in the next chapter before introducing applications that are already viable despite the challenges faced.

2.3 Thermoplastic Materials and Their Fibre Composites Used in Material Extrusion AM

When exploring the relationship between process and property, as well as the influence of extrusion dynamics on microstructure and mechanical behaviour, it is essential to recognise that the process is just one part of the equation. The selection and characteristics of materials significantly impact the performance of the resulting parts. These materials directly and indirectly influence processing conditions, ultimately affecting the overall outcome.

This chapter focuses on the thermoplastic materials and their composites commonly used in MEX. It begins with classifying the thermoplastics frequently utilised in MEX and then examining their composites and functional enhancements. Finally, a high-level overview of the effects of MEX on material microstructure will be provided, laying the groundwork for the detailed theoretical analysis in the chapter 3.

Chapter 2.4 will introduce various applications that utilise these materials and highlight the successful implementations based on currently achievable properties.

2.3.1 Thermoplastics Used in Material Extrusion

A variety of thermoplastics are used in MEX. Figure 2-10 lists examples and classes them into general-use polymers, engineering polymers and high-performance polymers. The pyramid's base consists of cheap, high-volume polymers; the further up on the pyramid a polymer is listed, the higher its material properties and price. While general-use polymers are often used as packaging, engineering and high-performance polymers are

used as functional materials in applications subjected to mechanical stress, impact, flexure, vibration, temperature extremes, hostile environments, etc. [27]. The left side of the pyramid shows amorphous polymers and the right side shows semi-crystalline polymers.

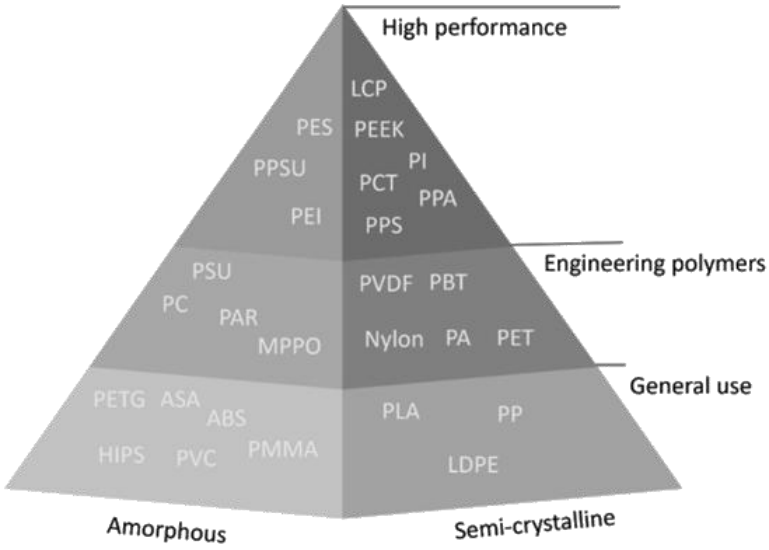

Figure 2-10: Classification pyramid for thermoplastics, from [28]

While hobby machines mostly use materials such as PLA, PETG, ASA and ABS, industrial machines often focus on higher-temperature materials. Starting at the pyramid bottom with ABS, upwards to the higher performing PC and PA. Polymers like PEI, PESU, PAEKs like PEEK and PEKK, or the Low Melting PAEKs by Victrex plc, Thornton, UK, are used for applications with the highest performance requirements. Generally, amorphous polymers are more common in MEX as they are easier to process. For example, Airtech International Inc, Huntington Beach, USA, a material supplier that produces polymer compounds for LFAM, currently has exclusively amorphous polymers in their portfolio as listed in Table 2-1 below:

Table 2-1: Portfolio of Airtech International Inc. as of December 2024

Product Name	Base Polymer	Reinforcement Fibres
T-100GF	PETG	Glass Fiber
S-150CF	ABS	Carbon Fiber
S-150GF	ABS	Glass Fiber
C-250CF	PC	Carbon Fiber
C-250GF	PC	Glass Fiber
I-350CF	PEI	Carbon Fiber

U-350CF	PESU	Carbon Fiber

The general-purpose products are offered for low-cost and temperature applications. In contrast, the engineering type, PC, is aimed at high-strength, medium-temperature applications, and the high-performance types are for high-temperature applications and are only offered with carbon fibre reinforcement.

In industrial applications, semi-crystalline polymers have often been the materials of choice in traditional manufacturing. These materials, too, are used in MEX, though they are much more challenging to process. Polyamides are used in the automotive industry, and polyaryetherketones (PAEK) are used in medical applications and in aerospace research. Chapter 2.4 will introduce some of these applications.

High-performance polymers have been adapted in their design and formulation for AM, as their high cost makes AM a desirable manufacturing method due to its high material efficiency. Victrex has developed PAEK materials with adjustable properties, named "Low Melting Polyaryletherketones" (LM-PAEK). They are made as PEEK-PEDEK copolymers [29] and, through the composition, can be adjusted to crystallise slower, show less shear-thinning viscosity, lower melting point and overall better processability [30]. This aims to improve the mechanical properties in AM [31].

A similar approach has been undertaken for Polyetherketoneketones (PEKK) by adjusting the ratio of terephthaloyl (T, straight, para substitution) and isophthaloyl (I, kinked, meta substitution) moieties to modify the crystallisation kinetics and melting point. By changing the T:I ratio between 60:40 and 80:20, the melting point shifts from 300 to 360°C and crystallisation from extremely slow, or pseudo-amorphous, to extremely fast [32]. The PEKK and LM-PAEK materials may show complex melting behaviour with multiple peaks [33]. A similar approach has also been described for the common FFF polymer PLA [34].

Slowing the crystallisation has been shown to improve the bonding between layers [35], which is why amorphous polymers have dominated the MEX process. This will be explained more in detail in chapter 3.1.2 which dives into the bonding mechanisms and crystallisation.

2.3.2 Function of Fibre Composites in Material Extrusion

Composite materials in MEX are typically short fibre, or discontinuous fibre, reinforced composites as they are easier to process. Fibre lengths are <1 mm and the materials are prepared by mixing fibres and matrix when making the pellets or filaments, which can then be extruded together. Fibres are typically glass or carbon. The effects of the fibres on the properties of the compound have been well documented but are complex. Parts of the same batch of material may show different properties depending on the flow of the material, and even within a single injection moulded part, the properties may vary

from one location to another [36]. Both glass and carbon fibres increase strength and stiffness with increasing fibre content [37]. As these fibres also have a significantly lower coefficient of thermal expansion (CTE) than polymers, the composite also shows a lower CTE [38]. This is desired in end-use applications, such as composite production moulds, and during processing, where it leads to lower warping. As shown previously in Table 2-1, all LFAM materials by Airtech contain some fibre reinforcement as, at that scale, processing unreinforced polymers becomes highly challenging due to warping.

The improvements achieved by adding short fibre reinforcement have been to aid only along the extrusion paths, often leading to lower properties than the unreinforced counterparts perpendicular to them [38]. This is due to the material flow during extrusion, which does not fill a mould as in injection moulding but instead follows the toolpath. This will be explained in detail in the chapter 3.1.

MEX can also process continuous fibres for high-performance applications, though this is more common in the FFF processes than LFAM. In LFAM, a combination has been investigated for tooling using a woven continuous fibre tape, which showed that the improvement along the extrusion direction over short fibres is marginal. Yet, the properties perpendicular in the layer could be improved by the 90° fibres. Across the layers, the added fibre leads to an increase in CTE, as mentioned above [39].

Continuous fibres remain the exception in LFAM, and while unreinforced polymers can be processed in FFF with the help of heated build chambers to minimise warping, short fibre composites are the standard in LFAM, not only because they are needed in the applications, but also already during processing.

2.3.3 Process Effects on Mechanical Properties

The layer-by-layer deposition along toolpaths creates processing effects that influence the material's mechanical properties. This subchapter will introduce the effects before chapter 3 will outline the methods used to quantify their influence on a detailed level. Chapter 4 introduces the experimental design to test for the effects and chapter 5 the results to better understand the process-property relationships.

2.3.3.1 Effect of Material Flow along Toolpath

During extrusion, material flows from a larger channel in the hotend into the narrower nozzle and is deposited on the build platform. Due to the relative motion along the toolpath, the material flows along a 90° turn into the extrusion line. This flow of material with flow velocity and direction changes affects fibre orientation and determines the fibre distribution within the part. Also, porosity is affected by the extrusion.

Fibres are known to align in flowing polymers due to shear forces. This effect is also present in moulding processes and has been described in detail. The shear forces rotate fibres inside a flowing melt until they align with the flow lines in a steady state position. In MEX, the material flow under the nozzle is the last flow stage and is critical to fibre

alignment. While the average orientation of fibres is always along the toolpath or X direction, the individual fibre orientations are affected by the flow, and the overall distribution of individual orientations describes the fibre alignment. This alignment increases the tensile strength and stiffness and reduces the CTE of the material along the flow lines. The process settings strongly affect this effect and can thus be designed for. This will be described in detail in chapter 3.1, the test methods in 4.2 and the results in 5.1.

Fibres are distributed within the extrusion line, and fibres in edge regions mostly align with the toolpath direction. When extrusion lines interact with each other, either within a layer, contacting in Y, or between layers, contacting in Z, their behaviour resembles colliding flow fronts during mould filling. This also comes with similar effects, the most important being that short fibres don't extend across the weld line, limiting their effect on strength in Y and Z and that air can be trapped between the fronts, accumulating porosity between them.

Porosity in MEX can occur in different manners. Herein, two terms are used: microporosity to describe tiny pores within the extrusion lines and macro pores between the extrusion lines.

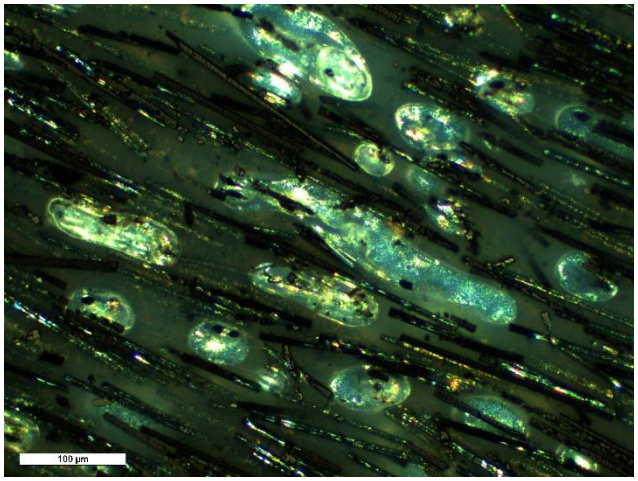

Figure 2-11: Micro pores between the carbon fibres in an extrusion line

Micropores, as the ones in Figure 2-11, can have different causes, like moisture in the feedstock, porosity trapped in the feedstock or vacuoles caused by material shrinkage, especially in fibre-reinforced materials. Previous studies have shown that the process cannot remove porosity trapped within the filament feedstock in FFF and will remain within the part [40]. Fibre reinforcements have a much lower CTE than the surrounding polymer and will not shrink during cooling, whereas the polymer between them will contract and can potentially form vacuoles. Pores tend to be round if small but become elongated with increasing size.

Macro pores occur when the toolpath stepover in a layer is larger than the width of the extrusion line or when the rounded edges barely touch. The former results in gaps between the extrusion lines of an entire layer height and that can stack across layers. The latter results in triangular or diamond-shaped holes at the edges of the extrusion lines, but they are contained to one or two layers at most if directly in contact. This can be avoided by correctly setting the relationship between stepover and extrusion quantity. Both types of pores and the correct setting can be seen in Figure 2-12 below.

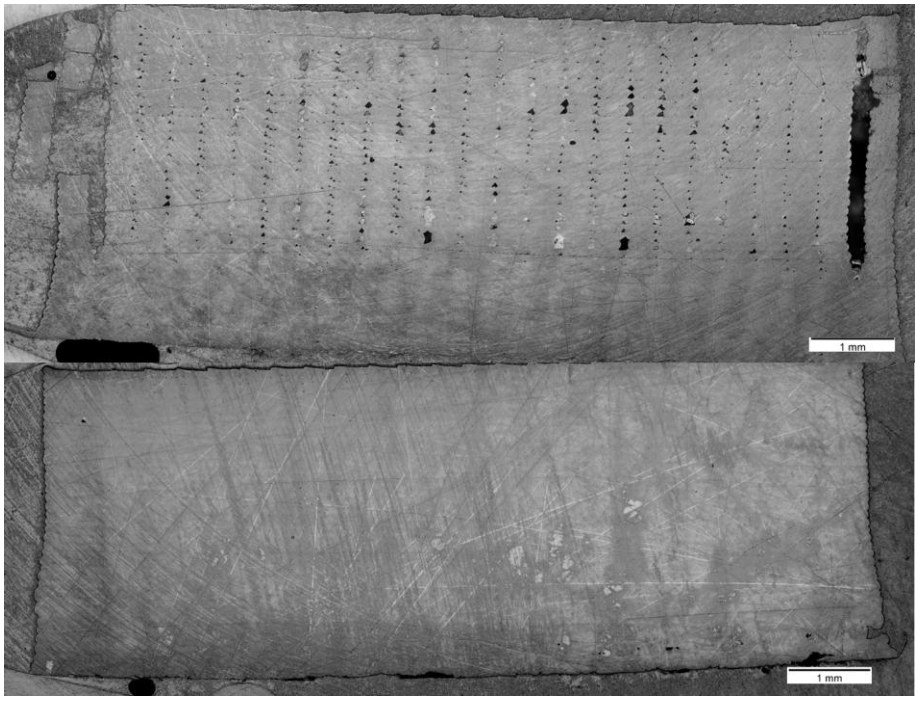

Figure 2-12: Top: Macropores due to incorrect stepover - extrusion width ratio. Bottom: correct setting without macropores

As both types of pores can be avoided by proper material handling and extrusion calibration, these effects are not investigated in detail in this work. The occurrence of vacuoles may be reduced with the extrusion parameters. However, their occurrence was so rare that they were assumed negligible.

A square core with semi-circular sides also called a disco rectangle, can approximate the extrusion line cross-section, as seen in Figure 2-13. The macropores seen in Figure 2-12 are caused by the gaps under the semi-circles. This shape of the extrusion lines in layers also results in the typical ridged surface of MEX parts. This rough surface needs to be post-processed for applications requiring smooth surfaces. When left on, the parts can also act as notches, leading to stress concentrations, further affecting the mechanical properties.

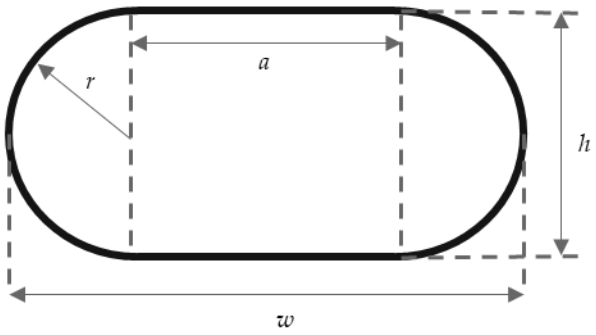

Figure 2-13: Approximation of the extrusion line cross-section shape

Line width is generally at least equal to the nozzle diameter, except when filling gaps between previously extruded lines. The layer height is typically 50% or less of the line width. As a result, the material flow when exiting the nozzle is usually stretched along the X-axis due to the low layer height. It may also be stretched along the Y-axis if the

line width exceeds the nozzle diameter. In FFF, layers are generally thin, often less than 1 mm; however, in LFAM, layers can be significantly thicker, starting at around 0.5 mm, with larger machines capable of extruding layers of 5 mm or taller.

2.3.3.2 Effect of Layer-by-Layer Deposition

A key distinction between AM and moulding or casting processes is that material is built layer-by-layer rather than in a single shot. This creates interface effects between them. As mentioned before, the flow causes fibres not to cross this interface, but the matrix polymer is also affected. As consecutive layers are deposited later, the material of the previous layers cools down and undergoes changes that can affect the following layers. These interfaces are not present in bulk material solidified from the melt in a single step.

As outlined in chapter 2.2.1 about the Process Principle, the material needs to cool down to support the subsequent layers. This leads to the thermal gradient from the hot top to the colder bottom and hot extrusion lines deposited on colder substrate layers. These inherent temperature gradients can cause warping and dimensional inaccuracy. As freshly extruded material cools and solidifies, differences in thermal contraction between layers introduce stresses. As each layer cools and contracts, it builds stresses and transfers them to the layers below that support it. These stresses are significantly pronounced in parts with large dimensions, high thermal gradients or large CTE, leading to warping or deformation during or after printing.

This effect of layer-by-layer deposition affects the final part rather than the material, which is the focus of this work and will thus not be investigated herein.

In semi-crystalline polymers, cooling not only causes warping but also initiates crystallisation. The cooling rate after the material deposition impacts crystallisation behaviour. Rapid cooling can suppress crystallisation, resulting in amorphous regions with weaker mechanical properties, while slower cooling promotes crystallisation, enhancing stiffness and thermal resistance. While crystallisation also causes additional shrinkage, it locks the chains in their molecular structure, restricting their mobility and, thereby, their ability to weld. As crystallisation is a temperature and time-dependent process, cooling the layer below and the delay before the next layer is deposited means the layer will likely have begun to crystallise before the next layer is deposited. As mentioned in the chapter 2.3.1, an approach to counter this is to slow crystallisation kinetics to make the polymer behave pseudo-amorphously, meaning that for the duration of a complete layer, the material will not crystallise. If crystals have formed, extruded material's energy is generally insufficient to remelt them, and the layer will not weld together. Meanwhile, the crystals of the layer below may even induce a structure in the layer above. Figure 2-15 shows a lamellar structure in a layer induced by the spherulites of the layer below as crystals in the melt continue to grow from the crystals at the interface rather than newly formed nuclei.

This has been reported in the literature already for compression moulded parts, as seen in Figure 2-14.

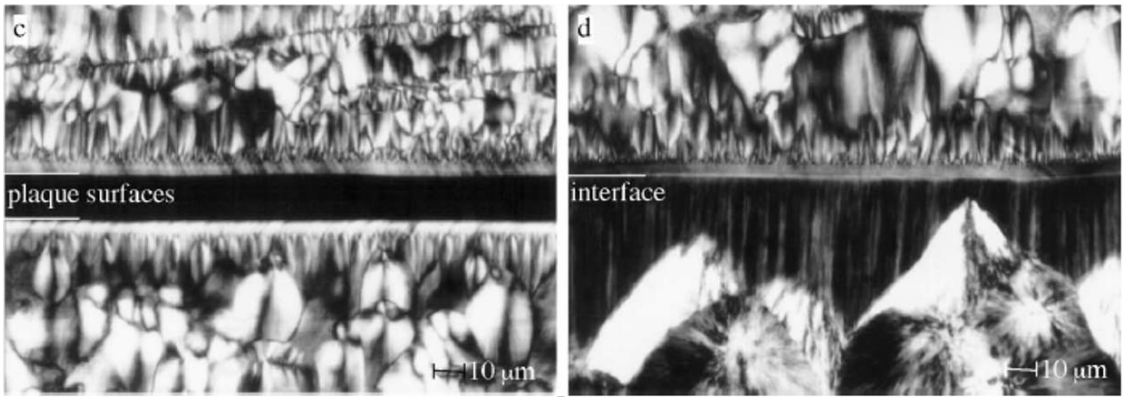

Figure 2-14: Lamellar crystal structure found in the literature [41]

But it can also be seen in LFAM-produced material, as seen in Figure 2-15 on PP specimens.

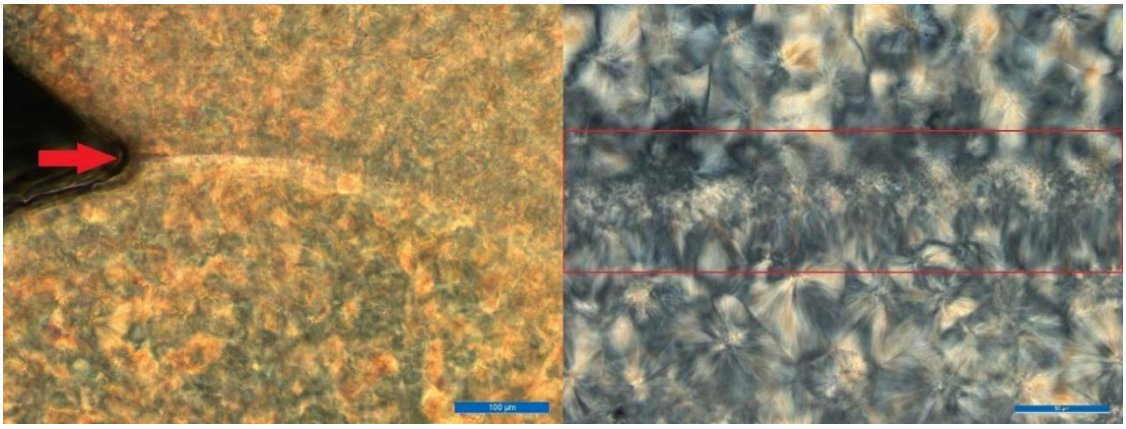

Figure 2-15: Crystal structure in a printed sample of Polypropylene, with lamellar crystals growing from the layer interface from [S20]

Crystallisation modelling and how it is considered in this work in detail will be the subject of chapter 3.2.

The interface between layers is a critical weak point in MEX-produced parts. The freshly extruded material relies on thermal fusion to bond with the previously deposited layer during deposition. The polymer chains on both sides of the interface diffuse across the interface and return to an entangled state, essentially dissolving the interface on a molecular level. This process is temperature-dependent. However, due to the cooling of the substrate layer, complete molecular diffusion rarely occurs, leaving an interface weaker than the bulk material. Additionally, crystallisation may hinder it, as mentioned above. This incomplete fusion often results in brittle failure modes at the layer interface, even after machining the ridges away, in contrast to the ductile failure observed along the extrusion toolpath.

This anisotropic behaviour and process-induced weakness at the layer interface is the core focus of this work, as it is a key barrier to adopting MEX for mechanically functional material.

2.4 Applications of Material Extrusion

MEX has established a strong presence in specialised niches by delivering value with the available materials and achievable properties. It has found applications across various industries by meeting unique geometric and functional requirements. This chapter illustrates the industries where MEX is already being used for production instead of prototyping, emphasising their specific needs and the importance of material properties in fulfilling these requirements. It also highlights a wide range of applications, from high-precision and sterile production for surgical applications to high-temperature and chemical-resistant applications in moulds for composites and components for the oil and gas industry. Additionally, MEX is utilised for volume production in automotive and wastewater shafts.

2.4.1 Aerospace Applications

In aerospace LFAM, it has found a niche in tooling applications for composite production. While AM often offers advantages in reducing lead times, material waste, and cost compared to traditional machining processes for R&D tooling, it has also been able to transition to the first serial production tools.

In aerospace tooling, MEX uses high-performance thermoplastics like PEI or PESU [39] to produce near-net shape parts post-processed by CNC machining, often on the same machine in a hybrid setup. Lower-temperature polymers like PA6 have also been investigated for lower-curing composites [42]. The tooling replaces aluminium or Polyurethane block-based tooling for low to medium-volume production. Similar approaches can be found in other industries working with composites, like marine or high-performance automobiles.

The key benefits of MEX-produced tooling are:

- shorter lead times and reduced cost,
- lower waste due to near net shape manufacturing where only the surfaces need to be machined instead of blocks,
- longer life span compared to PU blocks and composite tools,
- In R&D, there is the possibility of introducing complex custom geometries for functionalisation, like heating, cooling, resin injection, or handling.

GKN Aerospace has succeeded in developing LFAM-manufactured tooling that is now used as a serial production tool. The pressure intensifiers used in landing flap production used for autoclave curing and positioning of the stringers had previously been manufactured by hand layup of tooling prepreg, as a CTE match with the landing flaps is critical

with part sizes of up to 12 m. The MEX version performs as required while providing the benefits listed above, cost savings, and a simplified supply chain for the tooling material.

R&D efforts are being reported in the direct printing of interior cabin components using materials like Ultem, a PEI by Sabic, and research into printing on composite surfaces, focussing on the functionalisation of these structures.

Materials in use are primarily amorphous high-temperature thermoplastics like PEI and PESU, while research is also looking into semi-crystalline materials, mostly of the PAEK family with low melting PAEK (LM-PAEK) by Victrex and PEKK by Arkema both offering tuneable crystallisation kinetics and showing promising results.

The work presented here was financed through two projects looking into aerospace tooling. First, an LM-PAEK-based resin transfer mould for a flaperon for Saab Aerostructures in a Horizon Europe Clean Sky 2 project, called COMBO3D, under grant agreement number 831851. The aim was to improve the mould's cycle time through integrated thermal control and reduce its development and lead time while maintaining a similar lifespan and cost to conventional tooling [43]. Figure 2-16 shows the demonstrator tool of the project. At the top left is the CAD visualisation of the flaperon, and on the top right, where these structures are used, by size corresponding more to a flap. The bottom pictures show the near net shape printed lower shell of the mould on the left and the finished and assembled RTM tool of over 3m on the right.

Figure 2-16: Demonstrator of the COMBO3D project, top right image from [44]

The second project was the Polyetherimide (PEI) and Polyethersulfone (PESU) based pressure intensifiers for GKN Aerospace Deutschland GmbH, Munich, Germany, under the Bavarian Joint Research Program (Bayerisches Verbundforschungsprogramm (BayVFP) Förderlinie Materialien und Werkstoffe) under project 3DP-MAT. Figure 2-17 shows the project's target application, making tooling for landing flaps. At the top is the CAD visualisation of the landing flap and the intensifier model. The bottom left

shows a set of pressure intensifiers, and the bottom right shows a pressure intensifier on a landing flap after autoclave curing and de-moulding.

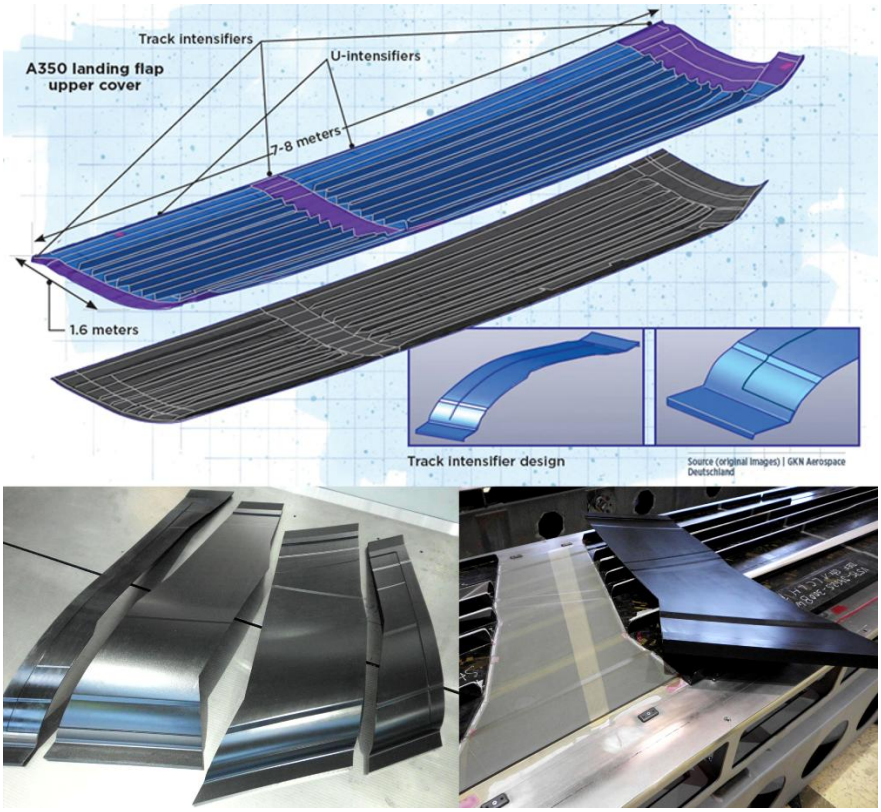

Figure 2-17: Demonstrators of the 3DP-MAT project, published in [44]

While the complete analysis of the economic benefits remains confidential, GKN has released a lead time reduction of 80% and a cost savings of 50% for the early versions of the pressure intensifiers compared to their previous version [45].

2.4.2 Industrial & Automotive Applications

In industrial production and the automotive industry, MEX has niches in pre-production prototypes that reduce the risk of expensive tooling and jigs and fixtures during production [46].

Another application that is, however, dominated by other AM technologies like PBF is the digital warehousing of spare parts after the end of production, as well as the restoration of older production runs.

The first application in the direct production of interior components has been published by BMW and Weber Additive for a centre console carrier, with a relatively low production volume of 8.000 units per year, a 40% short carbon fibre reinforced polyamide 11 [47]. Figure 2-18 shows the part on the left with the previously assembled part assembled from seven pieces, and on the right, a close-up still showing the layer lines on internal surfaces.

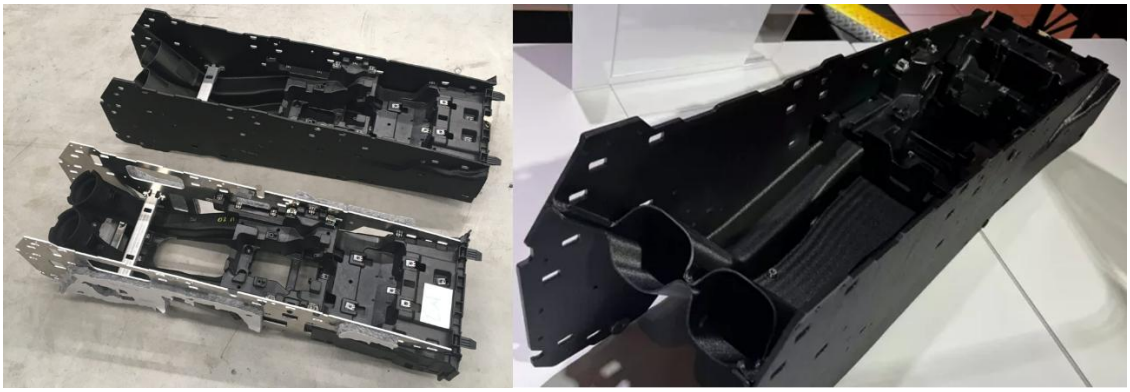

Figure 2-18: MEX manufactured centre console by BMW as published in [48]

Examples of production aids frequently manufactured also include grippers for robots. A case study by Siemens shows that polymer grippers, in their specific case, weigh up to 64% less than their conventional aluminium counterpart. This, in turn, improved the handling and manoeuvrability of robots, enabling the use of smaller robots and extending their lifespan, reducing energy consumption by up to 54% and the associated CO2 emissions by 82% [49].

Other industrial applications include PAEK materials in the Oil & Gas industry as corrosion-free components such as submersible pumps and impellers, seals, tubing, and valves [28][50]. PAEKs are chosen for their high thermos-mechanical properties, corrosion resistance, chemical stability and fatigue resistance. However, amorphous polymers like PSU and PEI have also been investigated [51].

An industrial application often overlooked and does not require high temperatures is wastewater shafts. Rehau Industries SE, Rehau, Germany, has successfully commercialised MEX-printed and machined shafts that can be designed and manufactured to fit the local piping grid out of semi-crystalline PP. This, too, is a serial production component that offers significant volumes through mass customisation.

Figure 2-19: Wastewater shaft by Rehau Industries, from [52]

Materials investigated in automotive research also include polycarbonate for combination with pre-made sheets or composites [53] and using the serial production polymers

from injection moulding, like Polyamide 6 [54], typical representatives of engineering thermoplastics.

2.4.3 Medical Applications

In medical applications, especially implants, PAEKs stand out and are considered the most promising materials [55]. MEX offers the possibility to design and manufacture implants directly at the point of care under the involvement of the treating surgeon [56], with first solutions offering complete workflows from design to sterilisation of ready-to-implant parts at the point of care [56]. This offers significant cost savings, especially lead time savings critical to patient care, while leveraging AM's capability for complex geometries and economies of scope to provide patient-specific parts. The benefits of PAEKs include their biocompatibility [57] and their ability to withstand steam sterilisation without being negatively affected [58]. Printing of small implants in a tightly controlled heated build chamber leads to high dimensional accuracy and almost isotropic behaviour [57]

Other applications include surgical guides, dental, short-term implants that can be sterilised up to 500 times, impression trays [58][59] and tissue engineering [46].

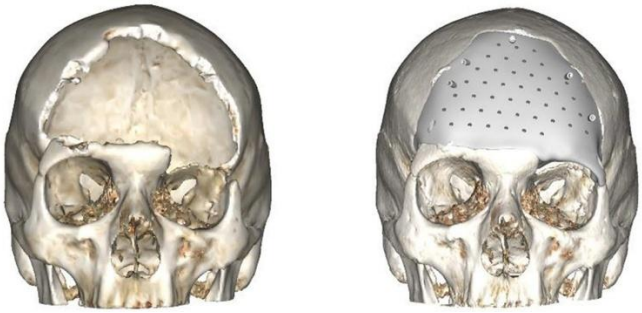

Figure 2-20: A three-dimensional cranial implant from [58]

2.4.4 Sustainability Considerations of Applications

MEX offers opportunities to align production efficiency with sustainability goals, addressing energy consumption, material recyclability, and the role of digital tools in advancing sustainable practices.

Energy consumption in MEX remains a significant barrier to sustainability, particularly for large-scale applications. The processes often require substantial energy input to maintain heated build chambers and operate extruders, especially when processing high-performance polymers [60]. Despite these challenges, a comparison of MEX with injection moulding by Kazmer et al. [61] showed that CO2 emissions per part follow a trend similar to cost per part, which indicates that the economies of scope inherent in AM also apply to the CO2 produced. This correlation suggests that the relative environmental impact per unit decreases in injection moulding as batch sizes increase or products are tailored for specific applications. However, these emissions are constant for MEX at a

low level, offering lower cost and lower emissions for low-volume production, aligning sustainability objectives with economic incentives.

AM's design freedom enables the creation of mass-customised products that optimise resource efficiency during use. Lightweight, complex geometries reduce material usage and enhance product performance, such as fuel efficiency in aerospace or automotive components. By integrating these considerations into production, companies can achieve sustainable practices that simultaneously reduce costs and carbon footprints, reinforcing the alignment between sustainability and profitability.

Recycling thermoplastics and composites used in MEX is essential to sustainable manufacturing. The ability to shred failed prints, prototypes, and support structures into smaller particles for reuse offers a pathway to reducing waste. However, the process of recycling within MEX is not without its challenges. Contamination from previous material residues or part use can degrade the quality of recycled material [60]. Maintaining consistent mechanical properties in recycled parts is particularly challenging for fibre-reinforced composites due to fibre damage during shredding and reprocessing.

Despite its limitations, AM offers an accessible opportunity for companies to initiate internal recycling. For example, MEX can use recycled materials from its processes, such as support structures or failed builds, to create non-critical parts or prototypes. This in-house recycling helps reduce waste disposal costs and decreases the demand for virgin materials, fostering a closed-loop system that supports the principles of a circular economy. Additionally, the growing adoption of pellet-based systems, which are more effective at processing recycled materials, enhances the feasibility of in-house recycling by eliminating the need for an extra step in extruding filament feedstock[62].

MEX workflows are inherently digital, a sound basis for informed, sustainable manufacturing. First tools that prove real-time insights into the carbon footprint, energy consumption, and material efficiency of 3D printing projects, like the "EcoPrintAnalyzer", are available for open source and free CAM software, like Ultimaker Cura, a widely used slicer [63]. This allows users to make data-driven decisions, optimising production costs and environmental impacts. Again, aligning them with economic motivators by making energy costs transparent.

The availability of tools on open-source platforms ensures that sustainability considerations are not limited to large corporations with extensive resources. Instead, these tools become accessible to smaller enterprises and individual users, accelerating the adoption of environmentally friendlier practices.

By addressing energy consumption and recyclability challenges and leveraging AM's design flexibility and economies of scope, MEX has significant potential to align cost efficiency with sustainability goals. This can be achieved through energy-efficient processes, material recycling, and the integration of accessible digital tools. Easy-to-implement digital tools enable users at all levels to enhance their responsible manufacturing practices while simultaneously optimising production performance.

3 Theoretical Considerations

This chapter introduces the theoretical framework used to study the process-property relationships in MEX. The first subchapter will focus on the extrusion dynamics, the flow of material inside the extruder until the deposition and its effect on the material. The second subchapter will then introduce the crystallisation of the material as it cools after deposition. The third subchapter introduces the fusion bonding process between the deposited material and the layer below.

3.1 Extrusion Mechanics and Fibre Alignment

MEX deposits thermoplastic or composite materials along a toolpath. The material only flows until the point of deposition, after which it cools and solidifies. While molecular diffusion effects on the polymer still occur, the fibre microstructure is set at this point. The material's deposition temperature also strongly affects the thermal history it will undergo during cooling. This chapter explores extrusion mechanics and their effects on material alignment and fibre orientation.

3.1.1 Material Flow and Fibre Orientation in Material Extrusion

In both FFF and LFAM with single screw extruders, the material is molten and pressed through a hot nozzle. While similar, the melting and feeding process has a few key differences.

In FFF, the filament is pressed by feeding wheels into a hot channel and against the converging section of the nozzle. Heat is introduced in the material only through conduction from the hotend walls. High extrusion speeds, pressing the material through the nozzle faster, will lead to different temperature profiles and even different but lower extrusion temperatures, with the material melting later and possibly being extruded at a lower temperature, requiring higher extruder force [64]. Typical shear rates in the material are $<1000\ s^{-1}$ in the extrusion nozzle and $<410\ s^{-1}$ at the deposition [65]. Small nozzles and low layer height lead to these high shear rates. The volume of the fed filament sets volumetric output and is theoretically linear. However, filament slippage and compression can lead to time delays, which lead to known issues like under extrusion at line starts or stringing after line ends [66].

In single screw extruders, the volumetric output is dependent on screw speed and melt temperature [67], [68], and while output shows a generally linear relationship to the

screw RPM, it can vary between different materials on the same screw [69]. RPM and screw geometry have a substantial impact on the melt temperature, with low RPMs mainly relying on conduction from the barrel and higher RPM on shear from the screw [64]. Changes in screw RPM lead to fast changes in extruder pressure but relatively slow changes in melt temperature over a few seconds, affecting the output under dynamic conditions [70]. The typical shear rate in screw extrusion is between 20 and 500 s^{-1} [71] inside the extruder, so significantly lower than in filament extruders, mainly because of the generally larger dimensions. Gear pumps are added to the extruders to reduce surges and fluctuations in the output rate and melt temperature [72]. Another benefit is that they can build the necessary extrusion pressure, reducing the backpressure on the extruder and thereby improving the extruder output rate [73]. The output does fluctuate slightly with the number of teeth due to the function principle of the gear pump. Shear thinning of the material can result in a faster reduction of volumetric efficiency [74]. The shear rate in the gear pump can be calculated according to [74], and for a typical gear pump size in LFAM of 5 cm^3/RPM, a maximum output of about 12.5kg, a tip radius of 10mm and 0.1mm clearance, the shear rate is <420 s^{-1}, similar as inside the extruder.

While shear thinning is sometimes assumed to help with wetting for intimate contact [71], investigations on establishing intimate contact during the consolidation of thermoplastic tapes for automated fibre placement showed that even at low pressure, the contact is established very quickly [75]. Due to the effects on output, it is therefore of then avoided, as mentioned in chapter 2.3.1.

Both processes can process pure or fibre-reinforced polymers. Reinforced materials are the norm, especially in LFAM, where warping becomes a significant issue with increasing part size. With these materials, the final fibre alignment is of great importance for the resulting properties of the produced part. The fibres are arranged along the toolpath along the X direction in the XY plane, and only a tiny portion of the fibres are aligned perpendicular to the layer plane [76]. With the material flowing along Z while in the extruder, the fibre orientation changes as it exits the nozzle, and the fibres align in the plane [77]. However, the flow of filled polymers is complex, with interactions between the fibres and the flow affecting each other, and the materials contain a large number of fibres that interact with the flow this way. The highest shear is experienced by the melt in the narrowest section of the nozzle and as the flow turns under the nozzle [78][79].

The fibre orientation flowing into the nozzle or an inlet strongly affects the final orientation as it exits [80]. Additionally, swirling flows lead to different orientations of fibres inside the nozzle than non-swirling flow [81], so the extruder screw can affect the fibre alignment going into the nozzle and, thereby, the final alignment in the part.

The next chapter will examine how the deposition's material flow affects the fibre alignment, considered the critical flow stage for the final fibre orientation.

3.1.2 Fiber Alignment in Fluid Flow

Fibres in a fluid move at their centroid with the fluid velocity, and their rotation can be described with Jeffery's equation [82] for different axisymmetric particles, including fibres. Moving along an orbit, fibres reorient based on velocity gradients in the fluid [36]. This can be summarised in two simple rules:

1. Shearing flows align fibres in the flow direction.
2. Stretching flows align fibres in the stretching direction.

Stretching flows occur when the streamlines are diverging or converging. This effect is visualised in Figure 3-1. Two edges of each of the grey fluid elements lie on the streamlines. As the flow diverges in the left example, the element is stretched across the flow direction. As the flow converges in the left example, the element is stretched in the flow direction to maintain a constant volume. The example is taken from [36], where interested readers may find more information and detailed descriptions of the mathematical models. While the book focuses on injection moulding, the theory is transferable.

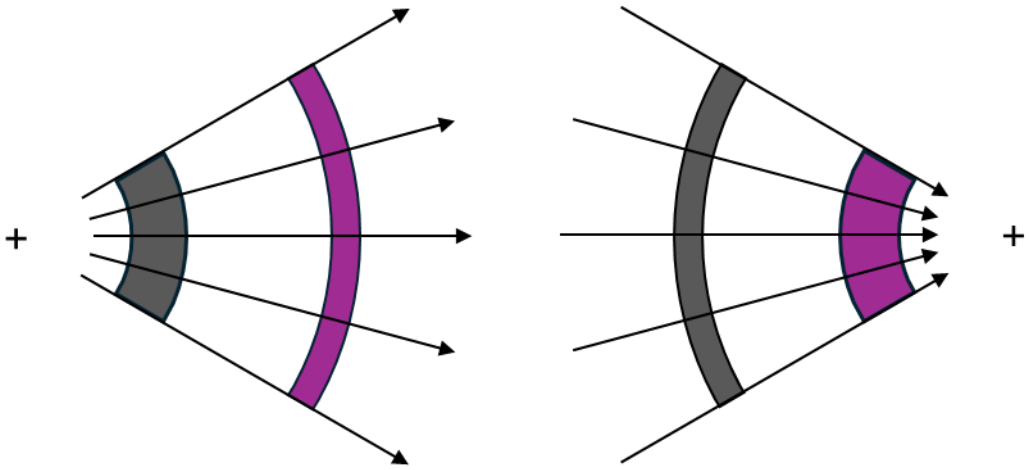

Figure 3-1: Material deformation in diverging and converging planar flows. Black lines are streamlines. A fluid element with a grey initial shape deforms into a magenta shape as it deforms [36].

Jeffery's equation has been used to describe the primary shear rate component between the toolpath and nozzle axis, XZ, during polymer stretching for the flow under the nozzle in LFAM [83]. With some empirical modifications, the equation can be written as follows:

$$\dot{\gamma}_{xz} = \frac{v_d - v_e}{h} = \frac{v_d}{h} \times (1 - \frac{v_e}{v_d}) \tag{3-1}$$

With the shear rate in XZ $\dot{\gamma}_{xz}$, the toolpath velocity of the deposition v_d, the average velocity of the extrudate v_e and the layer height h. As mentioned in 2.2.1, the feed rate of the extruder is calculated automatically from the toolpath velocity and the area of the extrusion line cross-section as described in Figure 2-13. From this, the nozzle's average

extrudate velocity v_e can be calculated similarly using the nozzle diameter. The area of the extrusion line cross-section from Figure 2-13 is:

$$A_d = \pi \times r^2 + h \times (w - h) = \pi \times ({}^{h}/_{2})^2 + h \times (w - h) \tag{3-2}$$

With the cross-section area of the deposited extrusion line A_d, extrusion line width w and side radius $r = {}^{h}/_{2}$.

The volume flow out of the nozzle and into the extrusion line must be equal, therefore:

$$A_e \times v_e = A_d \times v_d \tag{3-3}$$

$$v_e = v_d \times {}^{A_d}/_{A_e} \tag{3-4}$$

With the area of the extrusion nozzle A_e, and nozzle diameter D:

$$A_e = \pi \times ({}^{D}/_{2})^2 \tag{3-5}$$

Then (3-1) can be rewritten using just the settable extrusion parameters:

$$\dot{\gamma}_{xz} = \frac{v_d}{h} \times \left(1 - {}^{A_d}/_{A_e}\right) = v_d \times (\frac{1}{h} - \frac{h}{D^2} - \frac{4 \times (w-h)}{\pi \times D^2}) \tag{3-6}$$

Evaluating this for an extrusion width of 125% of the nozzle diameter and 50% of the layer height for typical print speeds of 10 to 100 mm/s and nozzle diameters from 0.4 to 4 mm renders the plot of Figure 3-2. This shows that, as described in the literature, the shear flow in FFF is much higher than in LFAM, which should lead to higher fibre alignment in FFF.

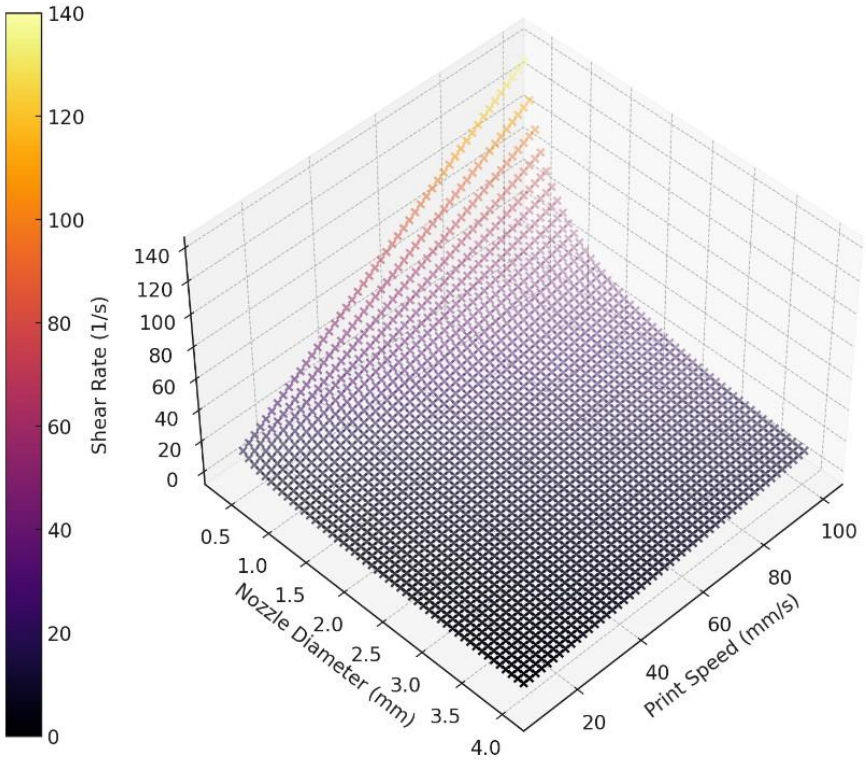

Figure 3-2: 3D Scatterplot of Shear Rate under Nozzle according to Jeffery's Equation for different Nozzle Diameters and Print Speeds

Evaluating it for a set print speed of 50 mm/s at an FFF typical nozzle diameter of 0.4 mm yields the plot of Figure 3-3. This shows that even if the nozzle diameter is unchanged, the shear rate can vary from over 400 s^{-1} to negative values. This indicates that the flow can change from converging to diverging flows, which should change the orientation direction according to Jeffery's equation.

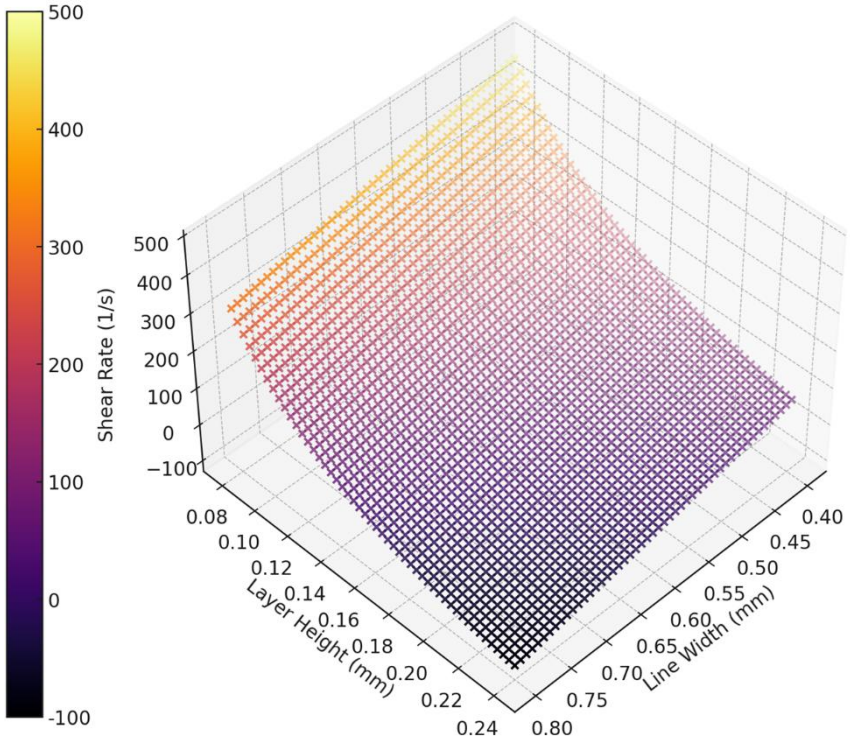

Figure 3-3: 3D Scatterplot of Shear Rate under Nozzle according to Jeffery's Equation for different Layer Heights and Line Widths

From these plots, it becomes clear that, overall, a higher degree of alignment is expected from FFF-produced samples, as the shear rate in the most critical flow stage is significantly higher than in LFAM. Additionally, the fibre alignment inside the filament feedstock is likely higher than after the extruder and melt pump of LFAM. However, the plot of Figure 3-3 suggests that when printing broad lines on tall layers, the flow conditions may shift to introduce a crossflow orientation, which should significantly impact the mechanical properties of the produced material.

This will be part of the experimental design to validate whether the flow conditions under the nozzle can affect fibre alignment as predicted by Jeffery's equation and if the process can shift the orientation away from X by achieving a diverging flow.

3.2 Crystallisation

Polymers with a regular chemical composition and geometric structure can form crystalline regions. These are formed from molecular chains arranged in parallel orientations or folding back and forth to form ordered three-dimensional structures. However, due to the inherent inability of polymer chains to completely disentangle during the crystallisation process, polymers achieve only partial crystallinity, with absolute crystallinity values remaining significantly below 100%. The non-crystalline portions remain amorphous, leading to the naming of such materials as "semi-crystalline" polymers due to their combined amorphous and crystalline nature [84], [85].

3.2.1 Nucleation & Growth

The crystallisation process consists of two main stages: nucleation and crystal growth. Nucleation can be further divided into primary and secondary nucleation, each with distinct mechanisms and effects on the crystalline structure.

Primary nucleation occurs independently of pre-existing crystals. It can be classified as homogeneous or heterogeneous. During homogeneous nucleation, nuclei form directly from the melt due to random thermal fluctuations. In contrast, heterogeneous nucleation is facilitated by foreign particles or surfaces present within the polymer melt.

Homogeneous nucleation is driven thermodynamically by the system's tendency to reduce free enthalpy by transitioning from a disordered, high-entropy state, the melt, to an ordered, low-entropy crystalline phase. The homogeneous nucleation rate highly depends on the degree of undercooling, which is the temperature difference below the melting point. Increased undercooling increases the driving force for nucleation, forming more nuclei and a higher number of crystals. However, molecular mobility decreases significantly at very low temperatures close to the glass transition, leading to incomplete crystal formation [86], [87].

Heterogeneous nucleation occurs when nucleation agents, such as fibres, pigments, or additives, act as pre-existing sites for crystal formation. This process reduces the activation energy needed for nucleation, allowing crystallisation to begin at higher temperatures than in homogeneous nucleation. As a result, it enables the growth of more ordered crystals. The crystallisation extent depends on the cooling rate and the number of nucleation sites. Lower cooling rates produce bigger and more ordered crystals, as the longer growth periods at elevated temperatures enable better crystal development [88], [89].

Secondary nucleation occurs after a significant portion of the crystalline structure has formed, usually when the degree of crystallinity exceeds approximately 50% to 75%. At this stage, crystals come into contact with one another, which limits further growth to the spaces between them. This leads to slower growth rates and the formation of the crystalline structure within the constraints of the available space. While secondary nucleation can continue for extended periods, it is less relevant in MEX, where crystallisation is limited to short timescales due to rapid cooling during the printing process.[86], [90], [91], [92].

After nucleation, crystals grow, and polymer chains reorganise into ordered regions. Initially, these regions form lamellae, which later aggregate into larger spherulitic structures. Spherulites, characterised by their spherical shape, can be easily observed under optical microscopy and are a common morphological feature of semi-crystalline polymers. Figure 3-4 shows polarised optical microscopy images of crystals in PAEK and PEEK at different cooling rates. The growth of spherulites typically occurs at a linear rate until they collide, at which point further growth is limited. The resulting crystalline

morphology depends on various growth conditions, including cooling rates and the presence of nucleation agents. [88], [89]. Figure 3-4, from [93], shows from left to right a 1°C/min and 30°C/min cooled crystal structure for PAEK at the top and PEEK at the bottom. The left images show large crystals that have begun to come into contact with one another, whereas the right shows spherulites still growing unrestricted in the surrounding amorphous material. Comparing the top and bottom images reveals that PAEK crystallises slower than PEEK, forming fewer and smaller crystals.

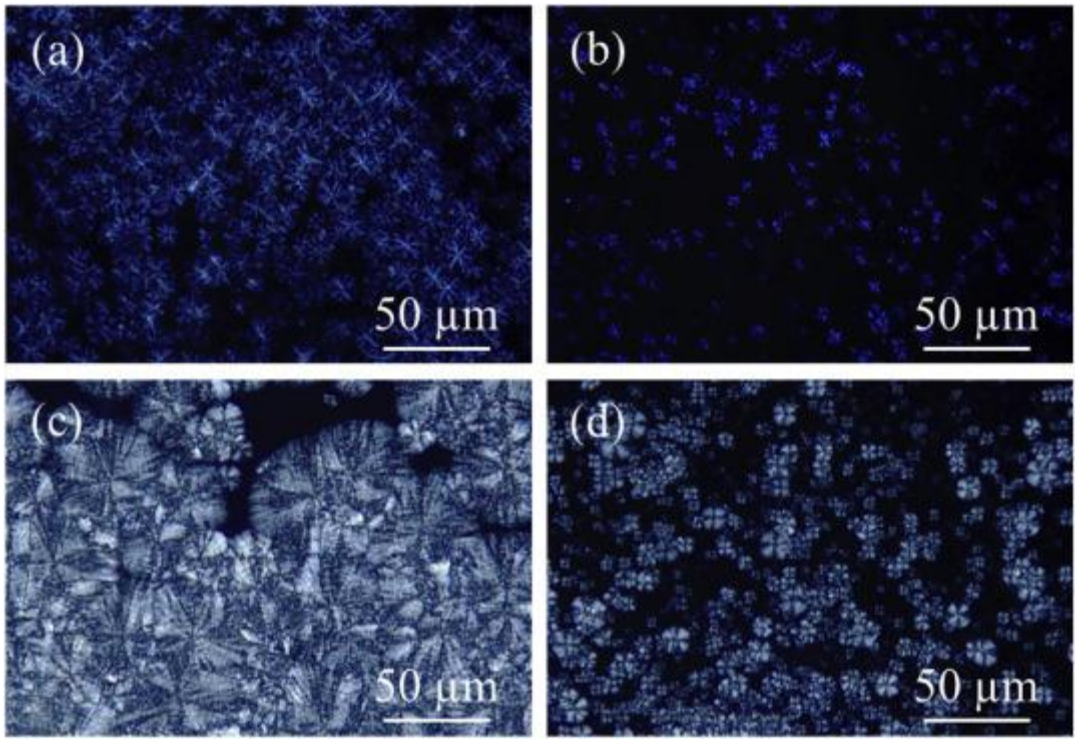

Figure 3-4: Non-isothermal polarised crystal morphology of PAEK and PEEK. (a) PAEK at 240 °C by 1 °C/min, (b) PAEK at 200 °C by 30 °C/min, (c) PEEK at 270 °C by 1 °C/min, (d) PEEK at 230 °C by 30 °C/min from [93]

Figure 3-5 shows the resulting structure of crystals limiting each other's growth in PP. While the structure appears fully crystalline, the amorphous regions still exist between the lamellas of the spherulites.

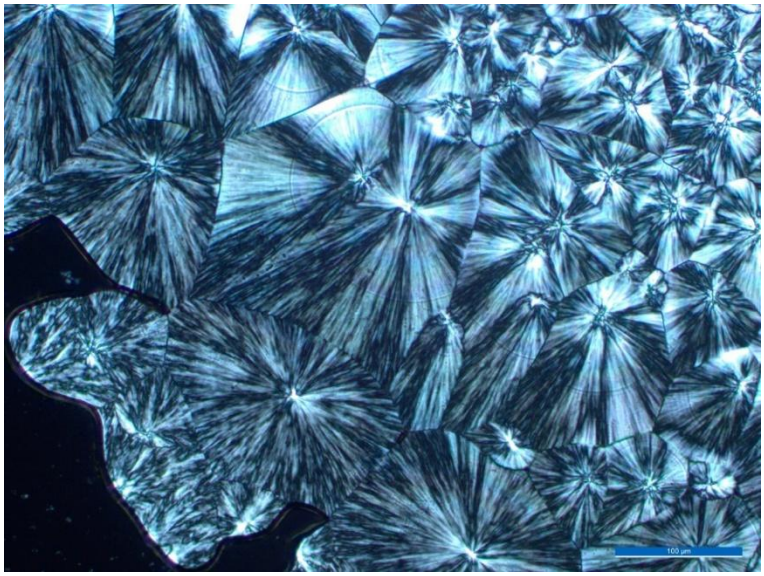

Figure 3-5: Spherulitic crystals in PP with high impingement on each other from [S20]

Several factors beyond nucleation agents affect crystallisation during MEX. These include the polymer's molecular structure, pressure, and thermal and mechanical histories. For example, increased pressure can raise the melting temperature, facilitating nucleation. While cooling and crystallisation occur in the printed part at ambient pressure, nuclei formed before the nozzle at pressures of up to 120 bars for small nozzles in LFAM may not be dissolved anymore. The duration of exposure to melt temperatures before deposition can influence the formation of nuclei, while shear forces from extrusion and deposition may orient molecular chains, affecting both primary and secondary crystallisation [92], [94].

In MEX, high cooling rates, short carbon fibres and shear-induced molecular alignment under the nozzle could all be relevant. Short carbon fibres have been reported to nucleate the crystallisation of PEEK, with shorter carbon fibres leading to faster crystallinity [95]. These conditions can lead to a high nucleation rate but may limit the extent of crystal growth, resulting in a fine crystalline structure. Additionally, interfaces between the polymer can act as nucleation surfaces, partially because they cool faster. Crystals growing from a surface will impinge quickly and grow two-dimensionally from the surface [96]. Crystals growing in layers that have been joined while amorphous have been reported to only grow across the interface if diffusion to entropy happens first [97].

3.2.2 Theoretical Models of Crystallisation

The development of crystals during polymer crystallisation has been extensively studied, resulting in multiple theoretical models to describe their kinetics and morphology. Among these, the Avrami equation, the Ozawa model, and the Nakamura model are widely used in the literature. These models describe the crystallisation process under various conditions, aiding in understanding how factors like nucleation mechanisms,

cooling rates, and thermal history influence the degree of crystallinity and crystal morphology.

Many of the models build on the Avrami equation. It has been adapted for polymers to describe isothermal crystallisation and is expressed as:

$$1 - X_r = \exp\left(-k(T) \times t^n\right) \tag{3-7}$$

where X_r is the relative degree of crystallinity, k(T) is the crystallisation rate constant at the specific temperature, t is time and n is the Avrami exponent [90].

The Avrami exponent provides information on the nucleation type and crystal growth dimensionality. Values between 1 and 2 typically correspond to needle-like crystals, between 2 and 3 lamellar crystals, and between 3 and 4 spherulites. The dimensionality of crystal growth (n_d) and the nucleation type (n_n) are combined to determine n:

$$n = n_d + n_n \tag{3-8}$$

Here, n_n ranges from 0 for instantaneous heterogeneous nucleation to 1 for sporadic homogeneous nucleation, allowing for intermediate values in mixed nucleation scenarios [88], [92].

The Ozawa model [98] extends the Avrami equation to describe non-isothermal crystallisation. It is expressed as:

$$1 - X_r = \exp\left(-K_0(T) \times \left(\frac{\Delta T}{\left(\frac{dT}{dt}\right)}\right)^m\right) \tag{3-9}$$

where $K_0(T)$ is the crystallisation rate constant, $\frac{dT}{dt}$ is the cooling rate, the amount of undercooling $\Delta T = T_m - T$, and m is the Ozawa exponent. The exponent is analogous to the Avrami exponent, providing insight into the dimensionality and nucleation mechanism. When applied to isothermal conditions, the Ozawa model simplifies to the Avrami equation [99].

Both models rely on experimental data, often derived from differential scanning calorimetry (DSC), to fit curves and calculate parameters. By plotting results on double logarithmic scales, the exponents and rate constants can be extracted from the slope and intercept of linearised curves. The transition from primary to secondary crystallisation is therein a deviation from the linear relationship. Limited by spatial constraints, secondary crystallisation results in a reduced Avrami exponent and a flatter curve [92].

While these models describe crystallisation kinetics effectively under certain conditions, they are limited in their ability to capture the complete complexity of real-world processes [90], [99], [100].

Nakamura et al. [101] introduced a model based on isokinetic assumptions for non-isothermal crystallisation. Their approach incorporated cooling rates and provided a more comprehensive description of crystallisation behaviour under dynamic conditions. By combining aspects of the Avrami and Ozawa models, the Nakamura model reduces to the Avrami equation under isothermal conditions but extends its applicability to a broader range of scenarios.

Building on existing theories, Choe and Lee [87] proposed a more detailed model to describe the crystallisation kinetics of PEEK. Their approach combined two Tobin equations [100], [102] to represent the parallel processes of homogeneous and heterogeneous nucleation. The model expressed the overall rate of crystallisation $\frac{d\alpha}{dt}$ as the sum of these two contributions:

$$\frac{d\alpha}{dt} = \frac{d\alpha_{het}}{dt} + \frac{d\alpha_{hom}}{dt} \tag{3-10}$$

The rate of crystallisation due to heterogeneous nucleation $\frac{d\alpha_{het}}{dt}$ was defined as:

$$\frac{d\alpha_{het}}{dt} = k_1 \times \exp\left(-\frac{3 \times E_d}{R \times T}\right) \times \exp\left(-\frac{3 \times \psi_1 \times T}{T \times (T - T_\infty)}\right) \times t[1 - \alpha(t)] \tag{3-11}$$

and for homogeneous nucleation $\frac{d\alpha_{hom}}{dt}$):

$$\frac{d\alpha_{hom}}{dt} = k_2 \times \exp\left(-\frac{4 \times E_a}{R \times T}\right) \times \exp\left(-\frac{3 \times (\psi_1 + \psi_2) \times T}{T \times (T - T_\infty)}\right) \times [1 - \alpha(t)] \times (t - w)[1 - \alpha(w)]dw \tag{3-12}$$

where k_1 and $k_2$are rate constants, E_d and E_a are activation energies, ψ_1 and ψ_2 are material parameters and T_∞ is the temperature below which crystallisation stops. These parameters are adjusted through nonlinear regression to fit experimental data [87],[100], [102],[103].

Critics have raised concerns about the physical interpretation of some regression techniques and errors in the original equations [104].

To remove inconsistencies between the models and to accommodate different materials in a single framework, artificial neural networks can be trained from the models to model the processes from a data-driven perspective [105].

3.2.3 Practical Determination in the Following Experiments

In the context of MEX process-property relationships, the crystallisation process is primarily relevant for its influence on polymer diffusion across layer interfaces. While the precise mechanisms and morphology of crystal formation are well-documented, this work focuses not on how crystals form but on the point at which their formation inhibits diffusion. Diffusion, driven by entropy, competes with the thermodynamic minimisation of free enthalpy. Once crystallisation begins, this ceases, as the ordered crystalline phase restricts molecular mobility and effectively halts diffusion across the layer interface.

Modelling crystallisation under real-world process conditions is challenging. The MEX process is particularly complex for several reasons, including short fibre reinforcements that serve as nucleating agents, fibre lengths that vary dynamically due to the process, high shear forces and high pressures that influence both melting behaviour and molecular order. Furthermore, the cooling rates experienced during MEX are not constant and can vary significantly across the part and depending on extrusion line geometry. Combined with using materials specifically designed for slow crystallisation with multiple crystal phases, these factors complicate the application of existing theoretical models.

Crystallisation in the experiments conducted for this work is not predicted but directly measured to address these challenges. The thermal history during cooling is recorded in situ and then replicated in a DSC8500 by Perkin Elmer, Shelton, USA, which allows for high cooling rates similar to the real process. This method enables precise measurement of the onset of crystallisation during cooling and the total crystallinity formed during subsequent reheating at a constant rate. The samples used for these measurements are taken directly from printed parts to ensure that fibre lengths, orientations, and material compositions are consistent with real process conditions.

This approach allows for an accurate assessment of when crystallisation begins to impede diffusion without relying on theoretical predictions that may fail to capture the complexities of MEX. Correlating the thermal history with the observed crystallisation onset and degree of crystallinity provides a practical and reliable framework for understanding the influence of crystallisation on interlayer bonding in MEX parts.

3.3 Interlayer Fusion Bonding

MEX is rarely used for mechanically functional parts, mainly due to the considerable anisotropy caused by reduced mechanical properties across the layers [106], [107]. While this issue occurs with all polymers, it is most severe for high-temperature polymers and more challenging for semicrystalline polymers than amorphous polymers processed at comparable temperatures. The mechanical strength of the final part is highly dependent on the quality of the bond at the interfaces. This chapter introduces the mechanisms governing interlayer fusion bonding, mainly focusing on intimate contact and

molecular diffusion, known as healing, while modifying Butler et al.'s classic couple fusion bonding model [108] to reflect the process conditions for MEX.

3.3.1 Fusion Bonding Model

For polymer welding, the coupled fusion bonding model by Butler et al. [108] has been widely used to describe the joining of polymer parts by chain diffusion across the interface and is used here to describe the bonding processes occurring between the individual layers and lines of extruded materials.

The model is often used to describe iso-thermal welding processes, where both bonding partners are brought up to their welding temperature, either just above the glass transition temperature for amorphous polymers or above the melting temperature for semi-crystalline polymers. However, in its original publication, the model was also proposed for non-isothermal processes, and there has been good agreement on non-isothermal, non-isobaric tape placement processes.

The model describes two phases of polymer bonding, starting with contact development between the surfaces through the deformation of surface roughness and asperities, followed by the diffusion of polymer chains across the interface, returning to entropy and effectively dissolving the interface to bulk polymer.

The first phase describing the surfaces coming into intimate contact depends on the material's viscosity resisting deformation and the pressure applied to deform surface asperities and time. As polymer viscosity is a function of temperature, it is also temperature-dependent.

For D_{ic} two models are suggested. Asperities must be deformed through pressure and temperature if the surfaces are rough.

$$D_{ic}(t) = D_{ic}(0) * [1 + C \times \int_0^{t_p} \frac{P(t)}{\mu_{mf}} dt]^{1/5} \tag{3-13}$$

With $D_{ic}(0)$ being the initial degree of intimate contact and C a constant function of the surface structure. Different models have been proposed to model surface asperities [109], [110], [111], [112], [113]. μ_{mf} is the fibre-matrix viscosity. P(t) is the pressure field function.

For surfaces that are close enough for intermolecular forces to deform asperities and establish contact, surface wetting was suggested and modelled as nucleation and growth:

$$\phi(t) = 1 - \exp(-k_\phi t^{m_\phi}) \tag{3-14}$$

With $\phi(t)$ being the fraction of the surface area that is wetted. k_ϕ is a spreading constant dependent on extrusion temperature and, thereby, viscosity, flow rate and pressure of the extrudate and the roughness of the surface. The exponent m_ϕ describes the spreading

behaviour with $m_\phi = 1$ or linear spreading and $m_\phi < 1$ for slower, diffusion-limited spreading.

The second stage describes chain diffusion and welding or bond formation across the surface. It depends on the processing time and repetition time, also known as the relaxation time, which also is a temperature-dependent material property.

With D_h:

$$D_h(t) = \left(\frac{t}{t_{rep}}\right)^{1/4} \text{ for } t \leq t_{rep} \text{ otherwise } D_h(t) = 1 \tag{3-15}$$

The reptation time t_{rep} corresponds to the welding time necessary for diffusion to complete.

The coupled model can then be described as the achieved degree of bonding D_b at any given time t, being a function of the degree of intimate contact D_{ic} and the degree of healing D_h. All degrees are formulated between zero and unity.

$$D_b(t) = D_{ic}(0) \times D_h(t) + \int_0^t D_h(t - t') \times \dot{D}_{ic}(t')dt' \tag{3-16}$$

Building on surface wetting to describe the extrusion process in MEX, the spreading of the material under the nozzle could be modelled as a wetting effect. Looking at the cross-section and assuming a continuously occurring surface wetting along the toolpath, the problem becomes one-dimensional. With the material coming out of the nozzle with inner diameter D and wetting the surface until it has reached its final contact area a, the process could be modelled as initial contact or nucleation of the wetting process. The growth of the final contact area due to material flowing to the sides could be considered the wetting process. Equation 3-14 could then be reformulated to describe the process as follows:

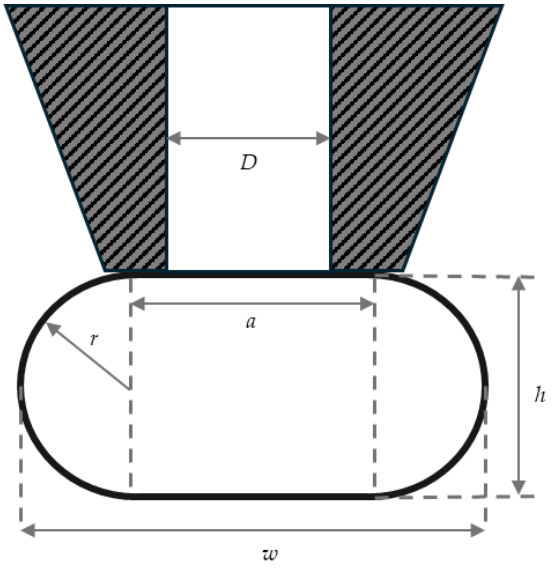

Figure 3-6: Extrusion line shape under nozzle

$$\phi(t) = \frac{D + (a - D) * \left(1 - \exp\left(-k_\phi t^{mm_\phi}\right)\right)}{w} \tag{3-17}$$

Or if the ridges are machined away and no macropores inside occur:

$$\phi(t) = \frac{D + (a - D) * (1 - \exp(-k_\phi t^{m_\phi}))}{a} \tag{3-18}$$

The material typically does not flow very far to the sides under the nozzle, and the flow is completed as the nozzle transitions, so the time scale is very short. For a nozzle diameter between 0.4- and 10 mm, print speeds are typically between 25- and 125-mm/s, and the time for wetting is about 0.4 s for a slow-moving large nozzle and 0.0032 s for a fast-moving small nozzle. With extrusion widths typically between 100 and 200% of the nozzle diameter, the initial contact is between 50 and 100%.

The process is, therefore, expected to be dominated by the healing of the interface. For this, the determination of the reptation time is critical.

3.3.2 Reptation & Approximating its Temperature Dependency

The reptation theory describes the diffusion process of polymer chains during healing, first introduced by De Gennes [114]. The prerequisite for applying reptation theory is that the molecular weight of the polymer exceeds the critical molecular weight, ensuring the entanglement of chains. Only large-scale molecular motions that change the topology of entanglements contribute significantly to bonding.

In De Gennes' reptation model, an entangled chain diffuses along its confining tube. The motion of the chain consists of the diffusion of small loops along the tube. The entanglements with surrounding chains hinder this motion less [115]. Figure 3-7 illustrates this molecular motion:

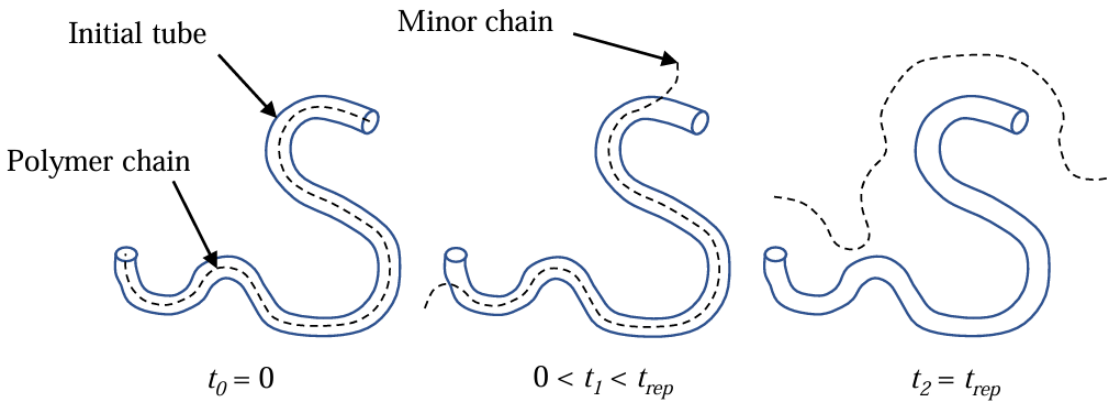

Figure 3-7: Molecular movement inside the Edwards tube [115]

- $t_0 = 0$: The chain is entirely confined by the initial tube, and the minor chain length is zero.
- $0 < t_1 < t_{rep}$: As the polymer softens at a temperature near or above the glass transition, the chain ends begin to diffuse and form minor chains. The minor chain length increases with time.

- $t_2 = t_{rep}$: At the reptation time, the minor chain length equals the entire tube length, completing diffusion [116], [117], [118].

In the reptation theory, the reptation time is the time required for a chain to escape the constraints of its initial tube [115]. The weld time is needed to dissolve the bond interface when diffusing across a layer interface.

Applying this concept to the healing process across an interface can be depicted as follows in Figure 3-8:

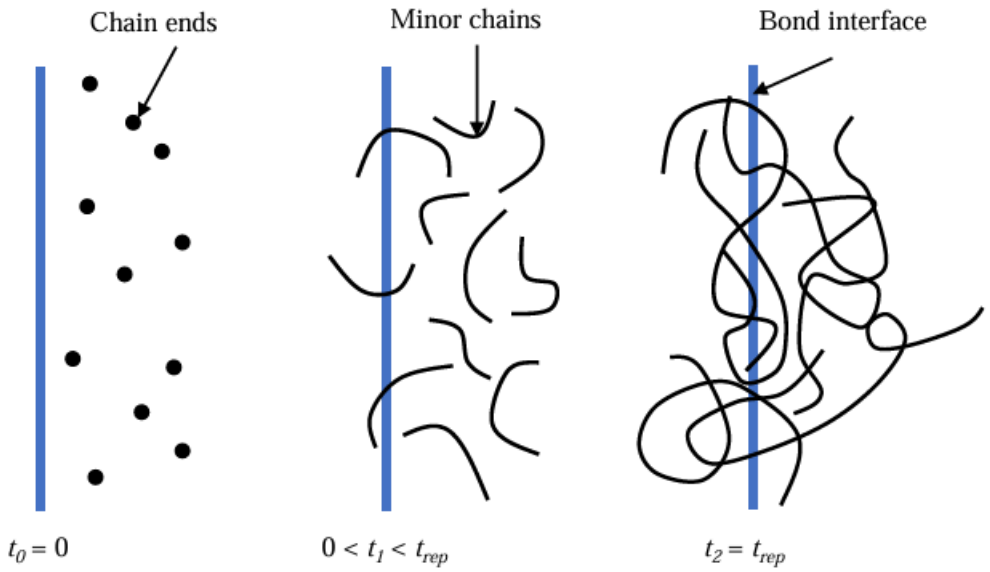

Figure 3-8: Diffusion of polymer chains across a bond interface

- $t_0 = 0$: No chain movement has occurred.
- $0 < t_1 < t_{rep}$: Minor chains diffuse across the interface, forming entanglements with chains from the adjacent layer.
- $t_2 = t_{rep}$: Full entanglement across the interface occurs, achieving maximum bonding strength [116], [117], [119].

However, it was suggested in the study by Butler et al. [108], referencing Wool [120], that the relaxation of an entangled network occurs faster than the relaxation of the individual chains. In the context of fusion bonding, the reorganisation of chains should not be considered a large-scale diffusion across the interface. Instead, it should be the relaxation of surface molecules from a higher energy surface state to a lower energy bulk state. With the mechanical relaxation time being related to the reptation time through the critical molar mass M_c of the chain:

$$t_m = t_{rep} \times (1 - \sqrt{\frac{M_c}{M}})^2 \tag{3-19}$$

PEEK's rod-like structure has a critical molecular weight, likely in the range of 10 to 20 kg/mol, and the molecular weight of PEEK types 150G, 450G and 650G by Victrex have been reported [121] as 26, 37 and 44 kg/mol respectively. This indicates that the fusion bonding of surfaces within t_m occurs significantly faster than the reptation, leading to the complete reorganisation of an entangled individual chain, according to De Gennes, within t_{rep}. [114], [122].

From here on, relaxation time is used synonymously with reptation time in the context of healing, and it depends on temperature. While many models assume healing to occur under isothermal or near isothermal conditions, MEX, with its high cooling rates, should be considered non-isothermal and modelled.

The relaxation time can be estimated through melt rheology [123], [124] in different ways:

The experimental relaxation time t_x is the time it takes for polymer chains to start losing memory of their initial configuration and begin to flow like a viscous liquid. It represents the minimum time for chains to start diffusing across the interface and for a bond to form at the molecular level. It is derived from the cross-over point in oscillatory rheology where the storage modulus G' equals the loss modulus G''. The experimental relaxation time has been successfully used by Bartolai et al. [125] for polycarbonate and acrylonitrile butadiene styrene.

The mechanical relaxation time t_m is the time required for the polymer chains to fully relax from their entangled state and move freely. Rheologically, it corresponds to the peak energy dissipation and full viscous behaviour, resulting in a Newtonian fluid. It provides a conservative estimate for the welding time, ensuring the bond reaches full molecular interdiffusion. It corresponds to the peak of the imaginary part of the complex viscosity $\eta'' = G'/\omega$, indicating the maximum energy dissipation due to friction.

Both these relaxation times can be derived from oscillating frequency sweeps in melt rheology as reciprocal of the frequency at the cross-point or maximum, respectively. Vega et al. [126] have studied relaxation times for linear polymers with ultra-high molecular weight and found that these two relaxation times, which were respectively shorter (t_x) and longer (t_m) than the more difficult to determine Rouse reptation time.

As the approach of Bartolai et al. [125] is valid for linear thermoplastic polymers, the approach can be applied to other MEX materials as well. However, in this work, t_m is used instead of t_x to gain a conservative estimate.

Measuring the relaxation time at low temperatures is difficult, especially below the crystallisation temperature in semi-crystalline polymers. Therefore, in this work, it is measured at high temperatures and then extrapolated to lower temperatures using the approach of Mansfield [127], who used the relaxation time to describe the glass transition

as the point where the chains become immobile, in this context ending the fusion bonding process. Mansfield used an empirical Vogel–Fulcher-Tammann (VFT) [128],[129] law fitted to the measured relaxation time:

$$t_{rep}(T) = A \times exp(\frac{B \times T_0}{T - T_0}) \tag{3-20}$$

A and B are constants, T is the temperature and T_0 is a threshold temperature at which the reptation time becomes infinite. In the Mansfield model, this is a temperature below, yet near, the glass transition temperature. For simplicity, it is assumed that the glass transition's lower onset is determined from DSC measurements.

Substituting this into the degree of healing of Equation 3-15 results in:

$$D_h(t,T) = (\frac{t}{A \times exp(\frac{B \times T_0}{T - T_0})})^{1/4} \tag{3-21}$$

Assuming then that the temperature under which the bonding occurs is time-dependent as the material cools results in:

$$D_h(t) = \int_0^t (\frac{t}{A \times exp(\frac{B \times T_0}{T(t) - T_0})})^{1/4} dt \tag{3-22}$$

Practically, the temperature will be measured during the process, and the temperature profile will be evaluated afterwards by integrating numerically the increase in healing over each measurement:

$$D_h(t) = \sum_0^{N-1} [\left(\frac{t_{i+1}}{A \times \exp\left(\frac{B \times T_0}{T(t_{i+1}) - T_0}\right)}\right)^{1/4} - \left(\frac{t_i}{A \times \exp\left(\frac{B \times T_0}{T(t_i) - T_0}\right)}\right)^{1/4}] \tag{3-23}$$

Until either D_h becomes 1 or the polymer chains stop diffusing. Either because the temperature is too low and t_{rep} becomes much larger than the time steps, or the chains lose mobility because of crystallisation, which will be the topic of the following subsection.

3.3.3 Pseudo-Amorphous Behaviour

So far, this work has assumed that relaxation slows because of temperature, and the threshold temperature is just below the glass transition temperature. This assumes that the polymers behave as amorphous during the observed time scales. The model by Butler et al. assumed that welding of semi-crystalline polymers occurs only above the melting temperature. Still, it has been observed, even for fast crystallising polymers, that the degree of bonding is underestimated for very high cooling rates when using the melting temperature as a threshold that stops the healing process [130].

During crystallisation, polymer chains align to form an ordered crystal structure, which locks them in position and reduces their mobility, thus impairing their ability to diffuse. The amorphous regions of the chains near the crystals also become less mobile due to their physical anchoring to the crystalline areas. Crystallisation in polymers is a time-dependent process. The nucleation and growth of crystalline regions require time, and faster cooling or shorter processing times can limit significant nucleation and growth. Additionally, surfaces can act as nucleation sites, accelerating crystallisation and further hindering the essential surface relaxation needed for healing.

As mentioned in chapter 2.3.1, polymers developed for AM often have a delayed or slowed crystallisation kinetic. For these polymers, the effect of healing below the melt temperature is expected to persist even at slower cooling rates. Some polymers are characterised as pseudo-amorphous, meaning they crystallise less readily, even in conditions where regular semi-crystalline counterparts would form crystals. If assumed that as long as the process conditions suppress crystallisation, the polymer will retain the characteristics of an amorphous material, being able to diffuse even at low temperatures. Suppression of crystallisation can occur either by a high cooling rate or over short periods until the nuclei have formed and crystals begin to grow.

Assuming that when crystals begin to grow chain, mobility is almost immediately affected, and the onset of crystallisation can be used as a threshold for stopping the healing process. That means crystallisation is suppressed for all cooling rates higher than the critical cooling rate.

Using the Avrami equation (3-7) to describe the onset of crystallisation, we can write:

$$t_{onset} = \frac{1}{k(T)} \times \left(\frac{1}{X_{Thr}}\right)^{1/n} \tag{3-24}$$

And the critical cooling rate $\dot{T}_{crit}$ as:

$$\dot{T}_{crit} = \frac{T_m - T_g}{t_{onset}} \tag{3-25}$$

With the melt equilibrium temperature T_m and T_g, or directly using the Ozawa Model (3-8):

$$\dot{T}_{crit} = \left(\frac{K_0(T) \times \Delta T^m}{-\ln\left(1 - X_{Thr}\right)}\right)^{1/m} \tag{3-26}$$

With the threshold for the crystallinity X_{Thr} being set at a low value, for example, 1%.

A semi-crystalline polymer will be assumed to exhibit pseudo-amorphous behaviour for the following conditions:

$$t < t_{onset} \quad \text{or} \quad \dot{T}_{crit} < \dot{T} \tag{3-27}$$

Because of the complexity of crystallisation of the extruded materials with carbon fibre reinforcement, high shear, high and non-constant cooling rates and complex polymer structure, it is difficult to determine these analytically or numerically. But as described in chapter 3.2.3, they can be measured relatively easily using fast DSC measurements, as will be done in the experimental validation.

3.3.4 The Material Extrusion Adapted Fusion Bonding Model

Summarising the last chapters and condensing it into the fusion bonding model, the degree of intimate contact is assumed to develop in a wetting manner under the nozzle in extremely short time frames and will be assumed instantaneous and complete. The analogous contact length between layers is not time-dependent and can be determined after printing if needed. If the ridges of the walls are machined away, this also falls out of the equation.

The degree of healing is formulated in a time and temperature-dependent form that uses a VFT approximation to extrapolate to temperatures below the melting temperature.

This approximation holds for as long as crystallisation has not begun.

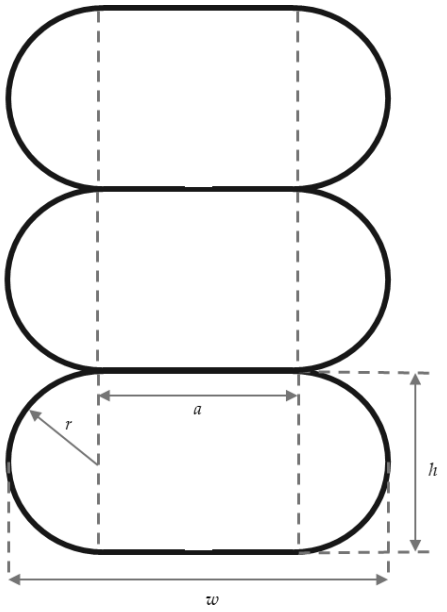

Figure 3-9: Sketch of a single walled print

For a single-walled printed wall, the strength across the layers σ_Z should then be described as:

$$\sigma_Z = \sigma_\perp \times \left(\frac{a}{w}\right) \times \int_0^{t_{onset}} \left(\frac{t}{A \times exp\left(\frac{B \times T_0}{T(t) - T_0}\right)}\right)^{1/4} dt \tag{3-28}$$

With:

- the strength of the fibre-reinforced polymer perpendicular to the fibre orientation $\sigma_\perp$,
- wall thickness w and length of contact between extrusion lines a, which becomes 1 for a machined specimen where the ridges have been machined off,
- VFT parameters A and B,
- the threshold temperature T_0, herein the lower onset of the glass transition and

- t_{onset} the time until the onset of crystallisation, or if $\dot{T}_{crit} < \dot{T}$, the time until the onset of the glass transition.

This sets the foundation for the design of experiments, which will need to determine these parameters during the MEX process.

4 Experimental Design

The experimental design will be introduced to validate the previously made considerations. This chapter will summarise the hypotheses and overall objective, followed by the materials selected for the experiments, the experimental setup, and the process parameters investigated.

4.1 Research Hypotheses and Objective

This research aims to deepen the understanding of process-property relationships in MEX, focusing on the influence of extrusion dynamics, crystallisation, and interlayer bonding on mechanical performance. This study hypothesises that MEX-printed parts' mechanical performance strongly depends on the interaction between material flow behaviour, fibre orientation, crystallisation kinetics, and the conditions under which layer fusion occurs.

The overarching objective of this research is to systematically understand and quantify the relationships between the process parameters of MEX and the resulting material properties, specifically focusing on:

- Material flow behaviour: Characterising the impact of flow dynamics on fibre alignment across the extrusion line cross-section.
- Thermal and rheological effects: Investigating the influence of the relaxation time and bonding processes during extrusion.
- Interlayer bonding: Understanding how crystallisation kinetics affect diffusion and the fusion bonding process at layer interfaces, particularly for high-performance thermoplastics and their composites.

This study aims to provide a comprehensive framework that supports the optimisation of MEX process settings to enhance mechanical performance, thereby advancing the industrial adoption of MEX for mechanically functional components.

Specifically, the following hypotheses will guide the investigation:

1. Material Flow and Fibre Alignment Behaviour in chapter 5.1:

   The fibre alignment during MEX can be predicted using Jeffery’s equation.
   Sub-hypothesis: A significant shift in fibre alignment occurs when the material experiences diverging flows, influencing the mechanical properties relative to the extrusion direction.

2. Mechanical Relaxation Time and Interlayer Bonding in chapter 5.2:

The mechanical relaxation time of polymers can be used as a reliable approximation for the welding time during interlayer bonding in MEX.
Sub-hypothesis: The relaxation time can be derived from rheological measurements and is temperature-dependent, following a VFT relationship for accurate predictions under cooling conditions.

3. Fusion Bonding of Pseudo-Amorphous Polymers at Low Temperatures in chapter 5.3:

   Pseudo-amorphous polymers can achieve interlayer bonding at temperatures below the melting point if cooling rates are high enough to delay crystallisation.
   Sub-hypothesis: The threshold temperature for bonding is determined by the onset of crystallisation, and bonding can persist as long as crystallisation is suppressed.

4.2 Process Effects, Parameters and Variables

This chapter outlines the key parameters affecting thermal and flow effects during MEX, which in turn affect the material properties. Additionally, parameters affecting thermal and flow-driven phenomena are identified and analysed to comprehensively understand their combined impact on the final part properties.

4.2.1 Flow Effect Driving Properties along X

Jeffery's equation has been introduced in chapter 3.1 to describe the shear rate, which is assumed to be the driving factor for fibre alignment in MEX. Fibre alignment is mainly expected within the XY plane, and fibres do not cross the extrusion line boundaries, but their alignment is critical to the material properties along X.

As introduced in Equation 3-6 previously, which is repeated below, the shear rate can be calculated as follows:

$$\dot{\gamma}_{xz} = \frac{v_d}{h} \times \left(1 - {A_d}/{A_e}\right) = v_d \times \left(\frac{1}{h} - \frac{h}{D^2} - \frac{4\times(w-h)}{\pi\times D^2}\right) \tag{3-6}$$

This shear rate affects the fibre alignment under the nozzle, meaning it could change within a single print if the extrusion conditions change. For this work, the conditions will be assumed constant within a single print. The extrusion process will, therefore, run as close as possible under stationary conditions whenever possible, avoiding changes in print speed or extrusion cross-section inside the tested volume.

From equation 3-6, it is clear that these parameters are expected to have an impact on the flow conditions driving fibre alignment:

Table 4-1: Parameters affecting the flow effects of the MEX process

Parameter	Description
Layer Height h	The layer height appears several times in the equation, and smaller layers cause a higher shear rate and, thus, more alignment as the flow becomes more convergent under the nozzle.
Extrusion Width w	Similarly, the layer width forces the material to flow to the sides under the nozzle, with high widths causing the flow to diverge and reducing the shear rate.
Deposition Speed v_d	The deposition speed, as setting the time frame for the flow, directly impacts the shear rate, with higher deposition speed leading to higher shear rates.
Nozzle Diameter D	The nozzle diameter also plays a role, as it determines the initial conditions before the material flows into the shape of the extrusion.

These four parameters have been plotted in Figure 3-2 and Figure 3-3 of chapter 3.1.2..

4.2.2 Thermal Effect Driving Properties along Z

In the MEX process, the thermal energy introduced by the deposition is balanced by the heat loss to the surrounding environment, mainly through convection and conduction to the lower layers and build platform. This equilibrium determines the temperature of the top layers, which drives thermal diffusion and crystallisation. The underlying mechanics determine the effect of layer interfaces and, therefore, the properties along the Z-axis.

The rate at which thermal energy is deposited has been introduced in a previous publication as “Enthalpy Deposition Rate”, the rate at which the total energy content of the deposited hot melt, which includes both internal energy and the work done by the material, is deposited on the part.

In a simplified assumption that the process runs under quasi-stationary conditions, this can be formulated as dependent on the volume flow of the deposition $\dot{V}$ and the temperature difference from the ambient ΔT:

$$\dot{H} = \rho \times \dot{V} \times c_p \times \Delta T \tag{4-1}$$

The quasi-stationary conditions assume that the print speed, part cross-section and extrusion line dimensions are constant and that the part is tall enough for the effect of conduction into the build plate to become negligible.

With the extrusion line cross-section, as previously introduced in equation 3-2 and sketched in Figure 2-13, the volume flow can be described as follows:

$$\dot{V} = (\pi \times ({}^{h}/_{2})^2 + h \times (w - h)) \times v_d \tag{4-2}$$

With the temperature difference of the extrusion temperature T_{Ex} and ambient temperature T_∞ the enthalpy deposition rate then becomes:

$$\dot{H} = \rho \times c_p \times (\pi \times ({}^{h}/_{2})^2 + h \times (w - h)) \times v_d \times (T_{Ex} - T_\infty) \tag{4-3}$$

From this, it is clear that these parameters are expected to have an impact on the thermal conditions driving layer bonding:

Table 4-2: Parameters affecting the thermal effects of the MEX process

Parameter	Description
Extrusion Temperature T_{Ex}	The effect of extrusion temperature is intuitive, and within the process window, it can be controlled. More accurately, this should describe the temperature of the extruded melt, which is often the measured temperature and can be affected by the federate of filament or screw RPM.
Ambient Temperature T_∞	The effect of ambient temperature is two-sided. While higher ambient temperature decreases the enthalpy deposition rate, it also reduces the heat loss of the part, with colder environments leading to faster cooling. It can be controlled to a certain extent with a heated build chamber. However, this is difficult in LFAM and will not be considered for this work.
Layer Height *h*	Layer height is an often-used parameter to increase the productivity of the machines. Taller layers deposit more material at the same deposition speed. However, the taller layers reduce the surface quality and lead to deeper ridges that reduce the relative contact area between the layers in a wall if the part is not machined. In this work, it will be controlled, but walls will be machined to eliminate the effect of reduced contact areas.
Extrusion Width *w*	The effect of the extrusion width is analogous to the layer height. However, a wider line at a constant layer height would lead to better contact, which again will be ignored by milling the surfaces.

Deposition Speed v_d	The deposition speed also directly impacts the volumetric output rate, with higher speed depositing more material and thus more heat. It can be controlled over a wide range during processing but should stay constant to ensure quasi-stationary conditions.
Volumetric Heat Capacity of the Material $\rho \times c_p$	Finally, the volumetric heat capacity of the material itself is an influencing factor, though typically not easily modified without affecting the intended application of the part. As standard reinforcement, carbon fibres have higher density but lower heat capacity than polymers like PEEK.

All these parameters positively impact the enthalpy deposition rate, except for the ambient temperature, which will not be controlled. The volumetric heat capacity of the material will also not be varied as it is typically not a process parameter that can easily be changed. Results are always compared with the same or at least a similar material to eliminate any impact.

4.2.3 Interactions between Thermal and Flow Effects

From the previous two chapters, it is clear there are several interactions between the thermal and flow effects. When optimising process parameters for one, there is likely to be an impact on the other, making the process-property relationships complex.

For example, while designing the fibre alignment at its maximum to optimise for strength or CTE along X, one would try to maximise deposition speed and minimise layer height, line width and nozzle diameter. However, this would negatively impact the enthalpy deposition rate and, therefore, likely the layer bonding.

However, designing the process for both can succeed if the whole picture is considered and the impact of each process parameter on the flow and thermal effects and their effect, in turn, on the material properties are understood.

This would give a foundation to design the process to match the requirements of the process and tailor material properties as needed, contributing to the industrial adoption of MEX as a production technology.

4.3 Material Selection, Sample Preparation, Methods & Equipment (MSME)

This chapter will outline the materials, sample geometry and preparation, and equipment used for each of the experiment sets in chapter 5 separately.

As the work occurred in the context of aerospace research, the material was chosen as a carbon fibre-reinforced PAEK due to its relevance in current and potential for future

applications. While initial material flow investigations are done on an easy-to-process and cheap standard FFF filament material, PETG, the aim is to validate the results on the PAEK.

4.3.1 MSME for Material Flow and Fibre Alignment Behaviour

This study is a combination of work published in studies that have undergone peer review in "Polymers" by MDPI, Basel, Switzerland, [131], [132].

The first part of the study based on FFF used the following setup:

A 20% carbon fibre-reinforced PETG filament by "Formfutura" named "CarbonFil" was used. High fibre content was chosen to maximise the effect of changes in fibre alignment on material properties, and an amorphous matrix was chosen to minimise crossover effects from matrix welding. A high fibre content was expected to give a more accurate result when measuring fibre misalignment, as more fibres would be visible in the cross-sections.

The "CarbonFil" material was dried for five hours at 65 °C before printing the specimens and kept in a box with a moisture absorber during printing. According to the manufacturer data sheet, the material has a density of 1.19 g/cm^3, water absorption of 0.13%, tensile strength of 52.5 MPa, tensile modulus of 3800 MPa and Vicat softening temperature of 85 °C at 0.455 MPa. Print temperatures are recommended at 230 to 265 °C for the extruder and up to 85 °C for the print bed.

Specimens were printed on a modified delta printer based on a Tevo, China, "Little Monster" running on a "Duet2" control board by Duet3D Ltd, Peterborough, UK, with an E3D-Online, London, UK, "Volcano" hot end with 60 W heating power and a type K thermocouple for temperature control using stainless steel nozzles. The build chamber was enclosed with 4mm PMMA sheets but not heated. The print bed was heated with a 400 W silicone heater controlled by a 100 kΩ thermistor underneath a glass plate. Temperatures were set at 265 °C for the extruder and 75 °C for the print bed, within the recommended range. The extruder temperature was chosen as high as possible to minimise the viscosity and allow maximum material flow. The bed temperature was high but below the Vicat softening temperature to ensure bed adhesion and allow the material to solidify and stabilise the extrusion lines.

Samples were produced by printing one cube of 35 mm sides of a single extrusion line wall for each of the 30 parameter sets. All parameter sets of the same nozzle diameter were nested and printed simultaneously. This ensures the previous layer cools sufficiently and maintains its shape before the next layer is extruded, ensuring all samples are printed under consistent conditions. To identify the cubes after printing, each was printed with the experiment number embossed on one of the sides by 0.1 mm, which

was visible after printing. They were printed as single walls to avoid interactions between the extrusion lines within a layer.

After printing the cubes, the first analysis step was surface scanning using a Keyence, Osaka, Japan, VR500. This 3D scanner with a measurement accuracy of height profiles of ±2.5 µm was used for the extrusion line shapes and wall surface roughness. Width accuracy was ±2 µm, used for measuring the actual line width. The extrusion line was scanned in the XY plane, and the walls of the cubes were in the XZ plane. This method allows for measuring the width, height profile, shape of the extrusion line, and their effects on the surface roughness of the walls. The surface roughness is influenced by the layer height and artefacts that may occur due to unstable extrusion. Using automated batch analysis and edge detection of the scans to orient the specimens in the measurement ensured that the surface roughness measurements in XZ were always performed on the same area in the same central region of the wall, leaving space for the corners. These measurements were performed to ensure process stability when selecting the parameter sets of highest and lowest fibre misalignment by ensuring the processes were also stable and repeatable.

3D scans determine height maps. The layer lines influence uneven structure. This is a repeating surface waviness rather than random roughness. However, surface artefacts caused by unstable extrusion lines can significantly add roughness. This is an actual roughness, as the artefacts result from sharp, jagged edges of unstable extrusion lines. Figure 4-1 shows three examples of surfaces with colour-coded height profiles.

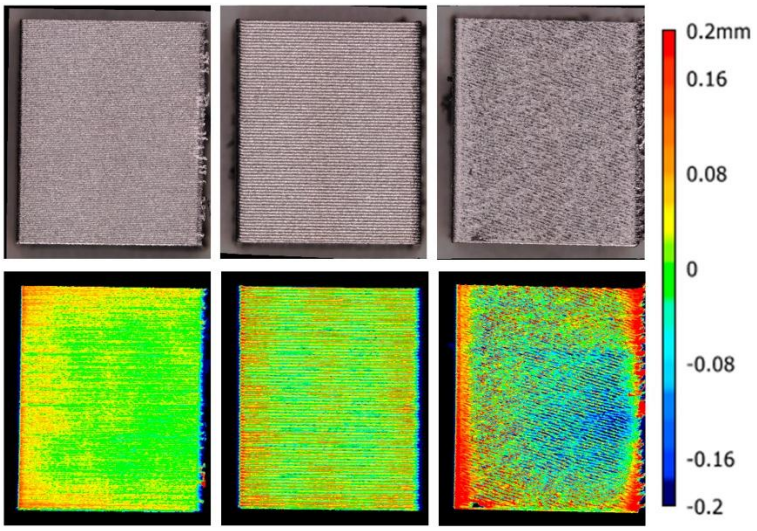

Figure 4-1: Examples of surface roughness in scans

After scanning, one of the walls was cut from the cube and embedded in epoxy resin. This was ground and polished to obtain cross-sections of the XY plane for fibre orientation and the XZ and XY planes to confirm that the fibre orientation was mainly in the XY plane, as expected and reported in the literature [76]. This was the case.

The orientation of the individual fibres within the extrusion line was measured to measure the fibre misalignment. For this, microscope images were taken of the polished cross-section using 10× magnification and multiple image alignment on an "Olympus BX41M" incident light optical microscope by Evident, Tokyo, Japan, to show the entire width of the extrusion line.

A Python 3.9 program was used to measure the orientation of the individual fibres, which:

- Transformed the image colours into a grayscale.
- A threshold was applied to transform the grayscale images into a binary of white fibres and black surroundings.
- Identified objects of white pixels and applied a threshold to delete smaller objects to filter and remove reflections of scratches or particles. In this case, a threshold of 21 μm^2 was used.
- Calculated the object location to calculate the length of the main axis, the width perpendicular to it and orientation.
- It then classified the objects into fibres and large particles by considering objects with a length-to-width ratio of 3:1 a fibre and everything else a particle.
- Finally, it outputs the length and orientation distribution of the three classes, objects, fibres and particles, to create plots of different statistical visualisations, such as histograms and cumulative curves, and save the data of the objects.

As the histograms of the individual fibre orientations from the X axis proved to be normal distributions around the X axis, the misalignment of fibres can be described using the standard deviation of the distribution. This was repeated at three cube positions to consider local variations, and the results were averaged for the fibre misalignment.

After the experiments, the parameter sets with the highest and lowest fibre orientation and a stable extrusion process were chosen to print tensile test specimens for testing along X and Y using digital image correlation (DIC) to observe the strain. All cubes and tensile test specimens were printed from the same roll of material to avoid differences between batches affecting the results. This was to investigate the effect the fibre misalignment can have on the mechanical properties over tensile specimens as a whole, but also at the level of individual extrusion lines using the strain field to visualise the extrusion line interfaces when testing along Y.

Three specimens were printed with each parameter set, and for each testing direction, X and Y. Specimens were printed without perimeters around the outside using only parallel lines to avoid having perimeters Y specimens influencing the mechanical properties. Dimensions were 150 mm × 24 mm × 2.4 mm in X × Y × Z. Width, and height were chosen to allow for a whole number of lines and layers to be printed for both parameter sets. The specimens were smoothed with 240-grain sandpaper. Twelve specimens were

airbrushed on the surface with a stochastic black-and-white pattern that could be observed using DIC. The universal test machine was a “100 kN UPM” by Hegewald & Peschke, Neu-Ulm, Germany, using a 10 kN load cell. DIC was performed using a GOM, later acquired by Carl Zeiss IQS Deutschland GmbH, Oberkochen, Germany, “ATOS Capsule” in “Aramis “mode. For the stress-strain curves, a virtual extensometer was calculated in DIC over a length of 25 mm. The strain field was also calculated and used to check for local differences in strain of the specimens.

Data from the LFAM process was later collected when the samples for Fusion Bonding of Pseudo-Amorphous Polymers at Low Temperatures were produced as part of those samples. A description of the materials and machines is part of 4.3.3 and is included there.

4.3.2 MSME for Mechanical Relaxation Time and Interlayer Bonding

The study was published and has undergone peer review in “Polymers International” by John Wiley & Sons, Inc., Hoboken, USA, [133]. The description of materials is taken from there and reduced to the relevant section.

The materials used in this study were supplied by Victrex plc, Thornton Cleveleys, UK, and have been designed for AM. Compared to PEEK for injection moulding, the PAEKs for AM have lower melting points and, more importantly, a considerably slower crystallisation behaviour, showing pseudo-amorphous behaviour. A slowly crystallising and an intermediately fast crystallising PAEK are used as unreinforced filaments for small-scale trials.

For large-scale printing, the slowly crystallising material is compounded with 20% short carbon fibre reinforcements and is processed in 3D printing directly from pellets.

As reference materials, Victrex's 450G PEEK is used for the unreinforced filaments, and the 30% carbon fibre-reinforced version 450CA30 is used for large-scale AM. These reference materials have been well documented in the literature, which allows comparability to previous studies. Figure 4-2 shows, from left to right, the slow crystallising PAEK, the intermediate crystallising PAEK and the fast-crystallising reference 450G PEEK. The slower the materials crystallise, the more transparent and darker they appear due to the lower crystallinity. They are described in Table 4-3.

Figure 4-2: Filament materials used for the validation of hypothesis 2

In contrast to the AM materials, they have a fast crystallisation behaviour, initially intended to shorten the cycle time for injection moulded parts. The intermediately fast crystallising material has since been brought to market under the Victrex trade name AM200.

Table 4-3: List and description of materials used in the study for hypothesis 2

Polymer	**Crystallisation speed**	**Melting point**	**Type**
Victrex 450G	High	343 °C	Commercial general-purpose PEEK grade, in filament form
Victrex 450CA30	High	343 °C	Commercial PEEK compound, with 30% chopped carbon fibre, in pellet form
Victrex IC-PAEK / AM200	Intermediate	304 °C	Commercial AM-specific polymer in filament form. Based on PEEK-PEDEK copolymer
Victrex SC-PAEK	Low (Slow Crystallising, SC)	310–330 °C	Development Type AM-specific polymer, in filament form. Based on PEEK-PEDEK copolymer
Victrex SC-PAEK-20%CF	Low	310–330 °C	Development Type AM-specific compound, in pellet form. Based on PEEK-PEDEK copolymer with 20% carbon fibre

Comparative DSC measurements of the materials at 10 K/min show a clear difference in their crystallisation speed in Figure 4-3. The 450G reference (black line) crystallises at a much higher temperature and in a sharper peak than the intermediate crystallising (blue), which in turn is at a higher temperature and sharper peak than the slow crystallising PAEK (green). The red line is the 20% carbon-filled slow crystallising PAEK, showing that the fibres don't accelerate the crystallisation but reduce the enthalpy as less polymer is in the same weight. This was unexpected, considering carbon fibres are known to affect PEEK.

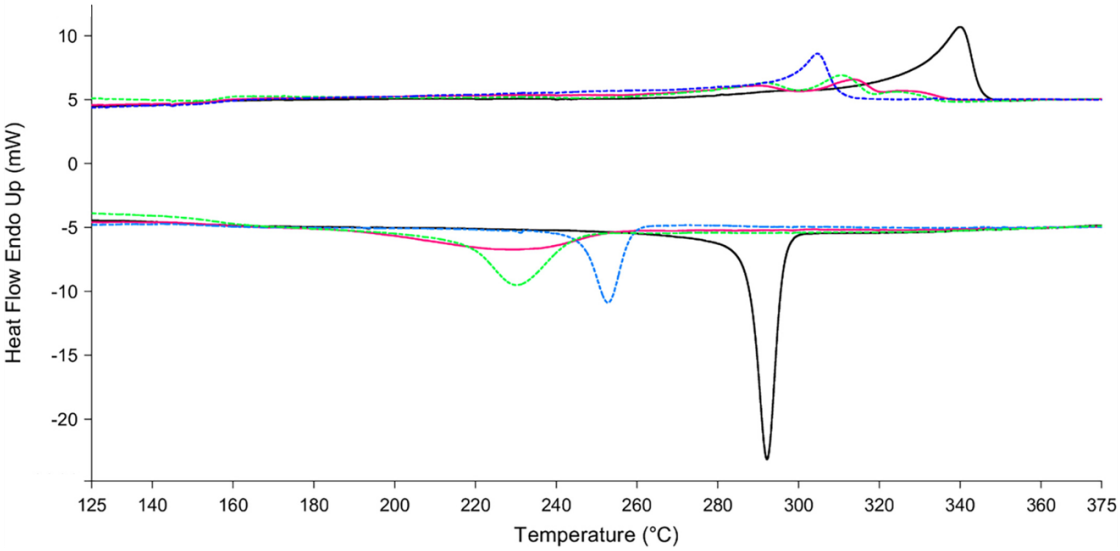

Figure 4-3: Measured at 10K/min

The characteristic temperatures for the three materials are listed in Table 4-4 below:

Table 4-4: Characteristic temperatures of the materials of Hypothesis 2

	SC-PAEK	**IC-PAEK**	**450G**
T_g *(Onset) (°C)*	152	151	143
T_m *(°C)*	310	303	343
T_c *(°C)*	238	249	292

All materials were dried before being printed to remove any absorbed humidity, and the pellet materials were also annealed at 180 °C for at least six hours. The filaments were dried in a convection oven and removed just before printing while stored in a cardboard container with a moisture absorber. The pellet materials in a Vismec, Padua, Italy, DP80 dryer and fed directly to the single screw extruder by an air conveyor. As the effects on the interlaminar strength are expected to be most significant for larger differences in crystallisation speed, 450CA30 and the fibre-reinforced compound of the slow crystal-lising PAEK were used for the experiments on the large-scale printer after initial trials on a filament printer showed promising improvements to the interlaminar bond strength.

The samples used for mechanical testing by three-point bending were produced on two machines. Initial small-scale tests on the unreinforced polymer were conducted on the delta-type filament printer mentioned in the previous chapter. A wall of 60 mm width and 80 mm height by 5 mm thickness is produced, out of which five specimens are cut in the Z direction and then polished on all sides to avoid effects caused by the surface roughness. Extrusion line dimensions were 1 mm extrusion width by 0.4 mm layer height extruded at 450 °C onto a heated printing bed at 150 °C for the first layer, which

then cooled to 135 °C for the following layers. The deposition speed was set to complete a layer in 10 s, resulting in a print speed of 40 mm s^{-1}.

Specimens from the large-scale system were produced by printing a cube of 300 mm wall length and 16 mm wall thickness on an AM Flexbot by CEAD Group B.V., Delft, Netherlands, with a G25 extrusion unit, consisting of a single screw extruder with 25 mm screw diameter and a five cc volumetric gear pump for accurate material dispensing, using a 6 mm nozzle and printing an 8 mm wide extrusion line with 2 mm layer height using a Comau, Turin, Italy, "NJ130-2.0" robot run by a Siemens, Munich, Germany, "Sinumerik 840D" in a 5 × 4.5 m double-walled laser protection cell.

The printing speed was reduced to complete a layer in 60 s to indicate the strength achievable in larger prints. For this, the printer was programmed with a maximum speed of 200 mm s−1, but the slicer was allowed to reduce the speed where necessary to ensure a layer time of 60 s, which resulted in a print speed of 32.5 mm s^{-1} for the walls. The extrusion temperature was 405 °C on a heated printing bed at 105 °C. The wall thickness was chosen to increase the printing speed to a more realistic value and to consider the influence of neighbouring extrusion lines on the temperature. The walls were then cut into plates that were machined smooth, and specimens were cut from them in the *Z* direction using a CNC mill to test the interface between the layers. They were tested on the same universal test machine described in the previous chapter.

Specimens were cut from a cube or wall rather than be printed individually as the resulting mechanical properties depend on the print geometry, with a constant cross-section giving more reliable results [134]. A wall was chosen in the FFF setup as printing an entire cube would require significantly longer layer times and more material.

All printed parts were annealed at 200 °C for two hours after printing to ensure complete crystallisation in the specimens and make differences in strength directly relatable to layer interfaces rather than different degrees of crystallinity, which also influence the mechanical properties [135]. The already separated walls were placed on an 8 mm aluminium plate, vacuum bagged, and maintained under vacuum the entire time while in the oven before being machined into the test specimens. Specimens for mechanical testing by three-point bending were 80 mm long, 4 mm thick and 10 mm wide per DIN EN ISO 178 and tested on a Hegewald & Peschke 250 kN universal test machine with a span of 64 mm at a testing speed of 2 mm/min using a 20 kN load cell.

The modelling of the degree of healing requires information on three aspects: the interface temperature at which the bonding occurs, the corresponding welding time at this temperature, and whether the material is amorphous or semi-crystalline, which determines whether healing can occur. The temperature is determined by a thin type K thermocouple with 0.08 mm wires (Omega 5SRTC-TT-KI-40-1M) placed between the layers during printing.

To measure the onset of crystallisation, a PerkinElmer DSC8500 was used, which can achieve cooling rates of up to 750 K/min. This allows the crystallisation to be recreated

at the cooling rates measured during the additive extrusion process of the specimens. The thermal history measured during printing is used and programmed into the differential scanning calorimeter.

The welding times are determined by measuring the mechanical relaxation time and fitting the measurements with a VFT law, as previously introduced. The samples for the rheology experiments had the shape of a disc with a diameter of 25 mm and a height of 1.1 mm. They were produced by FFF. Oscillatory frequency sweeps in a plate-plate measuring system with a heated measurement chamber on an MCR302 rheometer by Anton Paar, Ostfildern, Austria, were used to determine the complex viscosity. The samples were first heated above the melting temperature, then cooled to the measurement temperature and the frequency sweep was performed from high to low frequency. This was done from high to low measurement temperatures, starting at 360°C and reducing it until the measurement could no longer be completed before crystallisation set in.

The curve fit function of Python's "SciPy" library was used to determine the A and B coefficients of the Vogel–Fulcher law; T_0 was chosen as the onset of the glass transition during heating.

4.3.3 MSME for Fusion Bonding of Pseudo-Amorphous Polymers at Low Temperatures

The study was published and has undergone peer review in "Polymers" by MDPI, Basel, Switzerland [132]. The description of materials is taken from there and reduced to the relevant section.

The material used is a 30 wt.% short carbon fibre-reinforced PAEK developed for AM by Victrex, the same base polymer as in the previous chapter before but with higher fibre content. The material was dried for at least eight hours at 120 °C in the DP80 dryer and fed directly to the single screw extruder by an air conveyor. The AM Flexbot, described previously, was used to manufacture the samples.

An 8 mm brass nozzle was used for printing. The heat zones were set to 330 °C and 350 °C for the first two, with the remaining three zones (extruder zone 3, gear pump, and nozzle) set to the values of the design of experiments. The print bed was heated to 100 °C, and the machine was enclosed in a protective cell that maintained an average ambient temperature of 31 °C (minimum 25 °C, maximum 33 °C) during printing; the ambient temperature for each print was recorded.

Sample geometry was chosen as cubes with 300 mm edge length, and corners rounded to 50 mm radii in the printing plane, printed in a spiral mode. This yielded 200 mm by 300 mm flat plates on each side for sample preparation and allowed the extrusion under almost stationary conditions.

For this, the cubes were separated into the four side planes. One was used for coupons for fibre orientation analysis, and two were used to make coupons for mechanical testing

by 3-point bending. The coupons for mechanical testing were cut on one along X and the other along Z. This allowed for testing of fibre-dominated behaviour along X and matrix-dominated behaviour along Z. The fibre alignment and porosity analysis specimens were cut so the XY and YZ planes were visible, and fibre alignment was determined in XY and porosity in YZ. The remaining plate had the thermocouple inside and was used for DSC analysis samples. The crystallisation was then reproduced with the respective cube's material and approximate thermal history.

Coupons for mechanical testing were machined from the plates by machining both sides of the plate flat to remove layer lines and then cutting the specimens by contour milling. The resulting coupons were smooth on all sides to avoid the notch effects of the layers influencing mechanical characterisation and provide a homogeneous specimen shape throughout extrusion width and height settings. Flood cooling minimises the temperature increase during milling, which could weld the layers and affect the measured layer bonding. Samples were dried and then conditioned at 23 °C and 50% humidity for at least 48 h and kept in the climate chamber until their testing.

Mechanical testing was performed by 3-point bending on a universal test machine, a UPM250 by Hegewald & Peschke. The loads were measured using a 5 kN load cell, and deflection was measured using a DK830SLR extensometer by Magnescale, Tokyo, Japan. Conditioned specimens were removed from the climate chamber as a set and immediately tested. Six specimens were evaluated per orientation for each parameter set.

For the additional data for the fibre alignment, cross-section microscopy samples were embedded in transparent epoxy resin for stabilisation before polishing. Polishing was conducted in steps on a water-lubricated disc grinder using silicon carbide sandpaper in grit steps of 180, 320, 800, 1200, 2400, and 4000 to achieve scratch-free surfaces for analysis. The cross-sections were recorded on an Olympus BX41M incident light optical microscope with a 10× magnification and automatic multiple-image alignment to record the entire extrusion line width in one image. Five specimens were imaged per parameter set. Analysis was conducted using the greyscale analysing program previously described.

The temperature of the part during the printing process was recorded in two ways. An infrared camera, a Teledyne FLIR, Wilsonville, USA, a325sc, was positioned to observe the printed specimens horizontally. Additionally, thermocouples were introduced into the print by placing them on top of a printed line and holding them in place. At the same time, the next layer was deposited on top and solidified, fixing the thermocouple in place. The measurements yielded a surface and core temperature for the printed lines. They were used subsequently to analyse assumed surface-temperature-based bonding between layers and core-temperature-based crystallisation of the polymer by replicating the measured thermal history.

DSC measurements were performed to accurately recreate the LFAM process's thermal history. The DSC measurements were performed to investigate the occurrence of crystallisation during the cooling cycle and determine if the behaviour was pseudo-amorphous.

The thermocouples introduced during printing provided time-continuous temperature data that allowed the replication of the three distinct cooling phases experienced by the material during printing.

The three cooling phases consisted of the following:

1. Quench-cooling: After extrusion, the fresh molten material immediately comes into contact with the print surface, leading to rapid quench-cooling. During this phase, the material was rapidly cooled to an elevated temperature slightly below the extrusion temperature. In Figure 4-4, this corresponds to the drop in the extrusion temperature of 350 °C to the maximum recorded temperature of 260 °C. This occurs within 15 s from the first onset temperature increase at −15s and corresponds to a 360 K/min cooling rate in this example.
2. Fast Cooling: Once the layer was deposited and free on three sides, fast cooling occurred to a second, lower temperature at time 0 to 90 s in Figure 4-4 to 170 °C. In the example shown, cooling rates during this phase were between 60 and 120 K/min at a relatively low rate of 60 K/min compared to the other experiments.
3. Slow Cooling: After the next layer was deposited, after a short increase in temperature, the cooling rate of the material, now only free on its sides, was reduced. This slower cooling phase could provide sufficient time for the material to crystallise if the transition to the slow phase occurred at a high enough temperature. In the example, cooling rates in this phase were lower than 25 K/min, from 120 s onwards at, on average, 15 K/min until 360 s.

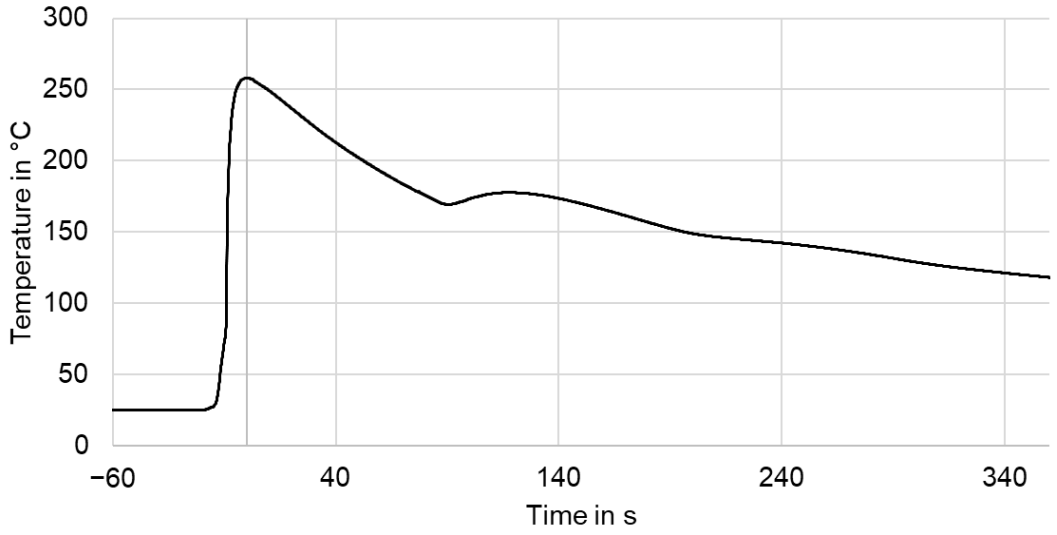

Figure 4-4: Example of a cooling curve in LFAM

To recreate the three observed cooling phases, the PerkinElmer DSC8500 was used again.

The cooling profiles were set to begin after a five-minute isothermal step at the extrusion temperature with a so-called “ballistic cooling” step in the instrument settings, which is uncontrolled cooling at the maximum achievable rate of the instrument to the first target temperature. From there, constant cooling occurred at the average rate of phase 2 to the temperature at which the next layer was deposited, determined by the lowest temperature measured by the thermocouple before the spike in temperature from the deposition. The last cooling step was conducted with the cooling rate determined by the pre-deposition temperature and the temperature recorded three minutes later. The sample was cooled at this rate until 120 °C, below the glass transition temperature. At that point, no more crystallisation was expected, and it was held there in a two-minute isothermal step, allowing the sample and instrument to settle before beginning a heating cycle at a constant 20 K/min to the extrusion temperature.

During cooling, the temperatures of onset, peak, and end of crystallisation were observed. During heating, the melt enthalpy of crystals formed was determined. As the DSC is only calibrated for one heating rate, the temperatures determined during the cooling cycles may be less accurate than those specified during heating. However, as crystallisation generally occurred during the last stage of cooling at rates lower than 25 K/min, and the instrument was calibrated for the 20 K/min of the heating cycle, the expected error is smaller than 1 K, which was accepted.

5 Experimental Results and Discussion

5.1 Material Flow and Fibre Alignment Behaviour

The first hypothesis was that the fibre alignment during MEX can be predicted using Jeffery's equation, with the sub-hypothesis that a significant shift in fibre alignment due to flow conditions will influence the mechanical properties relative to the extrusion direction.

5.1.1 Fused Filament Fabrication Experimental Results

The results of the chapter were part of a previous publication [131] and have undergone peer review, as mentioned in 4.3.1.. A detailed table of all results can be found in the publication. The identified relevant parameters of chapter 4.2.1 were the nozzle diameter D, layer height h, extrusion line width w and deposition speed v_d. For the first experimental set, these were varied in the FFF process using the described 20% carbon fibre-reinforced PETG. Extrusion line width and layer height were chosen relative to the nozzle diameter rather than in absolute values to avoid extrusion line widths smaller than the nozzle or layer heights larger than the nozzle.

An extrusion width of 100% of the nozzle diameter results in a flow similar to the planar flow described in [77], [79], while a 200% extrusion width has a strongly divergent flow. Based on previous experiments, layer height was chosen by experience, where values larger than 60% of the nozzle resulted in poor contact with the last layer. The lower limit was dictated by the printer's step resolution of 0.08 mm and smallest nozzle of 0.4 mm, giving a minimum layer height to nozzle diameter of 20%.

Deposition speed was chosen low to ensure even large extrusion lines could be printed at maximum speed without overloading the extruder or hotend.

The parameter limits were as follows in Table 5-1:

Table 5-1: Parameter settings for Hypothesis 1 experiments

Parameter	**Lower Limit**	**Upper Limit**
Extrusion line width w / D	100 %	200 %

Layer height h /D	20	60 %
Nozzle diameter D	0.4 mm	0.8 mm
Deposition speed v_d.	15 mm/s	25 mm/s

This resulted in a shear rate between -45 and 236 s^{-1}, calculated according to equation 3-6, though the sample printed at 236 s^{-1} failed during printing. The highest shear rate among successful prints was 157 s^{-1}

The fibre alignment inside the filament was also measured as inlet orientation and found to have a standard deviation of only 5.4° from the extrusion direction, indicating very high alignment.

Scans of the line surface in the XY plane and the cube walls showed that the shear rate had a visible impact on the extrusion shape. For this, one of the edges was selected, and a perpendicular height profile was measured and averaged with five offset profiles in each direction for 11 measurements.

Shear rates < 23 s^{-1} lead to a convex top surface of the extrusion line, as can be seen in Figure 5-1 below.

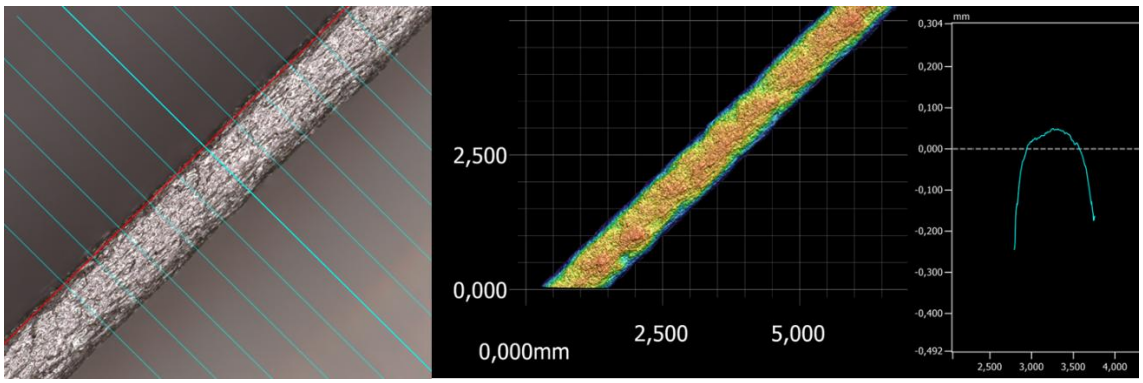

Figure 5-1: Example of an extrusion line with a convex shape

This extrusion shape led to walls where the ridges were visible and determined the surface structure, with the height map showing the lines clearly as well as shown in the side view of the above example shown in Figure 5-2. The surface had regular repeating patterns due to the ridges. Surface roughness S_A was 21.26 µm.

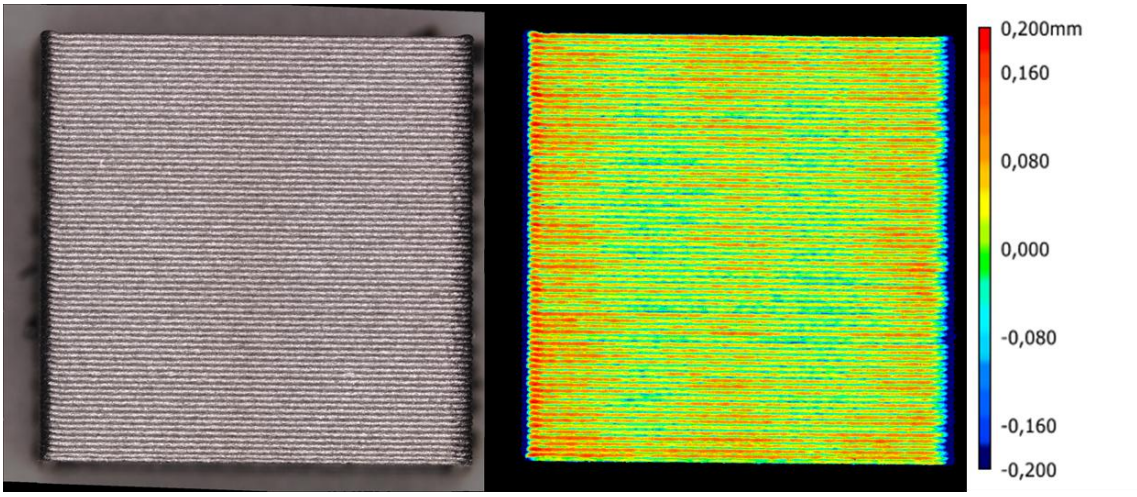

Figure 5-2: Side view and height map of a convex line type

Shear rates between 23 and 70 s^{-1} led to a change in extrusion line shape to a concave top surface, as can be seen Figure 5-3 below:

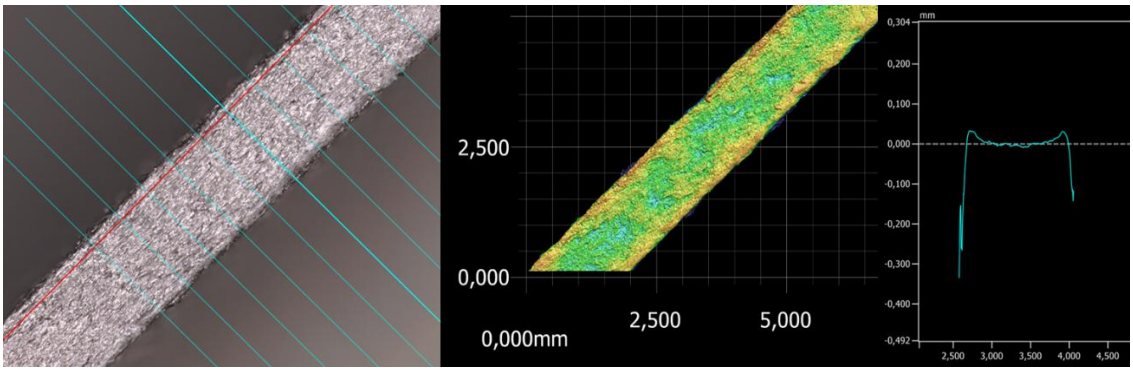

Figure 5-3: Example of an extrusion line with a concave shape

This extrusion shape led to walls where the ridges were still visible in the surface structure, but the height map shows many artefacts that appear, almost as noise. The surface was still relatively smooth, and the artefacts hid the layer lines, as can be seen in Figure 5-4. Surface roughness S_A was 34.6 µm, meaning that, even though the surface appears more even, it is rougher than the previous example with convex lines and clear layer lines.

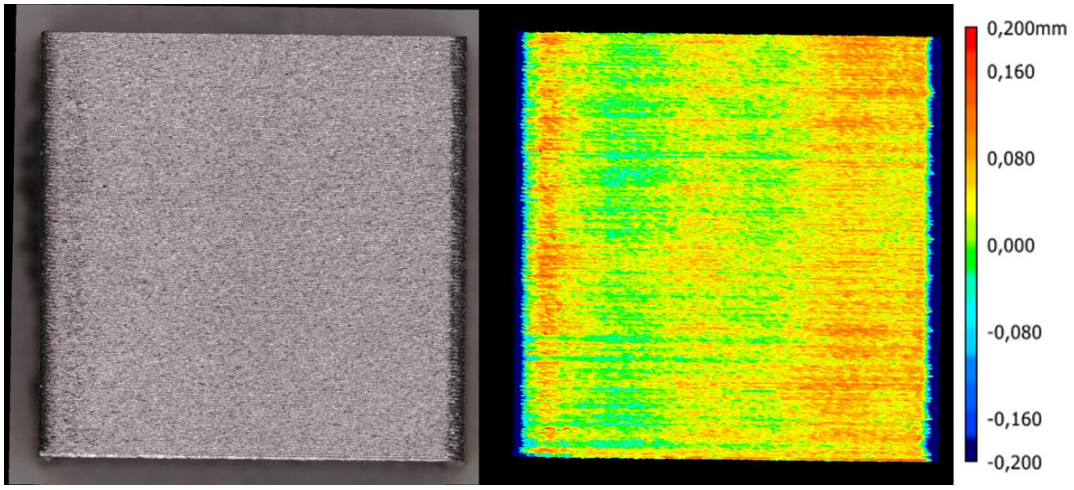

Figure 5-4: Side view and height map of a concave line type

Shear rates larger than 70 s^{-1} led to another change in extrusion line shape to a jagged top surface, where material appeared to be torn off the line in regular intervals, as can be seen in an extreme example in Figure 5-5 below:

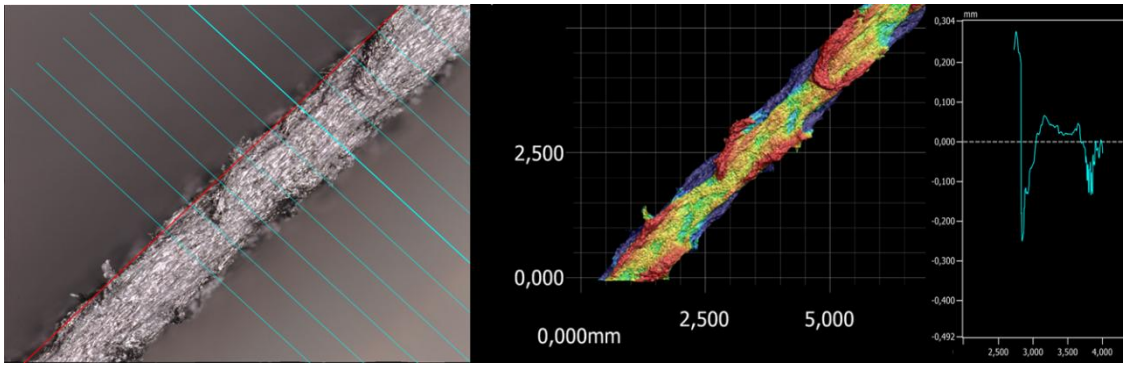

Figure 5-5: Example of an extrusion line with a jagged shape

This extrusion shape led to walls that were covered in artefacts that were very rough and irregular. The artefacts seemed to accumulate to form diagonal lines, likely where torn-off material adhered to jagged edges of the layer below. The layer lines were no longer visible, as can be seen in Figure 5-4. Surface roughness S_A was 72.3 µm, significantly higher than in the previous examples.

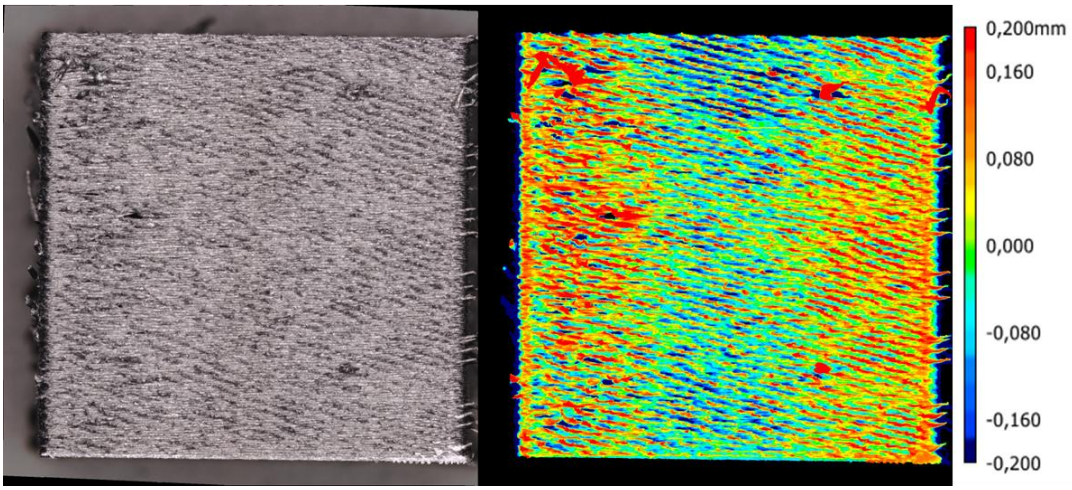

Figure 5-6: Side view and height map of a jagged line type

In the first publication [131], the shear rate was not yet considered, only the process parameters. Plotting the measured line roughness R_A of the walls along the layer lines in X over the shear rate, as in Figure 5-7, shows a weak trend of higher shear rate leading to higher average roughness. The line roughness along the extrusion direction is independent of the layer height.

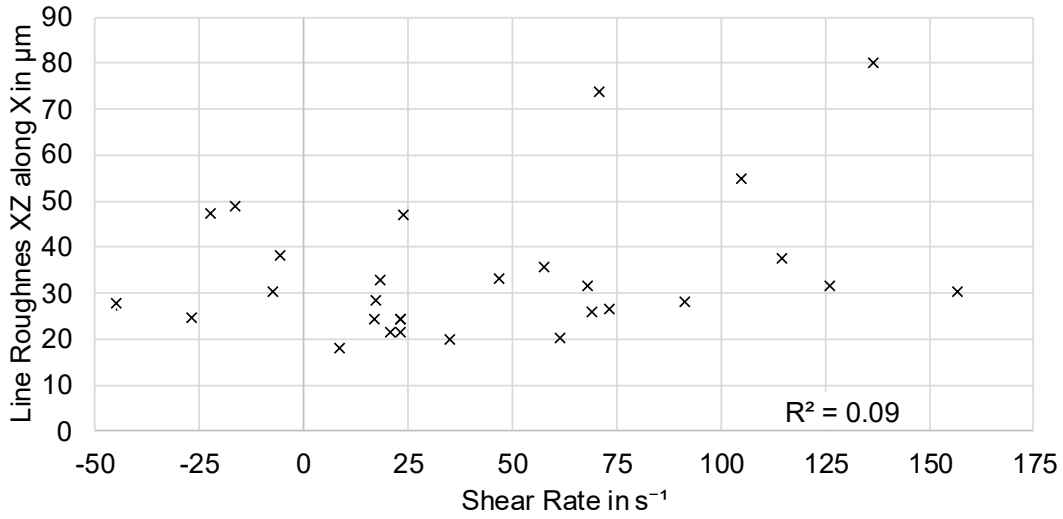

Figure 5-7: Line roughness of walls along X over shear rate

The surface roughness does not trend with the shear rate, as the artefact roughness overshadows the layer lines. However, clustering the results by layer height shows two different trends in Figure 5-8. The surface roughness decreases with increasing shear rates for low shear rates and high layer heights. The surface roughness increases with increasing shear rates for high shear rates and low layer heights. With an apparent optimum between trends right around the changeover point of convex to concave extrusion line shapes at ~23 s^{-1}.

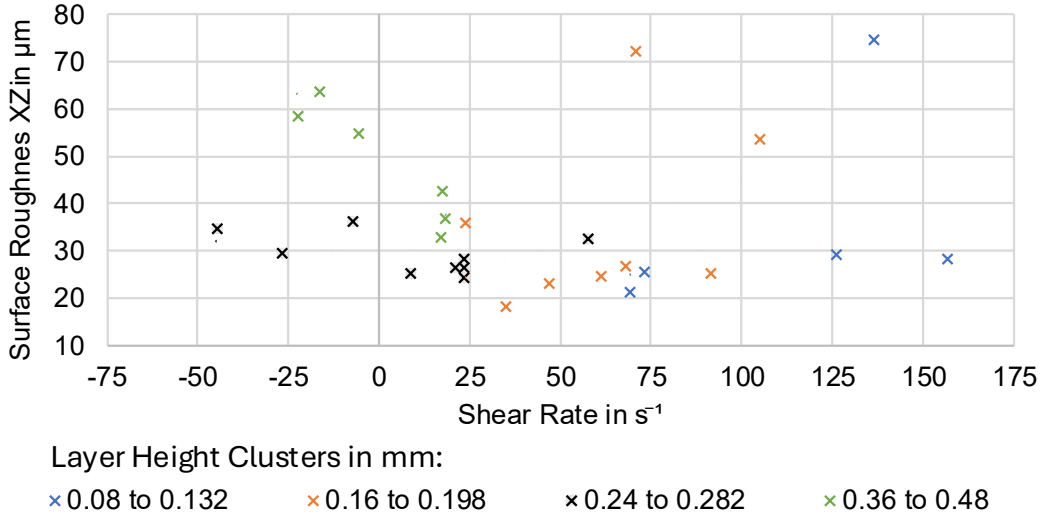

Figure 5-8: Surface roughness of walls over shear rate by layer height cluster

For the measurement of the fibre alignment, cross-section micrographs were made in the XY plane and the individual fibre orientations were measured from their orientation in the plane. All orientations were then plotted in histograms, and the standard deviation of the resulting normal distribution was used to quantify the fibre alignment of the group of fibres. A high value indicates poorly aligned fibres and a low value indicates high fibre alignment.

The 23 s-1 window for convex extrusion was assumed as a both-sided ideal state from -23 to +23 s^{-1}, even though the lower bound did not directly affect surface roughness or shape. However, the side walls of experiments with lower shear rates did show noise-like artefacts, similar to high shear rate samples. This can be seen in Figure 5-9 below for the two low shear rate experiments with -45 and – 27 s^{-1}, respectively:

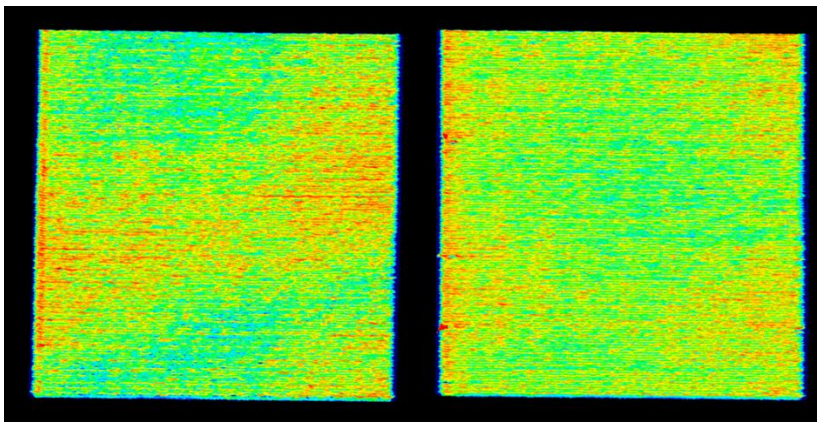

Figure 5-9: Side view of both experiments with a shear rate <-23 s^{-1}

Figure 5-10 shows two examples of the images and resulting fibre distributions of experiments having a shear rate of +17 s^{-1} and -16 s^{-1}, both having a convex shape and being within the ±23 s^{-1} window.

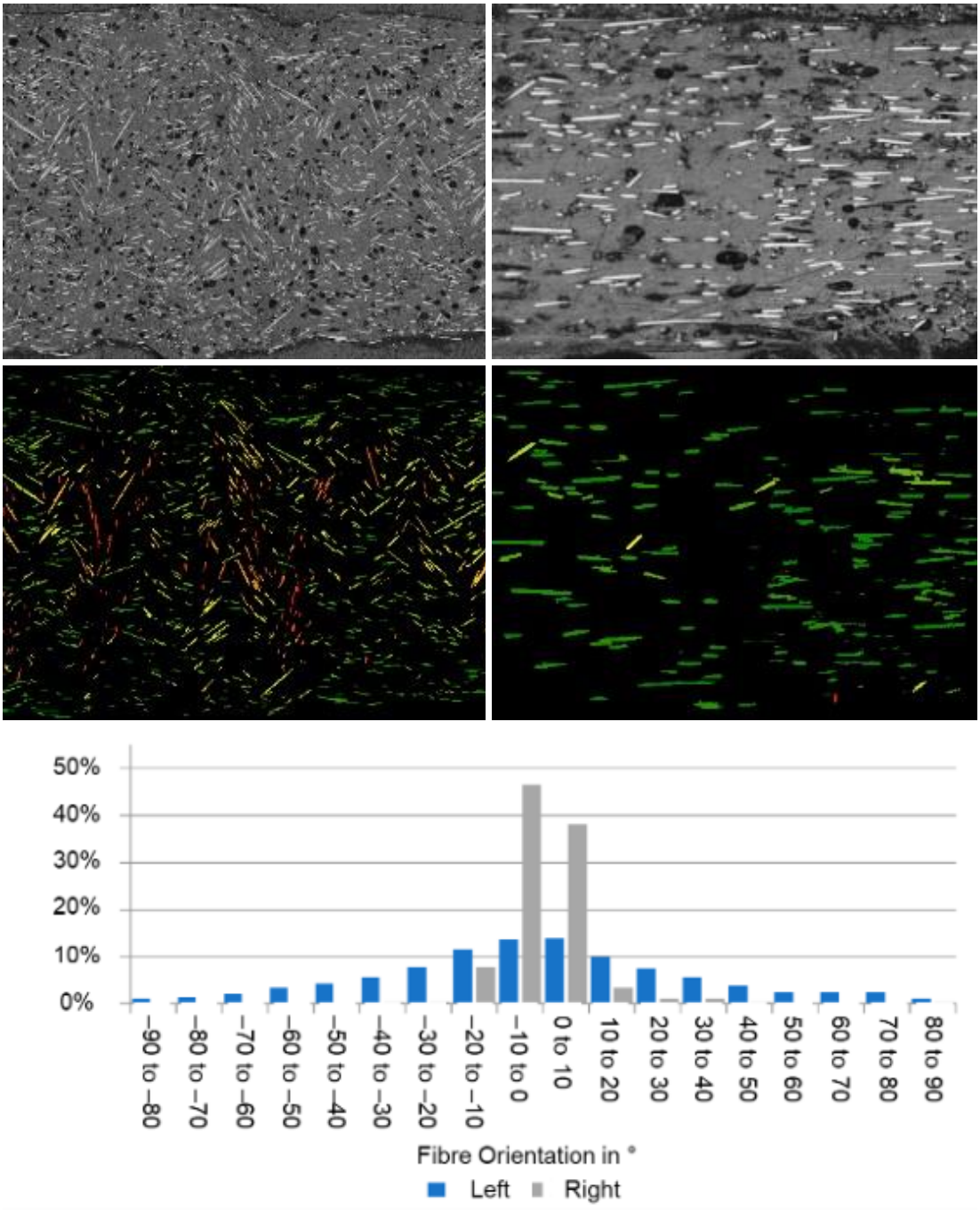

Figure 5-10: Examples of highly aligned and more random fibre aligned fibre distributions in micrographs and the resulting distribution

Extracting the fibre orientations of all experiments and plotting them over the shear rate, clustered by their extrusion shape, yielded Figure 5-11, showing again three different behaviours.

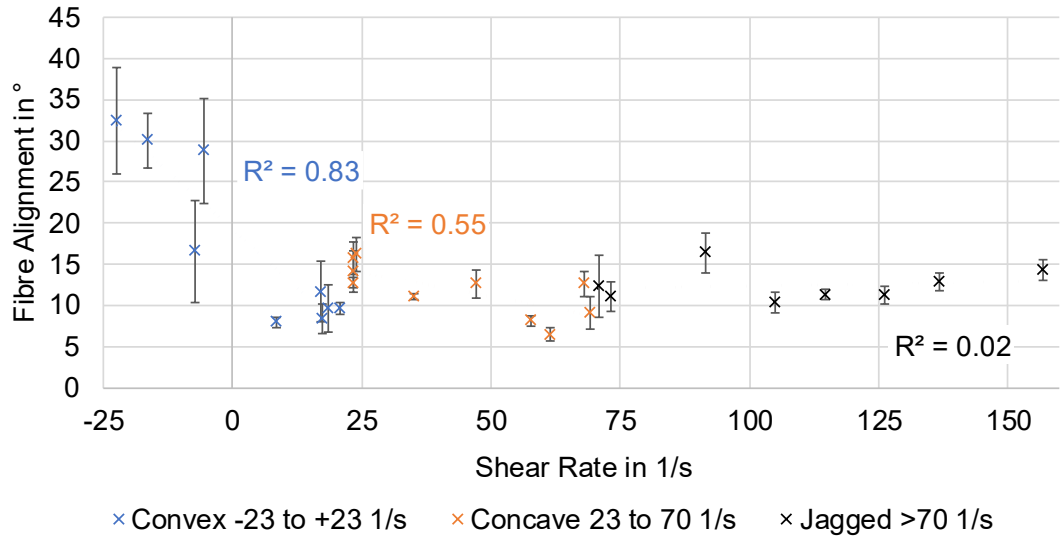

Figure 5-11: Fiber orientation over shear rate in extrusion-shape clusters

While the convex-shaped extrusion lines showed a high correlation with the shear rate, the convex ones showed only moderate correlation and an increased fibre misalignment at the 23 s^{-1} mark. The jagged extrusion lines showed no correlation with the shear rate at an almost constant level. The standard deviation increases noticeably for negative shear rates. This may be due to different fibre alignments inside the extrusion line over its height, leading to different results based on the cross-section position.

The absolute minimum of all measurements was 5.5°, only slightly above the filament at a shear rate of 61 s^{-1}; the minimum measurements of low positive shear rates ranged between 6.6 and 8.7 s^{-1}, also indicating excellent fibre alignment. The highest measured misalignment value was 39.6°, representing almost random distribution at a shear rate of -22 s^{-1} at the edge of the considered window.

The change in correlation and extrusion shape may indicate that while Jeffery's equation is valid at low shear rates, other effects come into play at high shear rates. This limit will likely depend on the material viscosity and the shear forces introduced by the passing nozzle and the material being sheared between the fixed layer below and the moving nozzle above. As the viscosity of thermoplastics decreases with increased melt temperature, a higher extrusion temperature may allow for higher shear rates. On the other hand, this may also affect fibre orientation, reducing the alignment at lower shear rates.

A setting at -16 and +17 s^{-1} was selected for mechanical testing, almost symmetrically inside the window and with an average length weighted fibre alignment of 30.1 and 8.2°, respectively. Both parameters' sets were printed with a 0.8 mm nozzle, eliminating influence factors from different internal shapes. These are the samples also previously shown in Figure 5-10.

The parameter sets are listed in Table 5-2:

Table 5-2: Parameter sets for tensile test specimens

	Width	Layer Height	Deposition Speed	Nozzle Diameter
Aligned	100% × D	60% × D	25 mm/s	0.8 mm
Random	200% × D	60% × D	18.3 mm/s	0.8 mm

The resulting stress-strain-curves are shown in Figure 5-12.

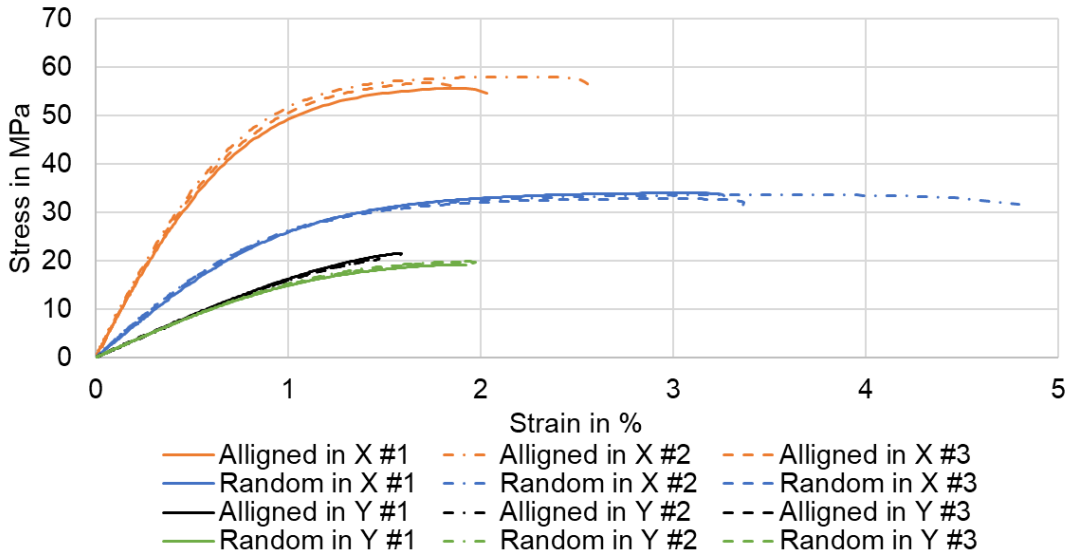

Figure 5-12: Stress-strain curves of the highly aligned (8.2°) and almost random (30.1°) parameter sets

The highly aligned specimens have significantly improved stiffness and strength along the extrusion direction compared to the almost random specimens, with the strength of the aligned specimens being 70% higher and stiffness 117% higher than the random specimens. Strain at break is significantly larger for the random specimens, with aligned specimens achieving, on average, only 57% of the average strain at break for randomly oriented specimens. The toughness along X of both samples interestingly was much closer together with 953.85 and 1051.29 J/mm³ for the highly aligned and random specimens, respectively, the aligned achieving about 93% of random specimens. The variance between specimens was very small, indicating that both process parameter sets were stable.

The effect in Y, however, shows almost no difference, with the random fibre orientation not contributing to stiffness or strength along Y and both values lower than their highly aligned counterparts.

Table 5-3: Results of tensile tests on FFF specimens

	Strain at Break in %	**Strength in MPa**	**Modulus in MPa**	**Toughness in J/mm³**
Aligned in X	2.17	56.80	7328.39	954.85
Random in X	3.81	33.47	3375.88	1051.29
Aligned in Y	1.51	20.74	1759.86	180.68
Random in Y	1.95	19.58	1750.65	253.66

The results are visualised with their standard deviations in Figure 5-13 below:

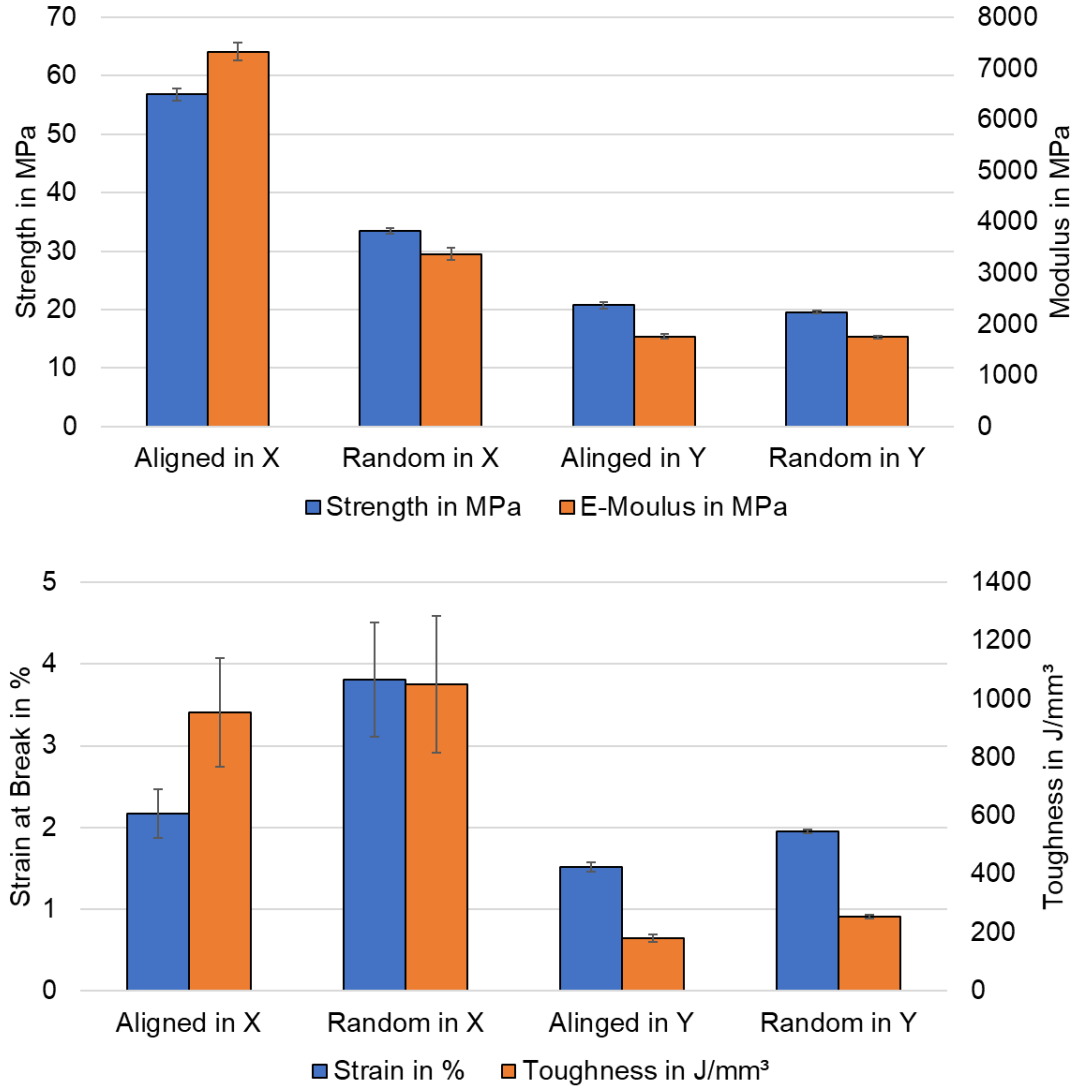

Figure 5-13: Results of tensile testing on FFF specimens

While DIC of the strain field showed homogeneous strain along X in Y it showed local strain patterns that are shown in Figure 5-14.

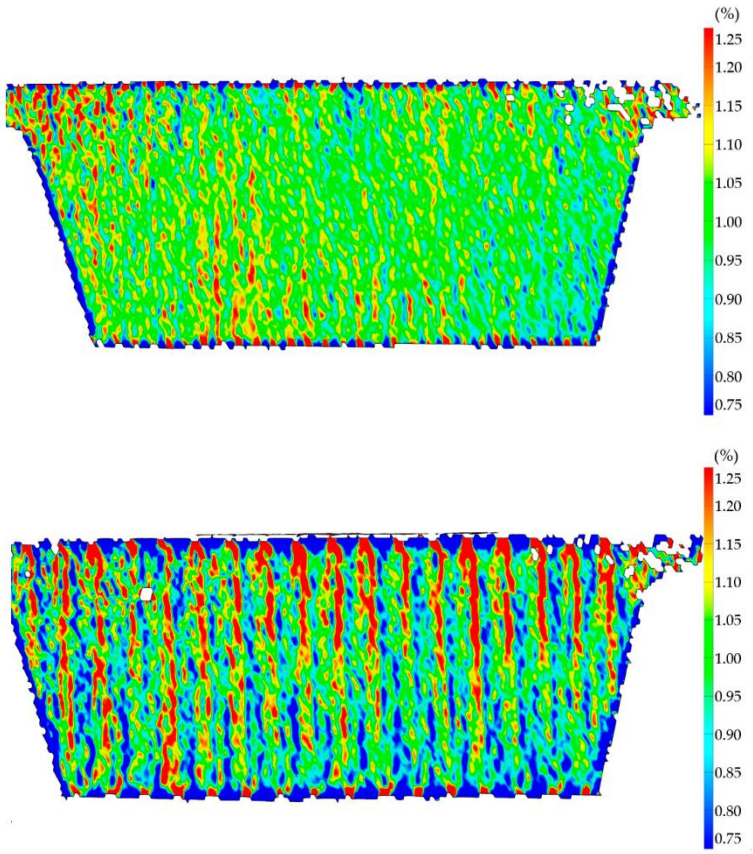

Figure 5-14: DIC of Strain fields of highly aligned (top) and random (bottom) specimens at 1% total strength

The strain fields both show local maxima and minima along the edges of the toolpath, but while the highly aligned specimen at the top is overall close to the average value of 1% strain, the lower specimen shows significantly more differences in local strain, with some of the maxima and minima reaching across the entire width almost uninterrupted. Figure 5-15 shows a sketch of the toolpath that aligns with the maxima and a close-up of the edge region, clearly showing the turnaround points of the toolpath and regions of lower strain between the extrusion lines.

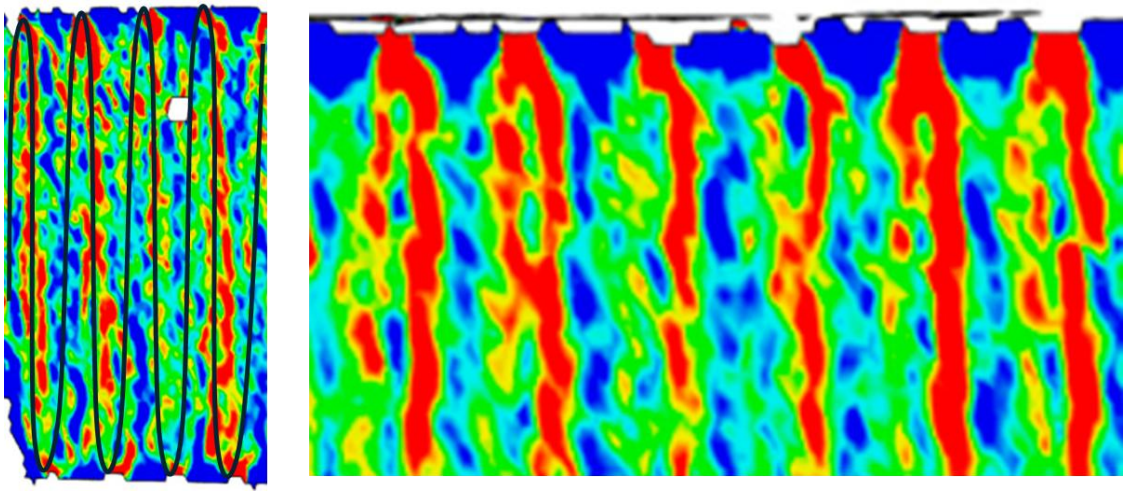

Figure 5-15: Sketch of toolpath and close-up of maxima on edge

In the highly aligned sample, this continuity of strain maxima is not visible. The maxima also align in parallel lines, but the occurrence is much more sparsely distributed and never continuous across the sample width. Also, turnaround points on the edge are not clearly visible. This may, however, be due to the strain difference being smaller.

Edge effects in the near-random specimens lead to higher fibre alignment at the edges of the extrusion line. This local difference in alignment appears to translate onto the strain field, with the aligned fibres restricting the matrix at the extrusion line edges and the near-random distribution in the core, allowing the matrix to stretch more freely.

Extrusion parameters clearly impact fibre orientation and, thereby, material properties significantly. The parameter sets selected for tensile testing differed only in extrusion line width and material flow velocity, tripling the misalignment. Thereby reducing the stiffness by more than half and strength by just over 40% but increasing strain at break by over 75%, slightly increasing the material toughness when tested along the extrusion direction X. Perpendicular to the extrusion lines within the layers along Y, the difference in fibre alignment had less impact on the mechanical properties on a macroscopic scale. However, the strain fields showed that the local elastic moduli were affected, and fibre misalignment led to a much more inhomogeneous strain field. Macroscopically a higher fibre misalignment reduces the anisotropy between X and Y, yet this is achieved by sacrificing strength and stiffness in X without improvement along Y.

5.1.2 Large Format Additive Manufacturing Experimental Results

As introduced in chapter 3.1.2, Fiber Alignment in Fluid Flow, and visualised in Figure 3-2, the typically larger nozzle diameters used in LFAM and lower deposition speeds result in much lower shear rates. The underlying process, however, is the same, and the same relationship observed for FFF is expected to apply. The chapter results were part

of a previous publication [132] and have undergone peer review, as mentioned in 4.2.1. A detailed table of all results can be found in the publication. The factor range for the LFAM experiments was as follows in Table 5-4 below, with deposition speed and shear rate not actively varied but resulting from the other factors, and nozzle diameter constant:

Table 5-4: Factor range of the LFAM experimental results on fibre alignment

Parameter	**Lower Limit**	**Upper Limit**
Line Width w	8 mm (100% D)	120 mm (150% D)
Layer Height h	2 mm (25% D)	4mm (50% D)
Extrusion Temperature T_{ex}	350°C	400°C
Layer Time t_L */ (Deposition Speed* v_d*)*	40 s (27 mm/s)	120 s (9 mm/s)
(Nozzle Diameter D)	8 mm	8 mm
(Resulting Shear Rate $\dot{\gamma}$*)*	0.25 s^{-1}	9.5 s^{-1}

The extrusion temperature was added as a factor to investigate the effect of reduced viscosity at higher temperatures on the fibre alignment. Instead of the deposition speed, the layer time was set, as the experiments also served to produce results for quasi-amorphous polymer bonding, which will be presented in 5.3. The shear rate resulting from the parameter sets was always larger than 0, as the previous results showed that, while diverging flow can cause near-random fibre orientation, it does not benefit the Y direction. The maximum shear rate was 9.5 s^{-1}, well below the range at which the extrusion line shape changes in FFF, though this range may be different for the used polymer, a 30% fibre-reinforced LM-PAEK, due to the higher viscosity.

Accurate assessment of the fibre orientation within the prints is crucial for understanding the resulting mechanical properties. Computed tomography is a proven precise method for determining the fibre orientation; however, to achieve a high resolution and identify the individual fibres, specimens must be small, and substantial amounts of data must be generated. This makes it impractical for the screening of sets with a high number of parameters and large specimens. For this reason, the previously described image analysis of cross-section micrographs was used. The core assumption is that fibres are mostly oriented in the XY plane, and cross-sections can be made parallel. While this was the case for fused filament fabrication printed specimens with low layer heights, it became evident that the approach is less effective for LFAM, as the significantly higher layer heights result in more out-of-plane fibre orientation. With regions within the extruded

line showing significantly different fibre alignment, highly aligned around the edges of the line and highly randomised in the core, the resulting distribution of the measurements is strongly affected by the cross-section position inside the line. This resulted in a very high variance in measurement results of repetitions on the same specimen and would only have been possible to remedy with a significant additional effort to ensure precise positioning of the cross-section, defeating the purpose of being able to analyse a large number of samples quickly.

Determining the fibre alignment through micrographs proved susceptible to measurement errors. Therefore, the results should be seen as indicative values and are only included for completeness. A trend to more aligned fibres with higher shear rates was noticeable and agrees with the determined fibre-dominated mechanical properties in X. For completeness. This trend is shown in Figure 5-16 over the shear rate.

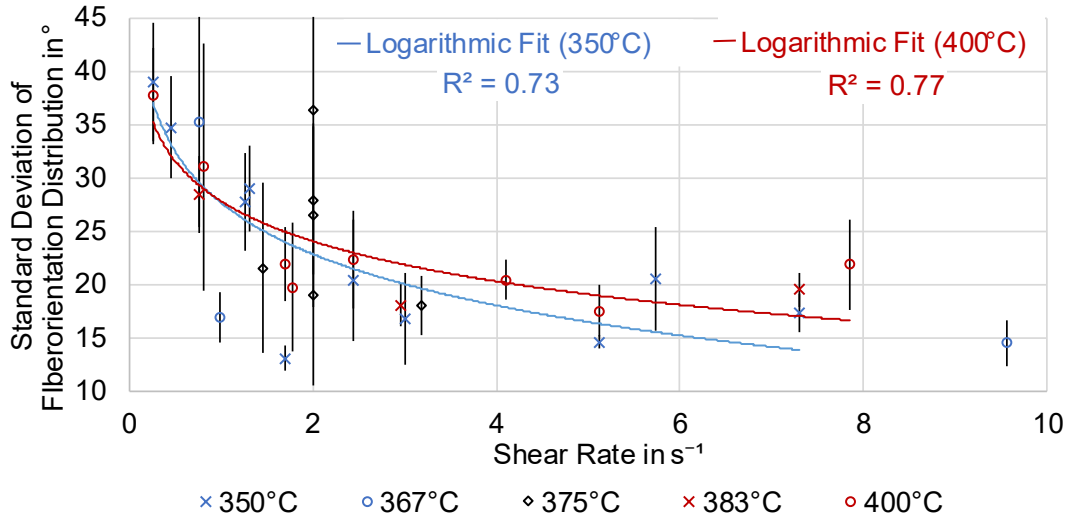

Figure 5-16: Fibre alignment over shear rate

Overall, the experiments agree with the expectation that a higher shear rate leads to lower fibre misalignment. However, because of the flawed measurement technique, no conclusion should be drawn due to the high variance of measurement results. Logarithmic trendlines have been added for the highest and lowest extrusion temperature experiments, respectively, 400 and 350 °C, which have a difference in viscosity. The trend for lower temperatures points towards better alignment at high temperatures, which is plausible, as the higher viscosity would lead to higher stress and larger aligned edge regions in the extrusion line.

As the measurement of fibre alignment was inaccurate and unreliable, the mechanical properties were not correlated to these measurements. Figure 5-17 and Figure 5-18 illustrate that a correlation between the shear rate and the mechanical properties exists, with high shear rates leading to high strength and stiffness. This is assumed to be due to a higher fibre alignment. Linear trendlines were added for the experiments at 350 and 400 °C again to indicate the effect of lower viscosity. The trendline for the cooler and,

thereby, more viscous material shows higher material strength and stiffness, possibly due to more fibres being aligned through thicker edge regions with high alignment or higher shear forces.

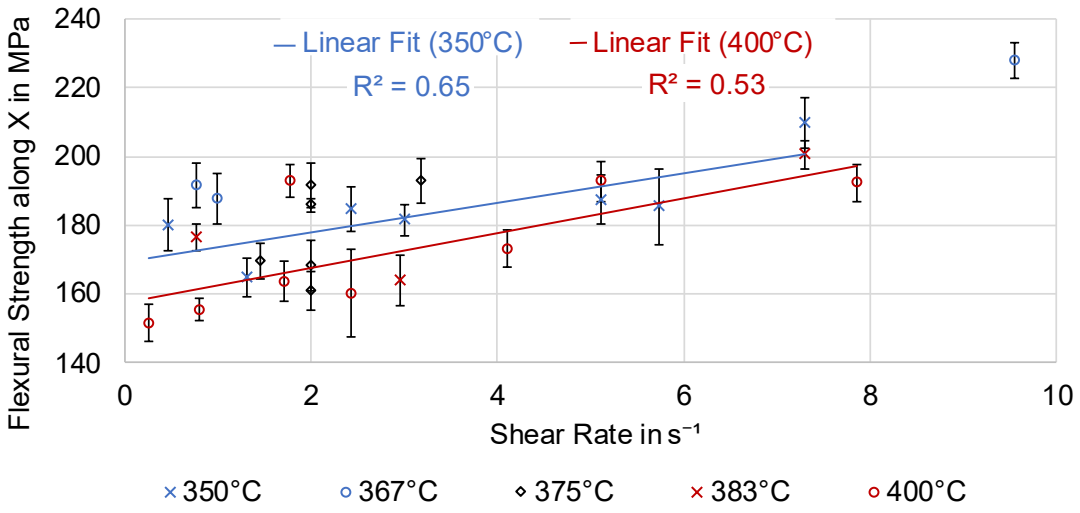

Figure 5-17: Flexural strength along X over shear rate in LFAM

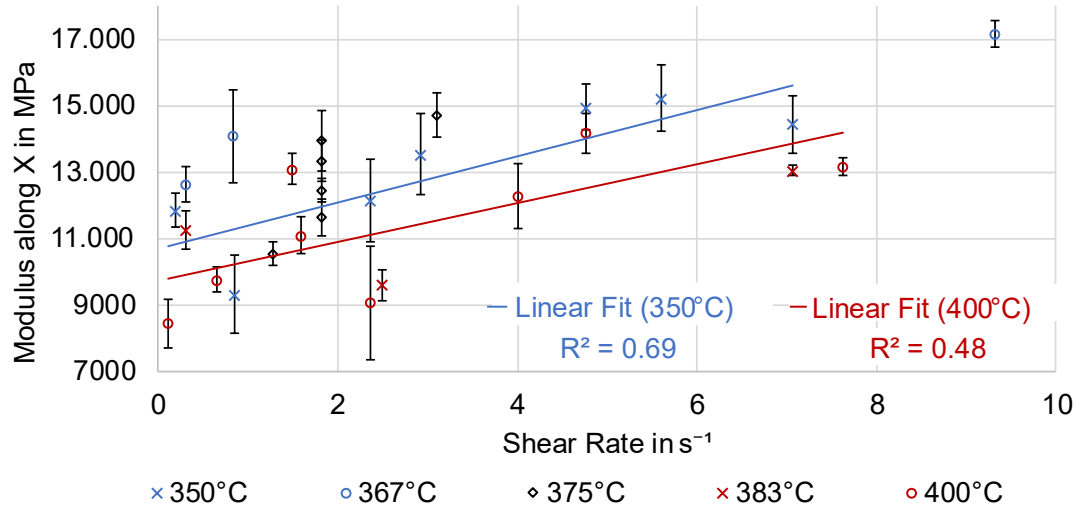

Figure 5-18: Modulus along X over shear rate in LFAM

High shear rate values were shown to improve the flexural strength and modulus, suggesting that it also helps align the fibres inside the extrusion lines. This trend fits well with the mean values of the observed fibre misalignment.

The results show a correlation between the shear rate and material properties along X in LFAM. Fibre misalignment was expected to strongly affect the material's mechanical properties, but it could not be accurately measured using only microscopy. However, high fibre misalignment leads to lower stiffness and strength along the extrusion lines. The highest achieved strength was 51% higher than the lowest, and modulus increased

by 103% and strain at break of the highly aligned specimens only 67% of the unaligned specimens. This shows a strong relationship between the material properties through different process conditions.

5.1.3 Conclusion for Hypothesis 1

The experimental results supported Hypothesis 1, demonstrating that fibre alignment during material extrusion (MEX) can be effectively predicted using Jeffery's equation, with shear rate as a key determinant of the final fibre orientation within the extrusion line. The findings confirmed that the type of flow, particularly diverging and converging flows, directly influences fibre distribution and alignment, thereby impacting the mechanical properties of the printed parts.

The investigation revealed distinct extrusion line shapes that corresponded to specific shear rate ranges in FFF, convex, concave, and jagged. Convex extrusion lines formed at shear rates below 23 s^{-1}, resulting in highly aligned fibres along the extrusion direction, with minimal misalignment. These samples exhibited superior mechanical performance along the extrusion direction, with tensile strength and modulus improvements of up to 70% and 117%, respectively, compared to samples with near-random fibre orientations. Conversely, shear rates exceeding 70 s^{-1} produced jagged extrusion lines, where the extrusion process became unstable.

The data also highlighted the potential for flow-induced misalignment at negative shear rates, confirming that converging flow conditions can lead to significant fibre reorientation perpendicular to the extrusion direction. This behaviour aligns with predictions based on Jeffery's equation, emphasising the sensitivity of fibre alignment to complex shear flow interactions. While convex-shaped extrusion lines showed consistent fibre orientation patterns, concave and jagged profiles demonstrated increased variability, suggesting additional influences such as extrusion instability and surface effects at higher shear rates.

The comparative analysis of different nozzle diameters, layer heights, and extrusion widths reinforced the conclusion that interdependent factors, including flow geometry and material rheology, govern fibre alignment. Introducing a high-fibre-content PETG composite facilitated clear visualisation of alignment changes, confirming that fibre misalignment within the extrusion line correlates strongly with mechanical anisotropy in printed parts. These findings suggest that achieving optimal shear rates and producing convex extrusion profiles can significantly improve mechanical properties while maintaining process stability.

In LFAM, the significantly lower shear rates inherent to larger nozzle diameters were associated with weaker fibre alignment trends. The experiments showed that raising extrusion temperatures to reduce viscosity may reduce shear forces and, thereby, fibre

alignment, though the effect is small over the possible range. This indicates that increasing the extrusion temperature may broaden the 23 s^{-1} process window for convex line shapes.

Despite challenges in precisely measuring fibre orientation through micrograph analysis at higher layer heights, the mechanical testing results substantiated the hypothesis, demonstrating a clear link between increased shear rate and improved flexural strength and modulus.

Overall, this study validates that fibre alignment can be controlled through careful modulation of extrusion parameters, particularly shear rate, as predicted by Jeffery's equation. The experimental results underscore the importance of maintaining controlled flow conditions to enhance the mechanical performance of MEX-printed components. These insights provide a foundation for optimising MEX process settings to produce mechanically robust parts with tailored fibre orientations, advancing the broader industrial application of fibre-reinforced thermoplastic composites in AM.

5.2 Mechanical Relaxation Time and Interlayer Bonding

The second hypothesis was that the mechanical relaxation time of polymers can be used as a reliable approximation for the welding time during interlayer bonding in MEX, with the sub-hypothesis that it can be approximated over temperatures below the melting point from measurements of the melt using the VFT relationship.

5.2.1 Experimental Results

The results of the chapter were part of a previous publication [133] and have undergone peer review, as mentioned in 4.3.2.. Experiments began by printing the specimens for mechanical testing and introducing the thermocouples in the printing process to capture the thermal history. In the case of LFAM, this resulted in a cube of which three remaining walls could be used for mechanical testing. For FFF, the single wall had to be reprinted to prevent the thermocouple from interfering with the test specimens. As a reminder to avoid confusion, the materials are identified by a prefix SC for slow crystallising, IC for intermediate crystallising and FC for fast crystallising, followed by the chemical structure, the fibre and fibre content, e.g. SC-PAEK-CF20 is a slow crystallising PAEK with 20% carbon fibre content.

5.2.1.1 Thermal History

The thermocouple measurements are shown in Figure 5-19. Time is normalised to begin at the first temperature peak the sensor registers when the nozzle passes over for the first time. In later chapters, the thermal history of the large-scale printer specimens will be approximated using the green line labelled 'DSC Curve'.

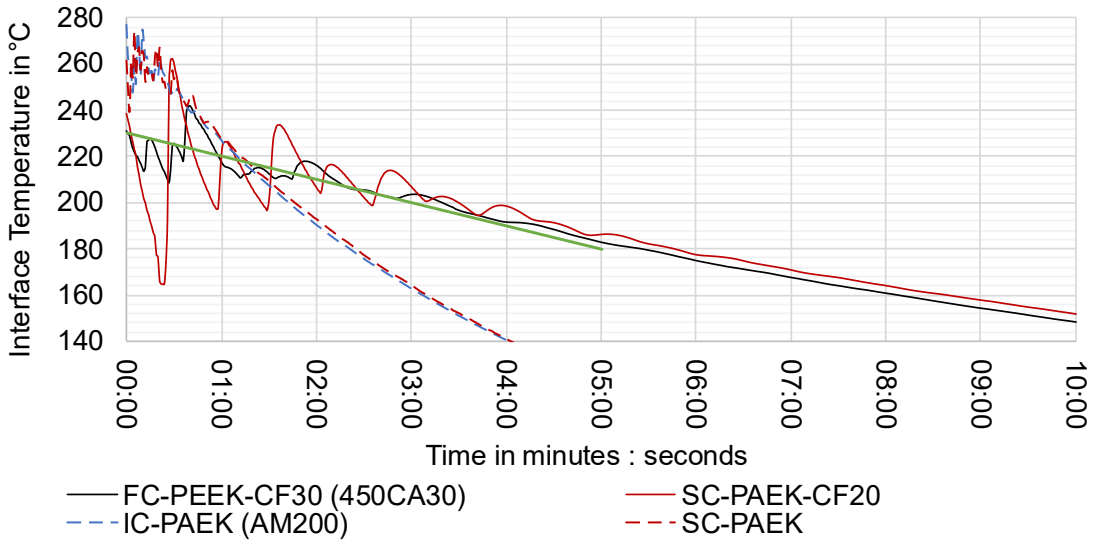

Figure 5-19: Interface temperature from thermocouple measurements

FFF measurements are shown in dashed lines, and LFAM measurements are in continuous lines.

The large-scale printer samples SC-PAEK-CF20 and FC-PEEK-CF30 (450CA30) cool down much more slowly than the filament-based printer samples SC-PAEK and IC-PAEK AM200, shown with dotted lines. This gives the large-scale printer samples up to 10 min above the glass transition temperature, almost three times as long as the filament-based printer samples. The cooling rate from the highest temperature at deposition to glass transition is, on average, 10 K min^{-1} for the large-scale and 35 K min^{-1} for the filament-based specimens, yet the initial cooling rates between the dips and peaks are much higher at around 100 K min^{-1}.

The initial peak temperature is lower for the large-scale samples than for the FFF samples. This is due to the shorter layer times of just about 10 s compared to the 60 s layer time for the larger specimens. For the large-scale printer specimens, most of the time is spent at temperatures lower than 230 °C, where the crystallisation of the polymer should slow down again. The filament-based specimens remain between 280 and 230 °C for the first minute.

The slower crystallising polymers cool down more slowly than their faster crystallising counterparts; while barely visible for both the slower crystallising filament-based specimens SC-PAEK and IC-PAEK, the difference is more significant for the large-scale samples between the fast-crystallising injection moulding grade FC-PEEK-CF20 and AM grade SC-PAEK-CF20. This is clearly visible in the large-scale printer specimens after 5 min. However, shortly after the glass transition, the temperatures equalise. This is probably due to crystallisation happening during the entire cool-down, releasing heat in the AM polymer, whereas the injection moulding grade releases its crystallisation enthalpy already at higher temperatures where the increased temperature gradient to the environment leads to faster dissipation. This could also explain why the AM polymer

has much more pronounced peaks and dips to lower temperatures. The large-scale curves also show a difference just after deposition: while the slow-crystallising material has a deep dip in temperature before rising again at 30 s when the nozzle passes the thermocouple for the second wall of the layer, the fast-crystallising material shows a sharp peak between the two, at about 15 s, possibly caused by crystallisation releasing heat.

These curves will be used to further interpret bonding and crystallisation. The thermocouple readings are used for the lower, cooler layer as one of the bonding partners. Essentially the bonding process begins when the consecutive layer is deposited on top. Thermal imaging showed a slightly lower surface temperature in the filament-based specimens and cooler edges of the print. The edge regions were consequently discarded during mechanical testing.

5.2.1.2 DSC

The next step was to measure the crystallisation behaviour of the used materials under constant cooling conditions. Figure 4-3 already showed the DSC curves and Table 4-4 the summarised characteristic temperatures of the feedstock materials.

By using DSC also on the printed specimens before annealing, the differences in crystallinity formed in 3D printing compared to the measurements are found; they are summarised in Table 5-5. The enthalpies of the fibre-reinforced materials have been corrected to the polymer content. While the injection moulding material FC-PEEK-CF30 is nearly unaffected by the increased cooling rates, the AM materials show clear changes in crystallinity content. $H_{Specimen}$ is the melting enthalpy of specimens after printing, $H_{10\ K\ min-1}$ the melting enthalpy after being cooled at 10 K/min, T_m the melting temperature and T_c the crystallisation temperature.

Table 5-5: DSC results of printed specimens

Material	**T_g in °C**	**T_m in °C (for each melting peak if multiple)**	**T_c in °C**	**$H_{Specimen}$ in J g^{-1} (crystallinity in %)**	**$H_{10\ K\ min-1}$ in J g^{-1} (crystallinity in %)**
SC-PAEK	154.21	293.03 311.24 327.21	233.337	16.44 (13%)	23.43 (18%)
IC-PAEK (AM200)	152.34	304.75	253.64	32.3 (25%)	40.14 (31%)
SC-PAEK-20CF	153.16	290.73 312.99	233.10	26.76 (21%)	23.13 (18%)

		328.19			
Reference LFAM FC-PEEK-30CF 450CA30	145.86	339.9	292.15	41.63 (32%)	42.74 (33%)

The materials designed for AM show lower melting and crystallisation temperatures and higher glass transition temperatures. The SC-PAEK further shows a lower overall crystallinity than the IC-PAEK and FC-PEEK-CF30 after controlled cooling at 10 K min^{-1}. The FC-PEEK-CF30 is the only material with nearly the same crystallinity after printing compared to that after controlled cooling. In contrast, the SC-PAEK-CF20 shows a slightly higher crystallinity after printing than after controlled cooling. The SC-PAEK used in small-scale printing shows a very low crystallinity after printing, which is visible in the parts as a darker, more transparent colour, indicating amorphous material. It is the only material which shows a cold crystallisation peak in the first heating after printing during DSC measurement.

Additionally, the large-scale printed samples were then subjected to a DSC run that emulates the temperature curve measured by the thermocouple in large-scale printing from Figure 5-19. The DSC program would heat the sample to 405 °C, hold it for 5 min and then rapidly cool it to 230 °C using PerkinElmer's 'ballistic cooling' function of the DSC, which applies the maximum available cooling rate (the effective sample cooling rate measured was about 375 K min^{-1}) from 230°C onward it would do a temperature scan at 10 K min^{-1} to 100 °C, the average cooling rate after deposition. This would give an indication of whether the material begins to crystallise before the next layer can be placed on top and if the material bonding can be considered amorphous during fusion bonding, as the thermal history showed that the material remains below the melting temperature once deposited.

The resulting curves show that while the 450CA30 begins to crystallise already during the ballistic cooling, the slow crystallising material had its crystallisation onset after 122.5 s with a standard deviation of only 1.26 s and peaked at 237.5 s with a standard deviation of 3.24 s, tested on three specimens. This shows that the crystallisation onset is very repeatable.

Because of the onset of crystallisation of the FC-PEEK-CF30, it was assumed that it would not fuse its layers due to already having crystallised and any interlaminar strength developed is purely adhesive or due to micromechanical interlocking of the rough layer surfaces. The calculated degree of healing would always be 0 as the threshold is reached before the next layer is deposited.

The SC-PAEK-CF20 is considered amorphous for the first 122.5 s and then considered crystalline, ending the bonding process.

The small-scale materials were not checked by DSC due to the very short layer time and higher temperature, resulting in less supercooling and ensuring the next layer could be deposited before crystallisation occurred. Also, crystallisation was visible during printing several layers below the printed layer by changing the colour of the unfilled polymer.

5.2.1.3 Mechanical Relaxation Time

To estimate the developed bond strength from the thermal history, the relaxation time of the polymers needed to be determined. As mentioned above, this was done by melt rheology at temperatures above or just below the melting point, as crystallisation would otherwise occur. The curve fit function of Pythons SciPy library was used to determine the A and B coefficients of the Vogel–Fulcher law; T_0 was chosen as the onset of the glass transition during heating. The parameters are shown in Table 5-6.

Table 5-6: VFT equation fitting parameters

Material	*A*	*B*	T_0
AM200	0.01383748	4.52652234	145.8
SC-PAEK	0.00787024	3.90514159	152.46

The resulting equation was then evaluated over the temperature range. Figure 5-20 shows the data points and resulting fitted curves on two scales to show both the fitting of the points and the curve extrapolation to lower temperatures.

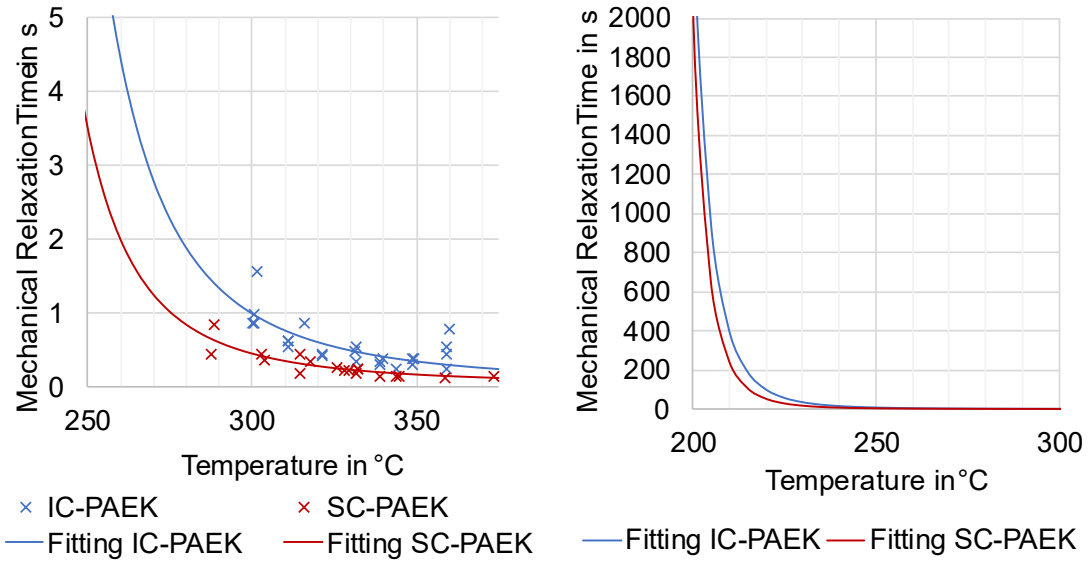

Figure 5-20: Data points for relaxation times from rheological experiments and the resulting fitted VFT curves left, detailed on the fitted points; right, extrapolation over the bondable temperature range.

Figure 5-21 shows the fitted curves over the process relevant range from T_g to 300°C. Showing that the healing during the LFAM process occurs in a temperature range where the welding process takes several minutes, whereas the FFF specimens should complete healing within seconds or even fractions of a second. Below 200°C the welding is completed in hours and after 190°C the timescale becomes days. This illustrates how critical the lower top layer temperature is to layer bonding, even if crystallisation can be supressed.

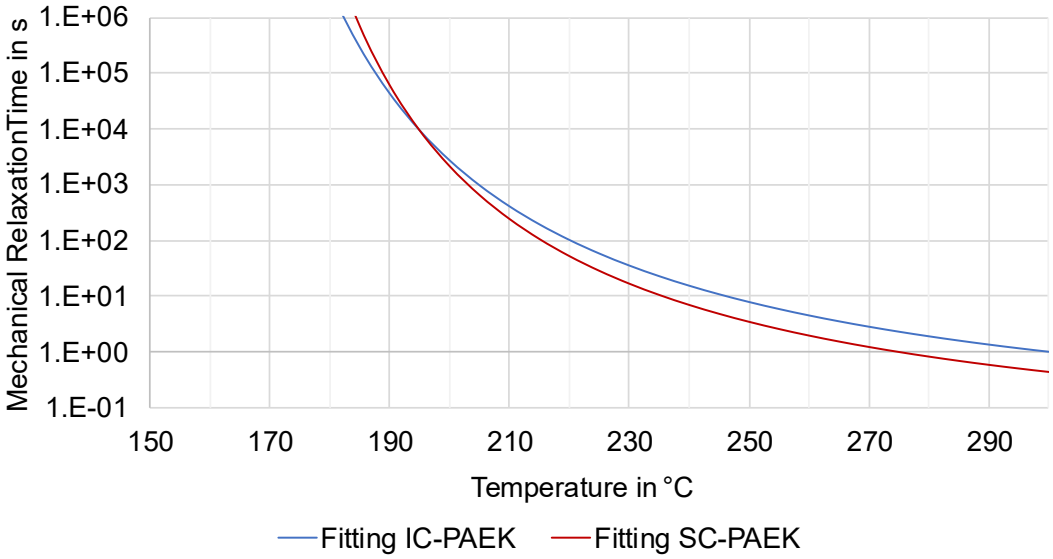

Figure 5-21: Fitted VFT curves on a logarithmic scale over the process-relevant temperature range

Even though the IC-PAEK has a lower glass transition temperature, the relaxation times are longer at high temperatures giving the slower crystallising material a more favourable curve in the temperature range above 200 °C, below which the relaxation times exceed the relevant time scales. As these results were gathered before moving to large-scale testing and the slow crystallising SC-PAEK showed both a more favourable welding time curve and slower crystallisation onset, the polymer was selected as the base for the large-scale compound SC-PAEK-CF20 with carbon fibres. Up to this point, a very small amount was sufficient for the material characterisation, while large-scale printing requires significantly larger amounts even to fill the extruder.

5.2.1.4 Interlayer Healing Model

The degree of healing can be evaluated from the thermal history and fitted relaxation times, using equations 3-24, repeated below, by integrating the increase in bonding numerically and integrating overall measurements.

$$D_h(t) = \sum_0^{N-1}\left[\left(\frac{t_{i+1}}{A\times\exp\left(\frac{B\times T_0}{T(t_{i+1})-T_0}\right)}\right)^{1/4} - \left(\frac{t_i}{A\times\exp\left(\frac{B\times T_0}{T(t_i)-T_0}\right)}\right)^{1/4}\right] \qquad (3\text{-}24)$$

Thermal history was used from the second layer onward, as the thermal influence for the first layer on the thermocouple from the nozzle passing for the next extrusion line in the same layer caused the temperature to peak and the degree of bonding to jump to 100%. For the next layer, the direct nozzle influence was lower.

The crystallisation was used as a stopping criterion, ending the bonding process of the slow crystallising SC-PAEK after 122.5 s, starting from the initial material deposition of the layer below. Figure 5-22 begins with $t = 0$ when the next layer is deposited on top, the crystallisation onset is accordingly offset by the 60 s layer completion time to 62.5 s.

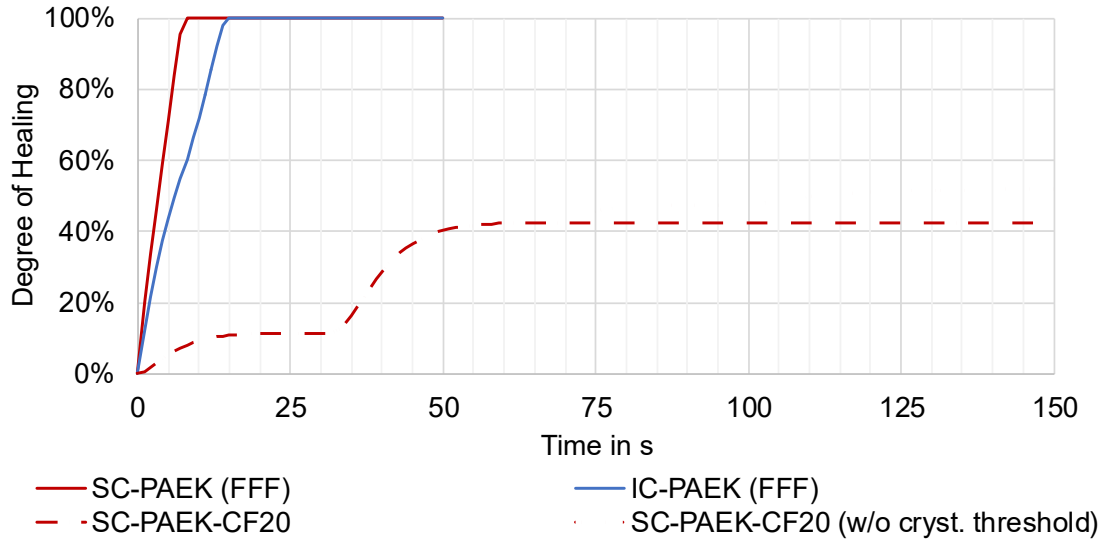

Figure 5-22: Evolution of degree of healing from the thermal history and relaxation times

The degree of bonding development without the crystallisation onset as a stopping threshold was also calculated for completeness.

From the graphs in Figure 5-22 the following observations are made.

The slow crystallising PAEK in small-scale AM completely fuses the layers together, achieving a 100% degree of bonding within one layer completion time of 10 s, in about 7 s.

The intermediately fast and slower bonding IC-PAEK AM200 rises to about 50% degree of healing in the first layer with bonding speed decreasing, but the heat from the nozzle depositing the consecutive layer on top boosts the healing process, which then quickly rises to 100% as well with the additional heat after 15 s, taking twice as long.

The large-scale samples are also influenced strongly by the heat of the nozzle, which passes every 30 s as a layer consisted of two walls with the degree of healing increasing steps of 30 s. These steps correlate with the peaks in the thermal history of Figure 5-19 where the temperature briefly passes over the relaxation time curve.

After 122.5 s crystallisation ends the bonding processes at 42.54% degree of bonding. It is also noteworthy that the second step, caused by the material deposited a layer above the bonding interface, is larger than the initial step. This is probably due to a fast heat loss by convection initially and then insulation by the consecutive layer. If crystallisation is neglected, the degree of bonding will rise to 52.32%; if considered only after the crystallisation peak, the degree of bonding will rise to 52.18%.

5.2.1.5 Mechanical Testing

Mechanical testing by three-point bending was chosen to evaluate the degree of bonding. Additional to the previous AM polymers unreinforced 450G samples were printed. These were meant to confirm that the early onset of crystallisation could not be compensated for with shorter layer times or higher temperatures.

The results are shown with their standard deviations in Figure 5-23. Five specimens were tested for each, except for the large-scale 450CA30 samples, where only three specimens were tested because layer bonding was so low that delamination occurred in several specimens during sample preparation. This already correlated well with the previously made assumption that layers are not welded together but rather held together by adhesion or surface roughness.

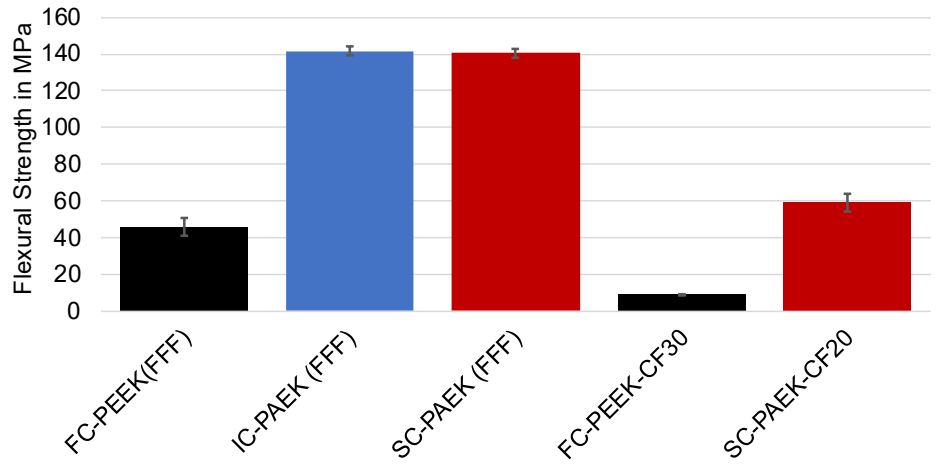

Figure 5-23: Flexural strength in Z of all printed specimens

An increase of 300% in layer strength is observable for the small-scale printer specimens for the AM polymers compared to the 450G reference. The Z strength is as high as the tested in-plane strength, achieving the expected 100% bonding strength. A 650% increase compared to the 450CA30 reference is observable for the large-scale samples, where the strength is lower than in the small-scale printer specimens. The 450CA30 failed adhesively between the layers, as was to be expected due to the onset of crystallisation before the next layer could be deposited. As fibre alignment is mostly in the extrusion direction, or at least in the layer plane, nearly the same maximum strength for the *Z* direction can be achieved in FFF with the slow crystallising material. This results in a 42.07% relative maximum strength based on the averages and 44.76% based only

on the maximum values, which is very close to the previously calculated 42.54%. degree of healing. The slow-crystallising material achieved higher strength on the LFAM machine than the fast-crystallising injection moulding material 450G on a small scale, even though the temperatures were much more unfavourable.

The added carbon fibre in the compounds should have very little effect in this orientation as the tested direction is perpendicular to the layer plane. Carbon fibres were added to the compounds not to improve the mechanical properties between the layers but rather to constrain thermal expansion and warping during the cool-down of the LFAM specimens. For the FFF specimens, this was not necessary as the samples were smaller.

Due to the welding times increasing rapidly at lower temperatures, as seen in Figure 5-21, the FFF samples of IC-PAEK and SC-PAEK benefit much more from the higher temperatures, even though they are subjected to higher cooling rates than the LFAM samples. Even without the healing stopped by crystallisation, assuming fully amorphous behaviours, and with the relatively slow cooling rate of only 10 k/min, the LFAM specimens would not achieve their full strength as the low temperatures shift the welding times to exponentially larger time scales.

5.2.2 Conclusion for Hypothesis 2

The second hypothesis stated that the mechanical relaxation time of polymers could serve as a reliable approximation for the welding time during interlayer bonding in MEX, with the sub-hypothesis asserting that this relaxation time could be derived from rheological measurements and approximated over temperatures below the melting point using the VFT relationship. The objective was to assess whether this approach could accurately predict the degree of healing across bonded layers, thereby improving the understanding of interlayer fusion dynamics, particularly for polymers with differing crystallisation kinetics.

The experimental findings support the hypothesis, demonstrating that the relaxation time obtained from rheological data is an effective parameter for approximating the molecular interdiffusion time necessary for achieving optimal bonding. The results confirmed that the relaxation time is highly temperature-dependent and follows the expected VFT behaviour, with the fitted parameters showing strong agreement with measured data. Notably, the derived relaxation times effectively captured the differences in bonding performance observed during FFF printing with SC- and IC-PAEK.

The thermal histories recorded during printing revealed distinct cooling behaviours for slow-, intermediate-, and fast-crystallising polymers. The relaxation times derived from the rheological measurements correlated well with the observed degrees of healing, particularly for the slow-crystallising PAEK. This material exhibited lower relaxation times at lower temperatures and delayed crystallisation, allowing for greater healing before crystallisation onset.

For the slow-crystallising SC-PAEK-CF20, the thermal analysis showed that the onset of crystallisation occurred after 122.5 seconds, providing a sufficiently long window for the interlayer fusion process to reach a significant degree of bonding. As a result, SC-PAEK-CF20 achieved a degree of healing of approximately 42.54% before crystallisation halted further diffusion, closely aligning with the predicted values.

The flexural strength tests validated the modelled bonding predictions. For the large-scale SC-PAEK-CF20 specimens, the measured Z-direction strength reflected the calculated degree of healing, confirming that the VFT-based relaxation time approximation accurately predicts mechanical performance. Conversely, the fast-crystallising FC-PEEK-CF30 exhibited negligible interlayer strength, as expected due to its rapid crystallisation kinetics, which prevented molecular interdiffusion.

The extrapolated VFT curves showed that below 200°C, the relaxation times increased exponentially, requiring impractically long durations for complete healing. This emphasises the critical importance of maintaining sufficiently high interlayer temperatures during MEX to ensure that the relaxation times remain within feasible bonding timeframes.

The results also highlighted the limitations of using conventional isothermal welding assumptions for MEX processes, where non-isothermal conditions dominate due to the rapid cooling and temperature gradients inherent in layer-by-layer deposition. By integrating the thermal profiles with the VFT-derived relaxation times, this study demonstrated that accurate interlayer bonding modelling requires precise thermal monitoring and an understanding of material-specific crystallisation behaviour.

Overall, the findings confirm that the mechanical relaxation time derived from rheological measurements and modelled using the VFT relationship provides a robust approximation for welding time during interlayer bonding. The hypothesis is validated, with the sub-hypothesis substantiated by both empirical data and theoretical modelling. The ability to predict interlayer bonding based on relaxation time offers significant potential for optimising MEX process settings, particularly for high-performance polymers with tailored crystallisation kinetics.

5.3 Fusion Bonding of Pseudo-Amorphous Polymers at Low Temperatures

The third hypothesis was that pseudo-amorphous polymers can achieve interlayer bonding at temperatures below the melting point if cooling rates are high enough to delay crystallisation, with the sub-hypothesis that the threshold for bonding is determined by the onset of crystallisation.

5.3.1 Experimental Results

The results of the chapter were part of a previous publication [132] and have undergone peer review as mentioned in 4.3.3. A detailed table of all results can be found in the publication.

In the experiments, cubes were printed on the LFAM machine, and the thermal history was recorded during processing to be able to link the material properties back to the process conditions. Parameters were as described in 5.1.2.

5.3.1.1 Thermal History and Crystallisation

Thermal history was measured as before with an embedded thermocouple and with an IR camera. Particularly the temperature to which the previous layer had cooled when the next layer was deposited was of interest.

The direct extrusion parameters showed no correlation, only a very weak correlation, and high variance between the resulting layer temperatures during processing. Only the layer time was found to have a strong negative correlation with the substrate temperature. A longer layer time leads to lower temperatures as the material has more time to cool. However, the substrate temperature varied by almost 100 °C for identical layer times, depending on the combination with the other parameters of extrusion height, extrusion width, and extrusion temperature, as can be seen in Figure 5-24.

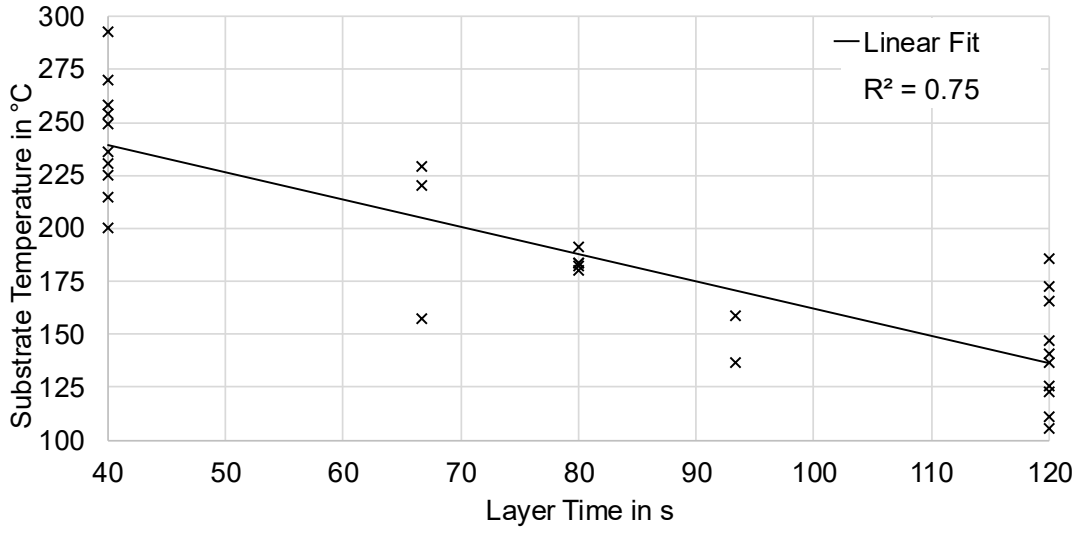

Figure 5-24: Correlation of substrate temperature over layer time.

The enthalpy deposition rate, introduced in equation 4-3 and repeated below, showed much higher correlation with the resulting layer temperature just before deposition of the next layer, as can be seen in Figure 5-25.

$$\dot{H} = \rho \times c_p \times (\pi \times ({}^{h}/_{2})^2 + h \times (w - h)) \times v_d \times (T_{Ex} - T_{\infty}) \qquad (4\text{-}3)$$

A comparison of temperature measurements during printing by thermography and introduced thermocouples is included in the same figure. The thermocouple readings show slightly higher temperature than the thermography since they measure the inside of the deposition rather than the free surface. The difference between readings is demonstrated by the one-side error bars in Figure 5-25. This difference is most prominent in the range between about 180 and 260 °C, which is close to the crystallisation window of the material of about 180 to 245 °C.

While the difference indicates that the temperature gradient within a single layer is small, mostly less than 10 °C, outside of the crystallisation window, it can reach up to 35 °C when the layer is completed just as the crystallisation reaches its peak.

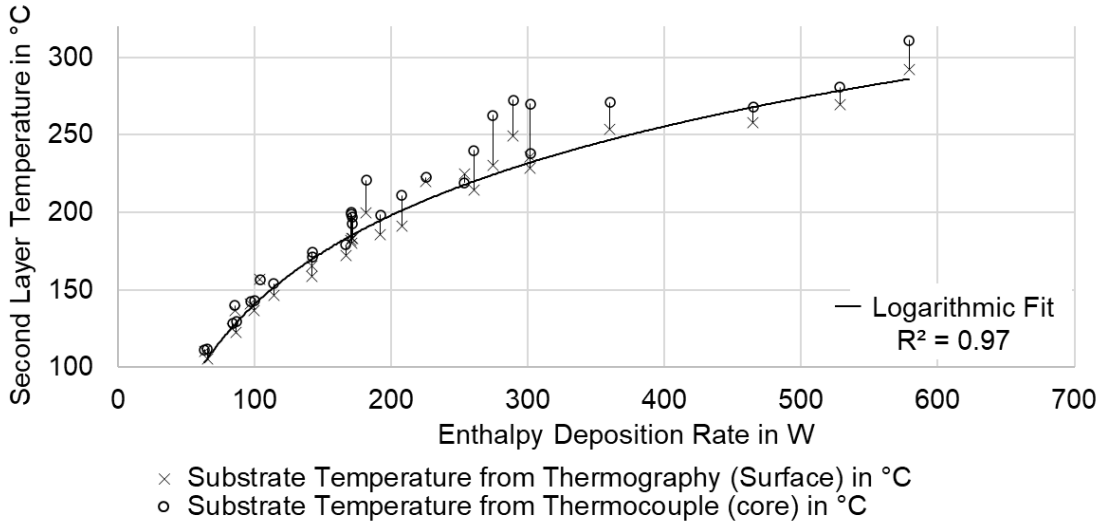

Figure 5-25: Measured substrate temperature by thermography and overprinted thermocouple

Substrate surface temperature correlates with the enthalpy deposition rate, and experiments with very different process parameters achieve similar layer temperature if the aggregate is similar, as can be seen in the pairwise examples of Table 5-7.

Table 5-7: Pairwise comparison of experiments with similar deposition powers but different extrusion parameters.

Number in Figure 5-26	Extrusion Temperature in °C	Extrusion Width in mm	Layer Height in mm	Layer Time in s	Enthalpy Deposition Rate in W	Surface Temperature in °C
1	350	8	4	93	142.1	170.3
2	400	9	4	120	141.9	172
3	400	12	2	40	301.6	257.7
4	350	12	4	67	301.8	236.9

Figure 5-26 shows the side IR image of the prints. It shows that for the observed temperature, not just the last layer is similar, but the temperature distribution in the material below.

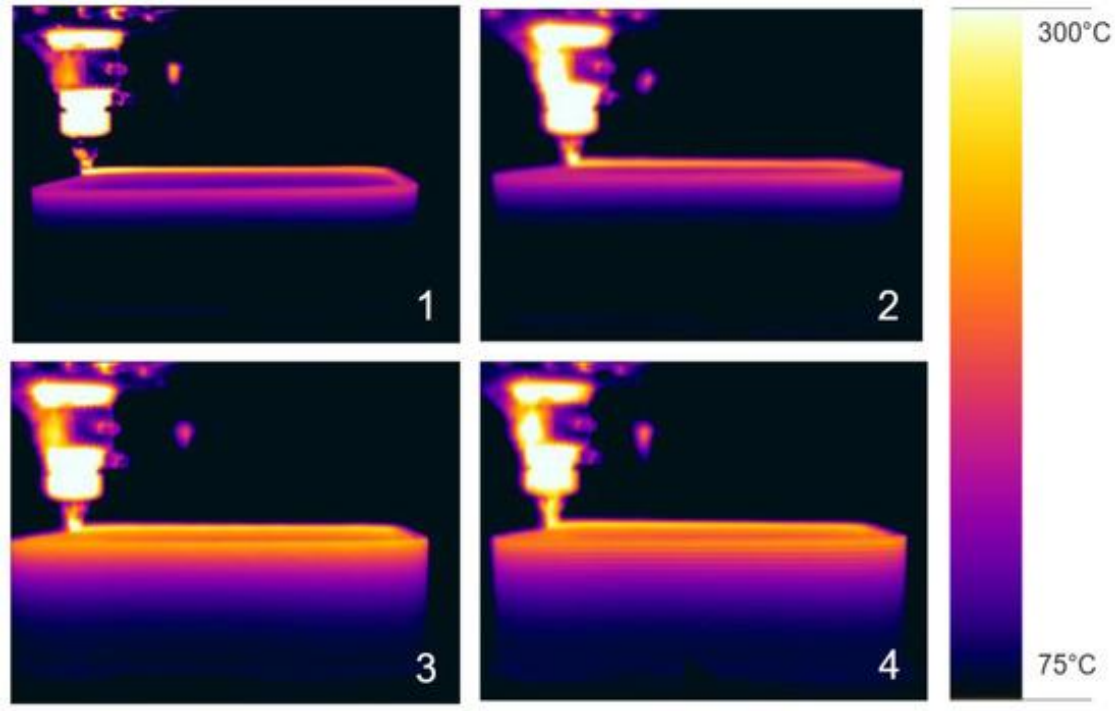

Figure 5-26: IR images of examples of Table 1, numbers 1–4 indicating the corresponding row of Table 3

This is independent of the extrusion height, width, and temperature if the enthalpy deposition rate is similar. A higher enthalpy deposition rate leads to a higher substrate temperature at contact with the deposition but also shifts the thermal profile along Z to a higher level, as can be seen in Figure 5-27.

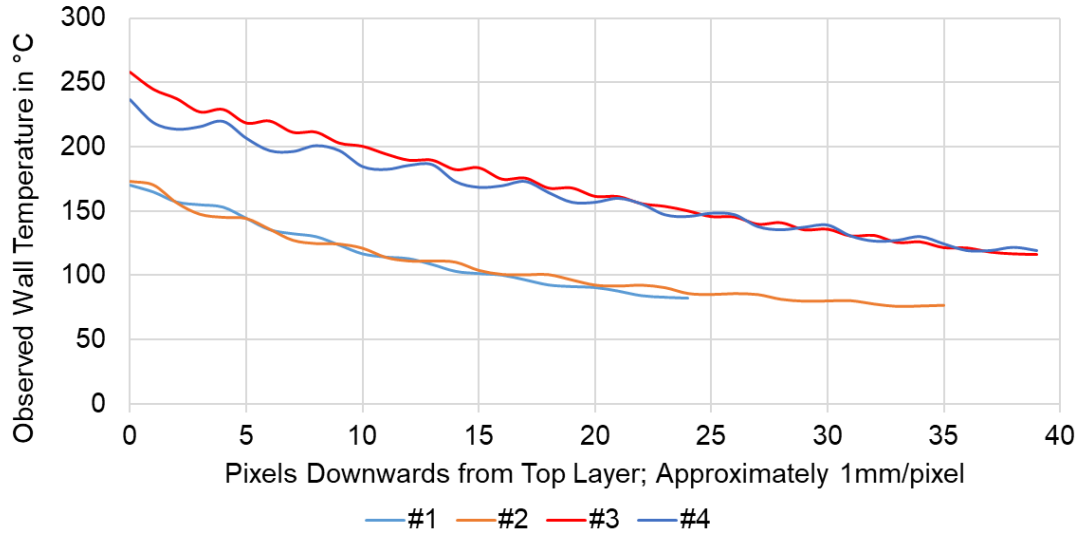

Figure 5-27: Temperature distribution in images of Figure 5-26 from top layer down along Z

The difference of the readings of the surface by the IR camera and internal thermocouple, as shown in Figure 5-25, increases when transitioning below about 260 °C, at which point the internal thermocouple reading seems to plateau in the 300 to 400 W range before achieving higher temperatures at higher enthalpy deposition rates. This matches the measured onset of crystallisation during DSC, shown in the histogram of Figure 5-28, which could explain the relative increase in temperature of the thermocouple reading inside the material against the IR reading of the surface. Of the experiments, 18 showed crystallisation; for the remainder, it was fully suppressed.

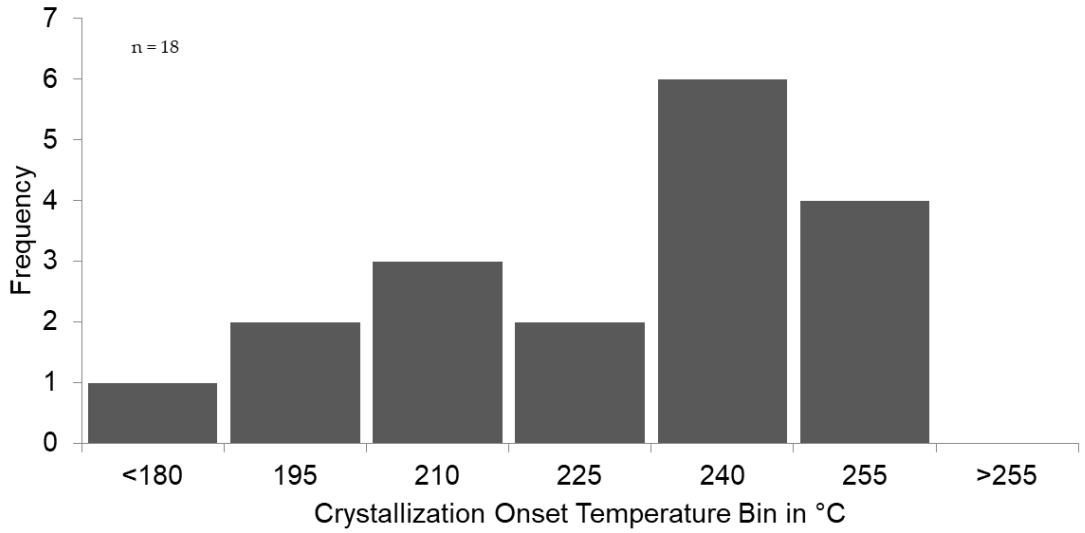

Figure 5-28: Crystallisation onset histogram in DSC measurements recreating experiment cooling rates

The DSC measurements also showed that the achieved crystallinity was highest for experiments where consecutive layers were deposited when the layer had cooled to temperatures slightly above the window of crystallisation onset. A higher layer temperature showed lower crystallinity, as is shown in Figure 5-29. This is likely due to the two-staged nature of crystal growth, with nucleation preceding crystal growth. Supercooling the melt causes a higher nucleation rate but decreases the crystal growth rate.

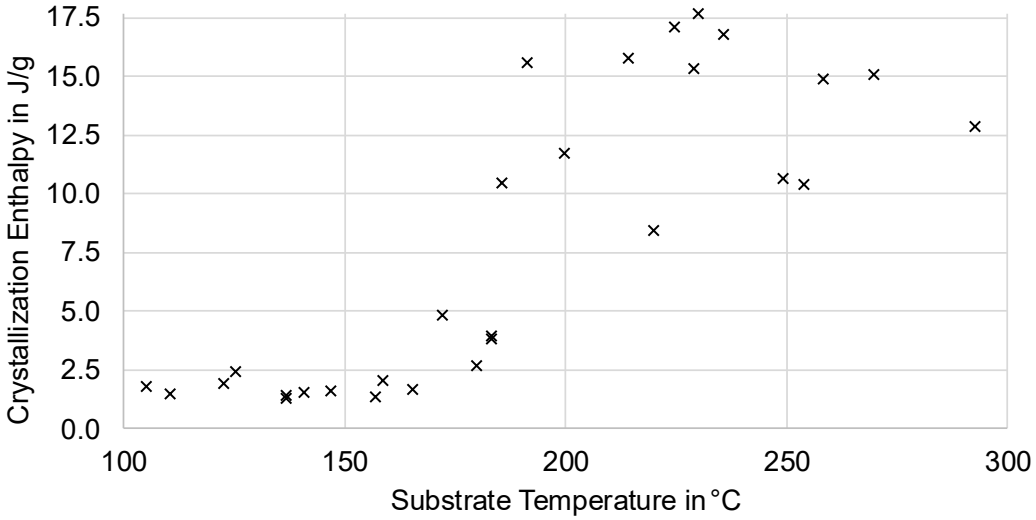

Figure 5-29: Crystallisation enthalpy over substrate temperature

An optimum for crystallisation seems to exist at which a supercooling to the crystallisation onset temperature causes a high nucleation rate and seeds crystals which can grow in the subsequent slower cooling phase. Higher layer temperature may either result in less nuclei being formed or nuclei being dissolved by the temperature increase caused by the deposition of the next layer. Another plausible explanation could be the increased formation of a higher enthalpy crystal phase, as indicated by the multiple melting peaks [136], [137], [138]. The crystallisation was almost suppressed if the layer had cooled below ~200 °C.

All specimens remained amorphous for at least 79 s after the consecutive layer was deposited, meaning all experiments happened under conditions where the material behaved as pseudo-amorphous as previously defined.

5.3.1.2 Mechanical Properties Matrix and Thermal History Dominated in Z

Three-point bending tests were used to confirm the effect of thermal history on the mechanical properties across the layer interface. As the substrate temperature depends strongly on the enthalpy deposition rate and substrate temperature influences strength and stiffness; a correlation between deposition power and mechanical properties was also found, as seen in Figure 5-30. However, as fusion bonding is also a time-dependent process, cooling rates from the substrate temperatures will also have an effect that is not captured by this metric.

A similar dependence was found for the determined modulus of the specimens. As fibres align mostly in the layer plane, this increase is expected to be due to a higher crystallinity of the matrix [139].

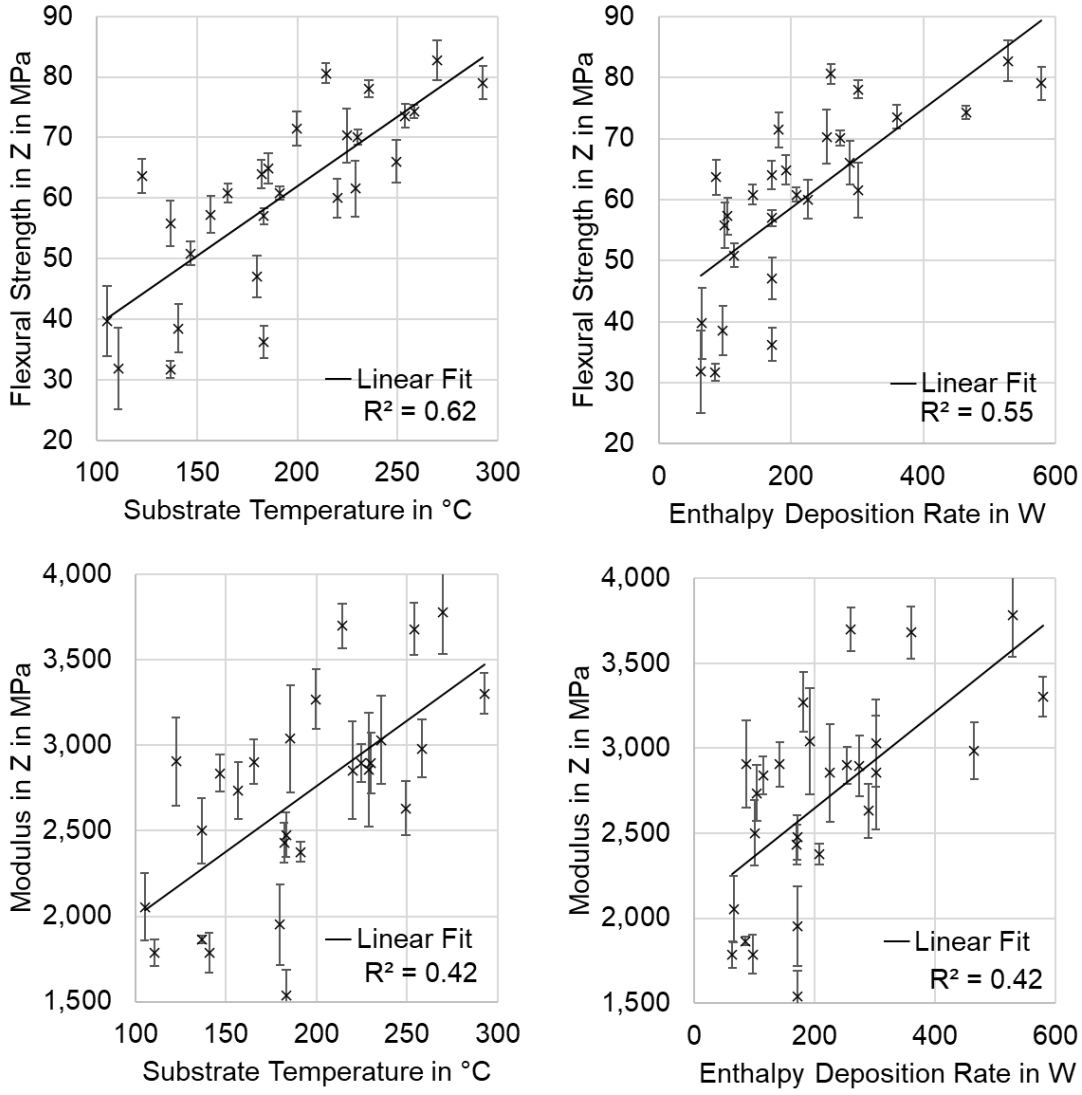

Figure 5-30: Three-point bending strength and modulus in Z over substrate temperature and enthalpy deposition rate

Figure 5-31 shows that samples with high crystallinity have high mechanical properties; however, the correlation is weak. Results above 70 MPa strength and 3000 MPa stiffness occurred only at high crystallinity. However, the presence of results with lower mechanical properties at high crystallinity indicates that other influencing factors are present.

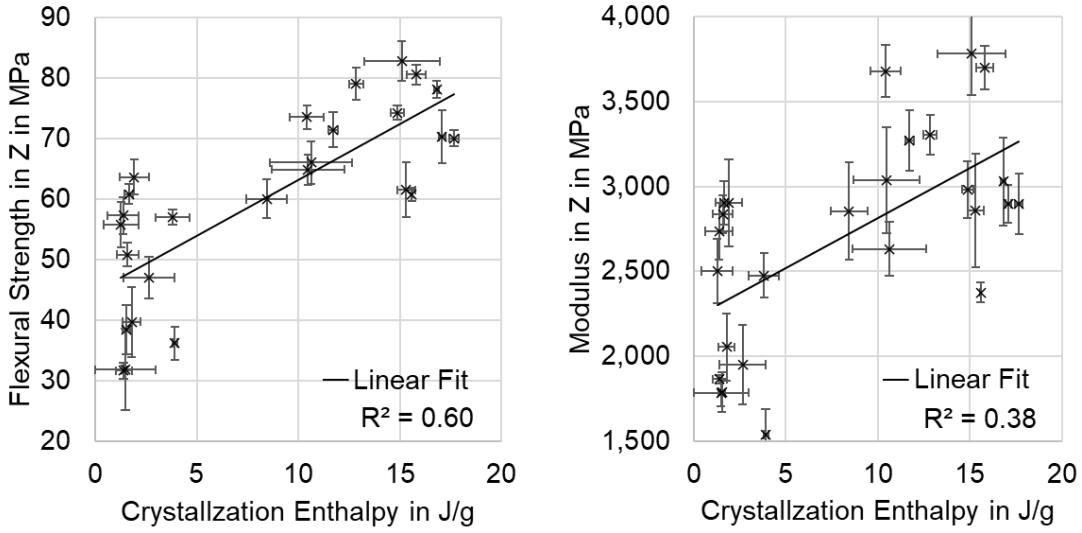

Figure 5-31: Strength and stiffness over crystallisation enthalpy

The healing model was applied to these experiments as well. However, it was unsuccessful in correlating the thermal history and cooling of the material to the achieved strength. The underlying problem is likely the measurement of the interface temperature. While overprinting, the thermocouple was pushed onto an already solidifying layer and overprinted with the melt. This means a large portion of the thermocouple surface is in contact with the fresh melt, and the reading is closer to the melt temperature. The temperature read when the consecutive layer was deposited was lower and correlated well with the strength after testing and the readings of the IR camera. However, this underestimates the contact temperature with the hot melt. Averaging the substrate and extrusion temperature resulted in values even higher than the readings of the thermocouple. The problem may be due again to the larger extrusion line dimension compared to the previous experiment.

While the model gave results that, in pair-wise comparison, gave a reasonable relation to the tested strength of individual parameter sets, no metric for the temperature was found for which a large portion of the results fitted well.

Figure 5-32 shows the test results over the interface temperature read by the thermocouple and the surface temperature, and the fitting of the mechanical relaxation time. While the substrate temperature is low, and most experiments should show no welding, the interface temperature is high, and all experiments should be fully healed. While the substrate temperature correlates strongly with the resulting flexural strength, the interface temperature does not.

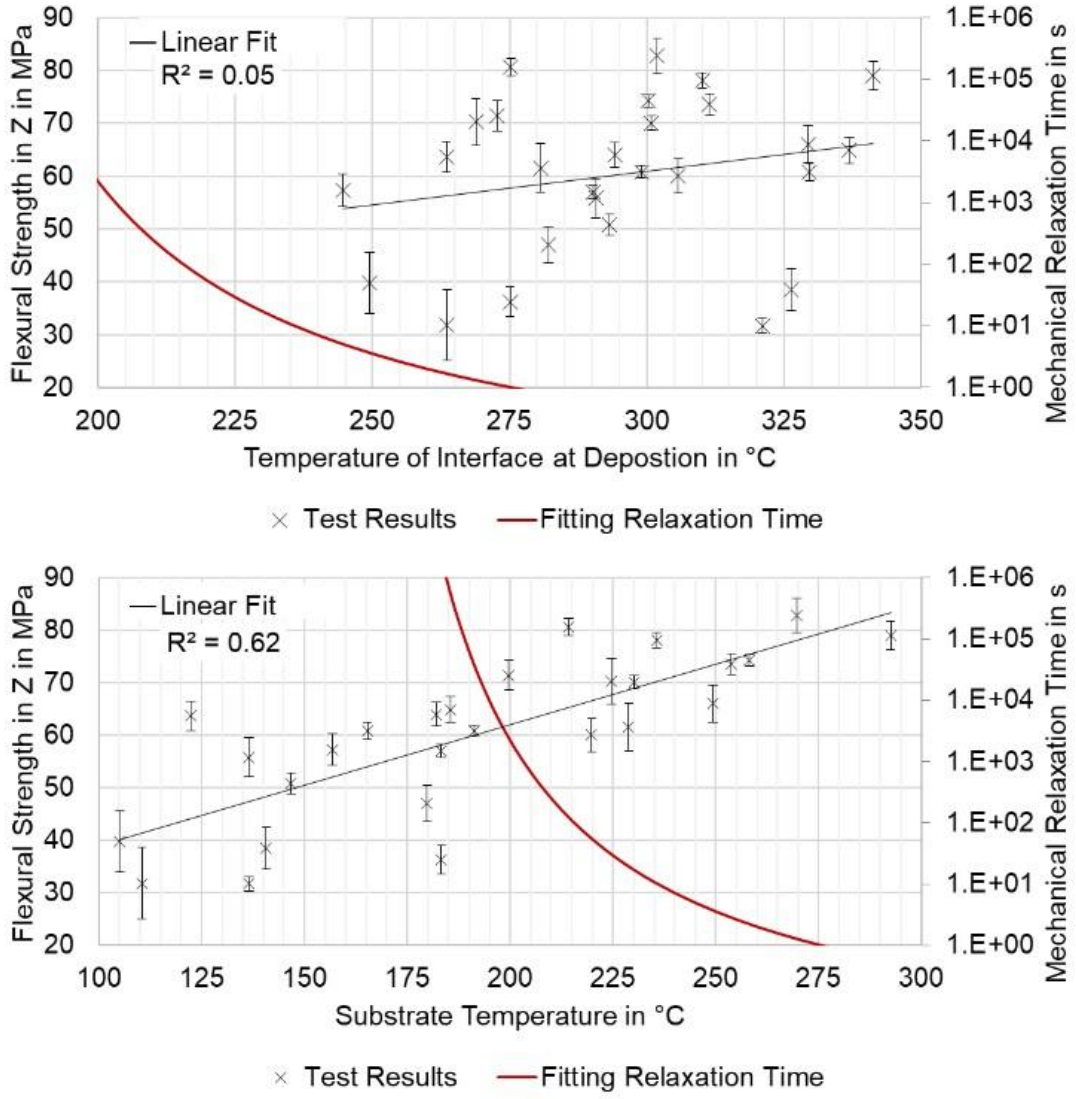

Figure 5-32: Test results over substrate and interface temperature with fitted mechanical relaxation time

The cooling rates measured by the embedded thermocouple when the melt was deposited were in the range of 44 to 123 K/min as the average cooling rate from deposition to the consecutive layer, even higher in the first moments after contact.

It is assumed that this quench cooling leads to very high-temperature gradients at the interface, possibly resulting in part of the molecular chains still being less mobile than the immediate contact surface. A microscopic simulation of the heat transfer from the melt into the layer below may yield a better understanding of the processes at play.

Overall, it can be concluded that higher deposition rates leading to higher processing temperatures improve the matrix-dominated material properties across the layers. However, there is a limitation to this. One of the experiments, with an extrusion temperature of 400 °C, line width of 12 mm, layer height of 4 mm, and layer time of 40 s, resulting in a deposition power of 579 W and a substrate layer temperature of 311 °C, was on the

limit of collapse and substrate layers were pushed aside during printing. Testing was only possible as the line width was high enough to machine deep enough into an uncompromised layer stack.

The part's thermal history during printing strongly influences the matrix material, affecting the welding process between the layers, the crystallisation, and the warping of the part. This temperature strongly correlates with the deposition power of the process, with different extrusion settings resulting in similar thermal conditions when the aggregates are similar. Higher deposition powers lead to higher substrate temperatures during deposition. This also suggests that the common approach of using a set layer time is invalid if the layer height or line width is changed.

Perpendicular to the layer plane, the matrix dominates the mechanical properties. The strength developed during the bonding of the layers through chain diffusion is a temperature-driven process. The substrate layer temperature during deposition is a key factor affecting the final part strength. Higher substrate temperatures strengthen bonding and improve mechanical performance [140], [141].

Layer temperature and cooling rates are also critical for the crystallisation behaviour, and the experiments demonstrate that higher layer temperatures lead to higher crystallinity. However, there is an optimum temperature range for crystallisation, and excessively high layer temperatures can result in lower degrees of crystallinity. Highly crystalline samples showed high stiffness compared to samples with low crystallinity.

AM materials with a slower crystallisation kinetic and quasi-amorphous behaviour, like the investigated PAEK material, show significantly enhanced strength between layers compared to materials designed for injection moulding with faster crystallisation kinetics [142], [143]. For end-use applications, crystallisation must be completed to ensure the desired material properties. Yet, the experiments have shown that for a wide range of layer temperatures, a high degree of crystallinity can be reached [144], [145]. This would make post-processing annealing necessary. The transition to full suppression is fast when the material cools fast enough to affect the crystallinity developed.

5.3.2 Conclusion for Hypothesis 3

The third hypothesis proposed that pseudo-amorphous polymers could achieve interlayer bonding at temperatures below the melting point, provided that cooling rates were sufficiently high to delay crystallisation. The sub-hypothesis asserted that the onset of crystallisation would determine the threshold for bonding and that bonding would persist as long as crystallisation was suppressed. This chapter aimed to evaluate whether the bonding dynamics during MEX are governed primarily by the suppression of crystallisation and to quantify the effect of cooling rates on interlayer fusion.

The experimental results support the core premise of the hypothesis. Thermal history measurements confirmed that the substrate temperature during deposition, influenced by the enthalpy deposition rate, critically affects interlayer bonding. It was observed that high cooling rates, particularly during the quench-cooling phase, delayed the onset of crystallisation, resulting in extended diffusion times for polymer chains across layer interfaces. This was further evidenced by the suppression of crystallisation in experiments where the layer cooled below the crystallisation window at rates exceeding the critical cooling threshold.

The DSC analysis validated that the crystallisation onset was effectively delayed for the PAEK material used. The polymer exhibited pseudo-amorphous behaviour in such conditions, allowing for significant healing. Importantly, even at temperatures substantially below the melting point, molecular diffusion occurred, supporting the sub-hypothesis that the onset of crystallisation serves as a limiting factor for interlayer bonding.

The mechanical testing results corroborated this finding, with specimens printed at higher substrate temperatures and faster cooling rates demonstrating improved flexural strength in the Z-direction. Even though the specimens' temperatures all fell within the crystallisation window, the interlayer strength achieved up to 82.7 MPa, indicating substantial molecular entanglement.

The comparison of thermocouple and IR camera measurements highlighted a key limitation: the difficulty in accurately capturing the true interface temperature during deposition. The disparity between surface and internal temperature readings, particularly near the crystallisation window, suggests that significant temperature gradients exist within the material. This may partially explain the variance in mechanical performance, as localised regions within the bond interface could experience different cooling and diffusion conditions.

Overall, the findings validate Hypothesis 3 and its sub-hypothesis. The experimental evidence confirms that pseudo-amorphous polymers can achieve robust interlayer bonding at temperatures below their melting point if cooling rates are sufficient to delay crystallisation. The onset of crystallisation can serve as a critical threshold, beyond which molecular diffusion ceases and can be effectively suppressed by slow crystallisation kinetics for pseudo-amorphous material behaviour. By optimising cooling rates and deposition power, the interlayer bonding process can be extended, leading to enhanced mechanical performance. However, the results also underscore the need for precise thermal control and monitoring.

These results contribute to the broader understanding of MEX process-property relationships and highlight the potential for tailoring cooling profiles to optimise bonding in high-performance polymers. Future work should focus on refining in-situ thermal measurements and developing predictive models that account for internal temperature gradients to further enhance control over interlayer bonding and crystallisation dynamics.

6 Discussion

6.1 Linking Theory and Experimental Findings

The relationship between the theoretical framework and the experimental findings highlights the critical role of material flow, crystallisation, and interlayer bonding dynamics in influencing MEX-produced parts' mechanical performance. This chapter integrates key theoretical considerations introduced in chapter 3 Theoretical Considerations with the experimental results outlined in 5 Experimental Results and Discussion, reinforcing the validity of the hypotheses and providing insights into process and machine optimisation potentials.

The theoretical predictions based on Jeffery's equation provided a robust foundation for understanding fibre alignment behaviour during material extrusion. The hypothesis that shear rates primarily govern fibre alignment at the extrusion nozzle was substantiated through empirical evidence. The experimental results for FFF demonstrated clear correlations between extrusion parameters and fibre orientation, with distinct flow regimes corresponding to convex, concave, and jagged extrusion line shapes.

Convex extrusion lines formed at shear rates below 23 s^{-1} displayed minimal fibre misalignment, confirming Jeffery's prediction that shearing flows align fibres parallel to the flow direction. Concave extrusion lines exhibited an inflexion point at approximately 23–70 s^{-1}, indicating transitional flow dynamics like swirling flow begin to influence fibre reorientation. Jagged extrusion lines at shear rates above 70 s^{-1} demonstrated chaotic flow conditions, contributing to highly randomised fibre orientations.

The significant increase in tensile strength (up to 70%) and modulus (117%) for samples with low misalignment highlights the mechanical impact of controlling shear rates within the optimal range. These findings align with prior studies on shear-driven fibre alignment, confirming that Jeffery's equation, despite its idealised assumptions, remains a valid predictor for MEX when shear rates are controlled within the observed thresholds.

However, deviations at higher shear rates suggest the influence of additional factors such as viscosity changes due to temperature variations and mechanical forces introduced possibly by the nozzle shearing the material between the layers below. There is a research gap left to account for non-linear shear effects in polymer-fibre composites.

In the LFAM experiments, where shear rates were significantly lower (<9.5 s^{-1}), the alignment trends persisted, however, with weaker correlations. This can be linked to the larger nozzle diameters and slower deposition speeds characteristic of LFAM, which reduced the magnitude of shear stresses. Nonetheless, the observed improvements in flexural strength and modulus in LFAM specimens at higher shear rates underscore the consistency of fibre alignment behaviour across scales, provided that the process temperature and material rheology are optimised.

The hypothesis that pseudo-amorphous polymers could achieve interlayer bonding at temperatures below their melting point if cooling rates were high enough to delay crystallisation was empirically validated. The DSC measurements showed a delayed crystallisation onset for SC-PAEK-CF20, confirming its suitability for maintaining molecular mobility during the bonding phase.

The measured cooling rates of 44 to 123 K/min successfully suppressed crystallisation in multiple specimens, maintaining pseudo-amorphous behaviour. In contrast, FC-PEEK-CF30 crystallised rapidly, resulting in negligible molecular diffusion across layer interfaces.

The fusion bonding model adapted from Butler et al.'s framework accurately captured the dynamic interplay between intimate contact and molecular diffusion. The mechanical relaxation time, derived from rheological measurements and modelled using the VFT relationship, provided a reliable approximation for predicting the welding time.

The experimentally determined VFT parameters for SC-PAEK and IC-PAEK reflected the expected trends in relaxation times:

The shorter relaxation times at higher temperatures supported faster bonding kinetics, achieving near-complete healing within seconds for FFF specimens. The extended relaxation times at lower temperatures illustrated the rapid deceleration of chain mobility, consistent with the theoretical limitations of healing when approaching the glass transition.

The resulting interlayer bonding strength in SC-PAEK-CF20 specimens reached 42.54% of the bulk polymer strength before crystallisation, closely aligning with the predicted degree of healing.

The observed pseudo-amorphous behaviour of SC-PAEK-CF20 at high cooling rates reinforces the theoretical proposition that suppressing nucleation extends the window for molecular diffusion. The polymer maintained interfacial chain mobility by preventing crystallisation during the critical bonding phase, achieving significant mechanical interlayer strength even at temperatures far below its melting point.

In LFAM, the slower cooling rates necessitated longer relaxation times, yet the thermal gradients recorded during layer deposition highlighted the challenge of achieving uni-

form bonding. The discrepancy between surface temperatures measured by infrared thermography and internal thermocouple readings suggests that localised quench-cooling effects may lead to more complex diffusion conditions than assumed initially.

This emphasises the importance of accurate control over temperatures during deposition, as even marginal changes in cooling rates can dictate whether the material retains sufficient chain mobility for effective diffusion. Post-processing annealing may be necessary to achieve uniform crystallinity when pseudo-amorphous behaviour occurs to optimise mechanical properties, as crystallisation is suppressed or reduced in most experiments.

6.2 Implications for Process and Machine Design

6.2.1 Process Design Consideration

The experimental findings and theoretical framework provide valuable guidance for optimising the MEX process to enhance mechanical performance. Key metrics such as shear and enthalpy deposition rates can fine-tune process parameters, balancing fibre alignment and interlayer bonding strength.

The shear rate during extrusion is pivotal in aligning fibres within the printed line. The results showed that shear rates resulted in highly aligned fibres along the flow direction, enhancing mechanical performance when kept inside the window where Jeffery's equation described flow. For this, the following guidelines can be recommended:

1. Minimise flow divergence: Avoid excessive expansion of the extrusion line width beyond the nozzle diameter to preserve fibre alignment along the extrusion direction.
2. Small extrusion lines and high print speeds: To maintain optimal shear rates, select a narrow line width close to the nozzle diameter and increase the print speed.
3. Avoid excessive shear: High shear rates lead to chaotic flow and fibre misalignment, which reduces strength and stiffness and results in rougher surfaces and even unstable extrusion.

By controlling these parameters, the process can achieve a high degree of fibre alignment and strength along X. Conversely, if more isotropic behaviour is required, large extrusion widths and low print speeds can create converging flow and induce random fibre orientations. This, however, comes at the expense of the properties along X and does not improve the properties along Y or Z.

The bond strength between layers is influenced by the substrate's temperature at the moment of contact with the subsequent layer, which depends strongly on the enthalpy deposition rate. Higher enthalpy deposition rates maintain higher substrate temperatures,

promoting interlayer diffusion. However, this must be managed to avoid overheating and slumping of the part. For this, the following guidelines can be recommended:

1. Maximise enthalpy deposition: Increase the deposition rate through either high extrusion temperatures, high deposition speed or larger extrusion lines.
2. Avoid overheating: Excessive enthalpy can lead to deformation, particularly in LFAM, where larger deposition lines can introduce high amounts of thermal energy.
3. Control layer time and temperature: Optimise layer times to prevent excessive cooling of the deposited layer while maintaining high enough cooling rates to delay crystallisation onset.

Both the shear and enthalpy deposition rates have been shown to positively impact the mechanical properties until they reach a tipping point at which behaviour changes. Extrusion lines change shape, and high substrate temperatures result in unstable parts. If these limits are known, the process can be optimised by maximising both metrics.

The results demonstrated that pseudo-amorphous polymers allow molecular diffusion at temperatures below the melting point. Materials with slower crystallisation kinetics provide a wider processing window for achieving bonding. This behaviour can be harnessed to extend layer completion times and maintain interlayer fusion:

A heated build chamber may help maintain a uniform substrate temperature, but further studies are needed to understand the interplay between chamber heating and the pseudo-amorphous behaviour. Fine-tuning these parameters could suppress crystallisation while maintaining the required interface temperature for optimal bonding.

The results of the LFAM fibre alignment measurements also suggest that similar to guidelines in injection moulding for maximum wall thickness, the extrusion line dimensions should be constrained to avoid excessive out-of-plane fibre misalignment: Avoid designs where the extrusion height and width result in a thick flow core, as this increases the likelihood of random fibre distribution. Implementing a maximum layer thickness should improve the predictability of fibre alignment and ensure uniform mechanical properties across the part.

6.2.2 Machine Development Potentials

Building on the process considerations, machine design enhancements can further support the optimisation of MEX through advanced temperature control, real-time monitoring, and active heating mechanisms. Implementing machine-level improvements ensures consistent bonding conditions and can complement the full potential of pseudo-amorphous materials.

An online process monitoring system that tracks real-time substrate temperatures can significantly improve process reliability. By correlating measured temperatures with predicted relaxation times and interface temperatures, the system ensures that bonding

occurs under optimal conditions and can provide real-time feedback. This approach offers early detection of deviations that could impact mechanical performance, enhancing quality assurance in small-scale and large-scale MEX applications.

Research has demonstrated the effectiveness of using active heating to raise the substrate temperature during layer deposition:

Some studies have shown that lasers positioned ahead of the nozzle can effectively increase substrate temperatures. This prevents excessive cooling and can heat the material beyond the melting point to facilitate interlayer diffusion [146], [147].

Similar experiments with IR emitters demonstrated that pre-heating the substrate, even if only by a small temperature difference, can improve bonding conditions and mechanical strength [148].

These methods can eliminate the critical challenge of balancing suppressing crystallisation and maintaining a sufficient interface temperature to support molecular diffusion. By reintroducing heat just before deposition, active heating systems enable the diffusion and even re-melt crystals that have formed.

An integrated system that combines real-time monitoring with active heating can substantially enhance MEX capabilities. When writing this chapter, the results had already been implemented to establish a company that develops such hardware, LEAM Technologies GmbH.

The system can adjust substrate heating dynamically in response to measured cooling rates, maintain consistent interface temperatures across complex geometries, and ensure that relaxation times are short, completing healing in fractions of a second.

This approach has been shown to improve layer bonding strength significantly in practice. Developing hardware that integrates real-time temperature tracking and active substrate heating has demonstrated substantial gains in interlayer strength, supporting its viability as a commercial solution. Such advancements pave the way for enhanced mechanical properties, even in high-performance fibre-reinforced polymers, by maintaining precise control over the thermal history during deposition, enabling the use of even fast crystallising materials, as shown in Figure 6-1.

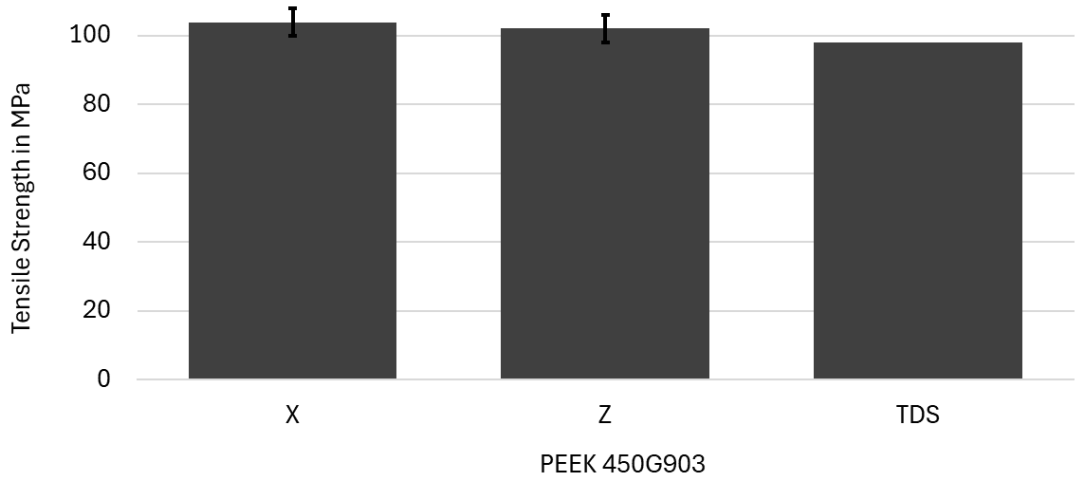

Figure 6-1: Achievable strength with machine enhancements

7 Conclusion and Outlook

7.1 Research Objectives in the Context of the State of the Art

This research aimed to advance the understanding of process-property relationships in MEX, focusing on the influence of material flow, crystallisation kinetics, and interlayer bonding dynamics on the mechanical performance of printed components. This work aimed to bridge the gap between theoretical modelling and practical process optimisation, addressing the persistent challenges of fibre misalignment, mechanical anisotropy, and insufficient interlayer adhesion that limit MEX's industrial adoption.

Compared to the state of the art, this dissertation provided a comprehensive approach that integrates flow dynamics, fibre orientation theory, and rheological models to predict and enhance mechanical properties. The results demonstrated that fibre alignment could be controlled through shear rate modulation as predicted by Jeffery's equation and that the mechanical relaxation time could be an accurate predictor for interlayer fusion bonding under non-isothermal conditions. Additionally, this study advanced the understanding of how pseudo-amorphous thermoplastics, particularly LM-PAEKs, can achieve high interlayer bonding strength at temperatures below their melting point through delayed crystallisation.

This research builds upon and extends current methodologies in MEX, contributing original insights into how material rheology and process parameters can be strategically manipulated to produce high-performance, fibre-reinforced parts.

7.2 Relevance and Originality of Findings

The findings of this study are highly relevant to academic research and industrial practice. The novel combination of Jeffery's theoretical framework for fibre alignment with experimental validation under MEX-specific flow conditions significantly contributes to understanding printed parts' anisotropic mechanical behaviour. The research also established that mechanical relaxation time, when modelled using the VFT relationship, provides accurate predictions of bonding strength across a range of temperatures and crystallisation conditions.

The exploration of LM-PAEK composites demonstrated that the crystallisation onset is a critical threshold for interlayer diffusion and molecular entanglement. This underscores the potential of slow-crystallising thermoplastics to extend the bonding window

during layer-by-layer deposition. Additionally, this work introduced practical guidelines for achieving optimal shear rates and enthalpy deposition rates, offering actionable recommendations for enhancing both small-scale and large-format MEX processes.

This research is original in its multi-scale approach, combining theoretical modelling, process optimisation, and industrial implementation. By demonstrating that material-specific process design can significantly improve the mechanical material properties, this dissertation lays the groundwork for improved process and machine design. It supports the broader application of MEX in high-performance sectors.

7.3 Materials and Methods

A significant contribution of this research is its focus on high-performance thermoplastics, particularly LM-PAEKs, which are gaining relevance in the AM sector and critical aerospace and medical applications. Due to their exceptional thermal and mechanical properties, these materials are considered promising candidates for next-generation composite matrix systems, with ongoing evaluations in European research programs such as Clean Sky for their potential use in lightweight aircraft structures.

The experiments conducted in this study used rheological and thermal analysis to characterise flow behaviour, crystallisation kinetics, and interlayer bonding strength. The methods employed ensured a highly detailed view of the material formation processes, allowing for robust validation of the proposed hypotheses. This research's materials and methods framework provides a reproducible approach for future studies to optimise MEX for structurally demanding applications.

7.4 Perspectives for Research Exploitation

This research has identified key academic opportunities for further exploration. One significant research gap relates to the non-linear shear effects observed at higher extrusion speeds, which warrants additional modelling and experimental validation. Further work could explore real-time monitoring approaches to precisely capture interface temperature variations and internal diffusion behaviour during deposition.

The progressing industrialisation of MEX opens new needs for research, such as material circularity, process standardisation for serial production, and the combination of MEX with other manufacturing techniques like subtractive and post-process surface treatments. These interdisciplinary efforts will be crucial for addressing the challenges of integrating MEX into broader manufacturing workflows.

By continuing to investigate these aspects, the research community can build upon the advancements presented here to enhance sustainability, efficiency, and versatility in AM.

In addition to academic exploration, the practical implications of this research have already extended into commercial development. The findings related to active heating strategies for improved thermal control have been directly applied to establish a company dedicated to developing and commercialising active heating hardware for MEX. The company has successfully brought these innovations to market, demonstrating the viability and impact of the proposed solutions.

This active heating system enhances interlayer bonding by maintaining optimal substrate temperatures during deposition, overcoming one of the key limitations of MEX for high-performance parts. The commercialisation of this technology underscores the potential for further industrial adoption, particularly in sectors such as aerospace, defence and energy, where mechanical reliability is paramount.

7.5 Resonance in the Research Community

The research presented in this dissertation has resonated within the AM community, contributing to ongoing discussions on improving mechanical performance and expanding the capabilities of material extrusion technologies. Publications from the underlying work have been cited, reflecting the interest and relevance of the findings among peers. Conference presentations have facilitated knowledge exchange and fostered collaborations with industry stakeholders and research institutions.

The experimental validation of theoretical models, combined with the practical demonstration of active thermal control, has positioned this research as a reference point for future studies on interlayer bonding and anisotropic mechanical behaviour in MEX. The engagement with large-scale projects, looking into aerospace tooling applications, further demonstrates this research's alignment with international efforts to advance sustainable and high-performance composite manufacturing.

In conclusion, this dissertation contributes to the field of MEX by addressing fundamental process-property challenges and proposing a cohesive framework for optimising MEX. The combination of theoretical insights, experimental validation, and industrial application emphasises the significance and applicability of this work, laying the groundwork for further innovations in high-performance AM.

References

[1] M. Quanjin, M. Rejab, M. S. Idris, N. M. Kumar, M. H. Abdullah, and G. R. Reddy, "Recent 3D and 4D intelligent printing technologies: A comparative review and future perspective," *Procedia Computer Science*, vol. 167, pp. 1210–1219, 2020, doi: 10.1016/j.procs.2020.03.434.

[2] C. Weller, R. Kleer, and F. T. Piller, "Economic implications of 3D printing: Market structure models in light of additive manufacturing revisited," *International Journal of Production Economics*, vol. 164, pp. 43–56, 2015, doi: 10.1016/j.ijpe.2015.02.020.

[3] D. L. Bourell, "Perspectives on Additive Manufacturing," *Annu. Rev. Mater. Res.*, vol. 46, no. 1, pp. 1–18, 2016, doi: 10.1146/annurev-matsci-070115-031606.

[4] M. Baumers, P. Dickens, C. Tuck, and R. Hague, "The cost of additive manufacturing: Machine productivity, economies of scale and technology-push," *Technological Forecasting and Social Change*, vol. 102, pp. 193–201, 2016, doi: 10.1016/j.techfore.2015.02.015.

[5] P. Zawadzki and K. Żywicki, "Smart Product Design and Production Control for Effective Mass Customization in the Industry 4.0 Concept," *Management and Production Engineering Review*, vol. 7, no. 3, pp. 105–112, 2016, doi: 10.1515/mper-2016-0030.

[6] K. Oettmeier and E. Hofmann, "Additive manufacturing technology adoption: an empirical analysis of general and supply chain-related determinants," *J Bus Econ*, vol. 87, no. 1, pp. 97–124, 2017, doi: 10.1007/s11573-016-0806-8.

[7] F. Wulle, D. Coupek, F. Schäffner, A. Verl, F. Oberhofer, and T. Maier, "Workpiece and Machine Design in Additive Manufacturing for Multi-Axis Fused Deposition Modeling," *Procedia CIRP*, vol. 60, pp. 229–234, 2017, doi: 10.1016/j.procir.2017.01.046.

[8] M. Merklein, D. Junker, A. Schaub, and F. Neubauer, "Hybrid Additive Manufacturing Technologies – An Analysis Regarding Potentials and Applications," *Physics Procedia*, vol. 83, pp. 549–559, 2016, doi: 10.1016/j.phpro.2016.08.057.

[9] D. Mathijsen, "Bigger, stronger, faster… pushing the envelope of 3D printers to turn them into true production tools," *Reinforced Plastics*, vol. 62, no. 4, pp. 194–202, 2018, doi: 10.1016/j.repl.2017.11.017.

[10] M. K. Thompson *et al.,* "Design for Additive Manufacturing: Trends, opportunities, considerations, and constraints," *CIRP Annals*, vol. 65, no. 2, pp. 737–760, 2016, doi: 10.1016/j.cirp.2016.05.004.

[11] W. Gao *et al.,* "The status, challenges, and future of additive manufacturing in engineering," *Computer-Aided Design*, vol. 69, pp. 65–89, 2015, doi: 10.1016/j.cad.2015.04.001.

[12] "3D Systems (DDD) - Market capitalization." Accessed: Dec. 22, 2024. [Online]. Available: https://companiesmarketcap.com/3d-systems/marketcap/

[13] "Stratasys (SSYS) - Market capitalization." Accessed: Dec. 22, 2024. [Online]. Available: https://companiesmarketcap.com/stratasys/marketcap/

[14] "Nano Dimension (NNDM) - Market capitalization." Accessed: Dec. 22, 2024. [Online]. Available: https://companiesmarketcap.com/nano-dimension/marketcap/

[15] *Additive Fertigung – Grundlagen – Terminologie*, DIN EN ISO/ASTM 52900, DIN Deutschen Institut für Normung e.V., Berlin, Jun. 2018.

[16] S. S. Crump, "APPARATUS AND METHOD FOR CREATING THREE-DIMENSIONAL OBJECTS," US5121329 (A), US19890429012 19891030, Sep 6, 1992.

[17] J. Gonzalez-Gutierrez, S. Cano, S. Schuschnigg, C. Kukla, J. Sapkota, and C. Holzer, "Additive Manufacturing of Metallic and Ceramic Components by the Material Extrusion of Highly-Filled Polymers: A Review and Future Perspectives," *Materials (Basel, Switzerland)*, early access. doi: 10.3390/ma11050840.

[18] M. Torrent, P. J. Gamez-Montero, and E. Codina, "Model of the Floating Bearing Bushing Movement in an External Gear Pump and the Relation to Its Parameterization," *Energies*, vol. 14, no. 24, p. 8553, 2021, doi: 10.3390/en14248553.

[19] D. I. Wimpenny, P. M. Pandey, and L. J. Kumar, *Advances in 3D Printing & Additive Manufacturing Technologies*. Singapore: Springer Singapore, 2017.

[20] S. Adamczak, J. Bochnia, and B. Kaczmarska, "An Analysis Of Tensile Test Results to Assess the Innovation Risk for an Additive Manufacturing Technology," *Metrology and Measurement Systems*, vol. 22, no. 1, p. 9, 2015, doi: 10.1515/mms-2015-0015.

[21] T. Hofstätter, D. Pedersen, G. Tosello, and H. Hansen, "Challenges and opportunities of fibre-reinforced polymers in additive manufacturing with focus on industrial applications," in *Joint Special Interest Group meeting between euspen and ASPE: Dimensional Accuracy and Surface Finish in Additive Manufacturing*, KU Leuven, BE, 2017.

[22] W. Oropallo and L. A. Piegl, "Ten challenges in 3D printing," *Engineering with Computers*, vol. 32, no. 1, pp. 135–148, 2016, doi: 10.1007/s00366-015-0407-0.

[23] A. Elser, M. Königs, A. Verl, and M. Servos, "On achieving accuracy and efficiency in Additive Manufacturing: Requirements on a hybrid CAM system," *Procedia CIRP*, vol. 72, pp. 1512–1517, 2018, doi: 10.1016/j.procir.2018.03.265.

[24] B. N. Turner and S. A. Gold, "A review of melt extrusion additive manufacturing processes: II. Materials, dimensional accuracy, and surface roughness," *Rapid Prototyping Journal*, vol. 21, no. 3, pp. 250–261, 2015, doi: 10.1108/RPJ-02-2013-0017.

[25] C. Moreau, "The State of 3D Printing 2021," [Online]. Available: https://info.sculpteo.com/hubfs/downloads/The%20State%20of%203D%20Printing%202021.pdf?_ga=2.156633660.688032419.1735221973-1221421945.1735221973

[26] "Additive manufacturing trend report 2021," [Online]. Available: https://f.hubspotusercontent10.net/hubfs/4075618/Additive%20manufacturing%20trend%20report%202021.pdf?_hsmi=82605589&_hsenc=p2ANqtz-8pVVH1TWB5lhXxlFFDFsuKkXC6nj7FtiZ-bBWqhdmdevavYK8SBIfKoMk5cy3L1VLE25pqHgBaoVd9k7TwJqX0iPykw67vd2Rk4WFcJMZRbkntIF6U

[27] E. N. Peters, "Plastics: Thermoplastics, Thermosets, and Elastomers," in *Handbook of Materials Selection*, M. Kutz, Ed., Wiley, 2002, pp. 335–355.

[28] N. Zirak, M. Shirinbayan, M. Deligant, and A. Tcharkhtchi, "Toward Polymeric and Polymer Composites Impeller Fabrication," *Polymers*, early access. doi: 10.3390/polym14010097.

[29] A. Chaplin, D. Thomas, U. Tahsin, and M. Riley, “COPOLYMERS AND PROCESS FOR THEIR MANUFACTURE,” EP3774991 (A1), EP20180715121 20180328, 2/17/2021.

[30] N. Yi, A. Chaplin, J. Grasmeder, and O. Ghita, "Adaptable polyaryletherketones (PAEKs) with competing crosslinking and crystallisation mechanisms," *Sci Rep*, early access. doi: 10.1038/s41598-024-51231-3.

[31] A. Chaplin, M. Riley, and U. Tahsin, “POLYMERIC MATERIAL, MANUFACTURE AND USE,” US2022064374 (A1), US202017420249 20200106, Mar 3, 2022.

[32] R. Reber, III, B. Koo, and D. Liu, "POLYETHERKETONEKETONE (PEKK), A VERSATILE ULTRA-POLYMER FOR ADDITIVE MANUFACTURING," vol. SAMPE Conference Proceedings. Charlotte, NC, May 20-23, 2019, 2019. [Online]. Available: https://digitallibrarynasampe.org/data/pdfs/s2019_pdfs/TP19--1596.pdf#:~:text=The%20T%2FI%20ratio%20of%20a%20PEKK%20copolymer%20affects,T%2FI%20ratios%20from%20about%2060%2F40%20to%20about%2080%2F20.

[33] J. Shang, P. Song, G. Li, Q. Sun, Y. Li, and Z. Wei, "Crystallization and melting behavior of poly(ether ketone ketone) (PEKK) copolymers synthesized by facile one-step method," *J Therm Anal Calorim*, vol. 148, no. 21, pp. 11727–11741,

2023. doi: 10.1007/s10973-023-12518-1. [Online]. Available: https://link.springer.com/article/10.1007/s10973-023-12518-1

[34] R. Androsch, C. Schick, and M. L. Di Lorenzo, "Kinetics of Nucleation and Growth of Crystals of Poly(l-lactic acid)," *Advances in Polymer Science*, vol. May 2017, 2017, doi: 10.1007/12_2016_13.

[35] Y. Shang *et al.,* "Slowing crystallization to enhance interlayer strength of 3D printed poly (ether ether ketone) parts by molecular design," *Additive Manufacturing*, vol. 59, p. 103104, 2022, doi: 10.1016/j.addma.2022.103104.

[36] C. L. Tucker III, *Fundamentals of Fiber Orientation: Description, measurement and prediction*. München: Carl Hanser Verlag GmbH & Co. KG, 2022. [Online]. Available: https://www.sciencedirect.com/science/book/9781569908754

[37] J. R. Sarasua, P. M. Remiro, and J. Pouyet, "The mechanical behaviour of PEEK short fibre composites," *Journal of Materials Science*, vol. 30, no. 13, pp. 3501–3508, 1995. doi: 10.1007/BF00349901. [Online]. Available: https://link.springer.com/article/10.1007/BF00349901

[38] O. Huseynov *et al.,* "Critical review on short fiber-reinforced composite materials manufactured by material extrusion: from thermal perspective," *Prog Addit Manuf*, vol. 10, no. 1, pp. 783–808, 2025. doi: 10.1007/s40964-024-00673-2. [Online]. Available: https://link.springer.com/article/10.1007/s40964-024-00673-2

[39] M. Feuchtgruber *et al.,* "Using carbon fiber tape to tailor the coefficient of thermal expansion in 3D-Printed composite tooling," *Journal of Thermoplastic Composite Materials*, 2024, Art. no. 08927057241264475, doi: 10.1177/08927057241264475.

[40] A. Vassilopoulos, Ed. *Proceedings of the 20th European Conference on Composite Materials - Composites Meet Sustainability (Vol 1-6)*. Lausanne, Lausann: EPFL Lausanne, Composite Construction Laboratory, 2022.

[41] G. D. Smith, C. J. Plummer, P.-E. Bourban, and J.-A. E. Månson, "Non-isothermal fusion bonding of polypropylene," *Polymer*, vol. 42, no. 14, pp. 6247–6257, 2001, doi: 10.1016/S0032-3861(01)00060-X.

[42] J. C. Antolin-Urbaneja, H. Vallejo Artola, E. Bellvert Rios, J. Gayoso Lopez, J. I. Hernández Vicente, and A. I. Luengo Pizarro, "Experimental Characterization of Screw-Extruded Carbon Fibre-Reinforced Polyamide: Design for Aeronautical Mould Preforms with Multiphysics Computational Guidance," *JMMP*, vol. 8, no. 1, p. 34, 2024, doi: 10.3390/jmmp8010034.

[43] S. Zaremba, "Composite Mould Based on 3D Printing—COMBO3D," *The Project Repository Journal*, vol. 11, no. 1, pp. 116–118, 2021, doi: 10.54050/PRJ1117715.

[44] G. Gardiner, "3D-printed CFRP tools for serial production of composite landing flaps," *CompositesWorld*, 28 Jun., 2023. Accessed: Dec. 25, 2024. [Online]. Available: https://www.compositesworld.com/articles/3d-printed-cfrp-tools-for-serial-production-of-composite-landing-flaps

[45] G. Gardiner, "ATLAM combines composite tape laying, large-scale thermoplastic 3D printing in one printhead," *CompositesWorld*, 21 Apr., 2023. Accessed: Dec. 26, 2024. [Online]. Available: https://www.compositesworld.com/news/atlam-combines-composite-tape-laying-large-scale-thermoplastic-3d-printing-in-one-printhead

[46] S. Rajendrachari, *Practical Implementations of Additive Manufacturing Technologies*. Singapore: Springer Nature Singapore, 2024.

[47] "center console carrier." Accessed: Dec. 26, 2024. [Online]. Available: https://akro-plastic.com/en/applications/center-console-carrier

[48] D. Sher, "Hans Weber receives SPE award for 3D printed automotive component," *VoxelMatters News*, 31 Jul., 2024. Accessed: Dec. 26, 2024. [Online]. Available: https://www.voxelmatters.com/hans-weber-receives-spe-award-for-3d-printed-automotive-component/

[49] Industrial Machinery. "Lightweighting robot grippers with additive manufacturing results in enhanced efficiency and sustainability - Industrial Machinery." Accessed: Dec. 26, 2024. [Online]. Available: https://blogs.sw.siemens.com/industrial-machinery/2024/07/18/lightweighting-robot-grippers-additive-manufacturing-webinar/#section_1

[50] R. C. Advincula, "3D Printing High Performance Polymers and the Oil and Gas Industry," *CORROSION 2019*, 2019.

[51] A. C. C. de Leon, Í. G. Da Silva, K. D. Pangilinan, Q. Chen, E. B. Caldona, and R. C. Advincula, "High performance polymers for oil and gas applications," *Reactive and Functional Polymers*, vol. 162, p. 104878, 2021. doi: 10.1016/j.reactfunctpolym.2021.104878. [Online]. Available: https://www.sciencedirect.com/science/article/pii/S1381514821000705

[52] REHAU Deutschland. "smartAWASCHACHT: Die Schachtlösung, wenn es sonst keine Lösung gibt | REHAU Schachtlösungen." Accessed: Dec. 26, 2024. [Online]. Available: https://www.rehau.com/de-de/smartawaschacht

[53] M. Kizak, A. von Bartschikowski, A. Trauth, C. Heigl, and K. Drechsler, "Investigation of the Interfacial Fusion Bonding on Hybrid Additively Manufactured Components under Torsional Load," *Polymers*, early access. doi: 10.3390/polym16192719.

[54] N. Tagscherer, A. M. Bär, S. Zaremba, and K. Drechsler, "Mechanical Analysis of Parameter Variations in Large-Scale Extrusion Additive Manufacturing of Thermoplastic Composites," *JMMP*, vol. 6, no. 2, p. 36, 2022, doi: 10.3390/jmmp6020036.

[55] *PEEK Biomaterials Handbook*. Elsevier, 2019.

[56] M. Herzmann, "3D printing of individualized cranial PEEK implants – saving costs and following regulatory pathways," (491 Pages / Transactions on Additive Manufacturing Meets Medicine, Vol 3 No 1 (2021): Trans. AMMM), 2021, doi: 10.18416/AMMM.2021.2109491.

[57] C. Basgul, H. Spece, N. Sharma, F. M. Thieringer, and S. M. Kurtz, "Structure, properties, and bioactivity of 3D printed PAEKs for implant applications: A systematic review," *Journal of biomedical materials research. Part B, Applied biomaterials*, early access. doi: 10.1002/jbm.b.34845.

[58] N. Sharma, J. Zubizarreta-Oteiza, C. Tourbier, and F. M. Thieringer, "Can Steam Sterilization Affect the Accuracy of Point-of-Care 3D Printed Polyetheretherketone (PEEK) Customized Cranial Implants? An Investigative Analysis," *Journal of clinical medicine*, early access. doi: 10.3390/jcm12072495.

[59] Franz Bauer and Stefan Leonhardt, "Medical AM of High Performance Plastics at the Point-of-Care," *Trans. AMMM*, vol. 1, S1, 2019. [Online]. Available: https://www.journals.infinite-science.de/index.php/ammm/article/view/116

[60] D. Freitas, H. A. Almeida, H. Bártolo, and P. J. Bártolo, "Sustainability in extrusion-based additive manufacturing technologies," *Prog Addit Manuf*, vol. 1, 1-2, pp. 65–78, 2016. doi: 10.1007/s40964-016-0007-6. [Online]. Available: https://link.springer.com/article/10.1007/s40964-016-0007-6#Fig11

[61] D. Kazmer, A. M. Peterson, D. Masato, A. R. Colon, and J. Krantz, "Strategic cost and sustainability analyses of injection molding and material extrusion additive manufacturing," *Polymer Engineering & Science*, vol. 63, no. 3, pp. 943–958, 2023. doi: 10.1002/pen.26256. [Online]. Available: https://4spepublications.onlinelibrary.wiley.com/doi/10.1002/pen.26256

[62] A. Patti, "Challenges to Improve Extrusion-Based Additive Manufacturing Process of Thermoplastics toward Sustainable Development," *Macromolecular Rapid Communications*, early access. doi: 10.1002/marc.202400249.

[63] B. Aruanno, "EcoPrintAnalyzer: Assessing Sustainability in Material Extrusion Additive Manufacturing for Informed Decision-Making," *Sustainability*, vol. 16, no. 2, p. 615, 2024. doi: 10.3390/su16020615. [Online]. Available: https://www.mdpi.com/2071-1050/16/2/615

[64] J. Kattinger, T. Ebinger, R. Kurz, and C. Bonten, "Numerical simulation of the complex flow during material extrusion in fused filament fabrication," *Additive*

Manufacturing, vol. 49, p. 102476, 2022. doi: 10.1016/j.addma.2021.102476. [Online]. Available: https://www.sciencedirect.com/science/article/pii/S2214860421006254

[65] S. Bakrani Balani, H. Mokhtarian, T. Salmi, and E. Coatanéa, "Numerical simulation of the shear rate in the fused filament fabrication process of poly-ether-ether-ketone (PEEK)," *Prog Addit Manuf*, pp. 1–21, 2024. doi: 10.1007/s40964-024-00888-3. [Online]. Available: https://link.springer.com/article/10.1007/s40964-024-00888-3

[66] A. Bellini, S. Gu¨c¸eri, and M. Bertoldi, "Liquefier Dynamics in Fused Deposition," *Journal of Manufacturing Science and Engineering*, vol. 126, no. 2, pp. 237–246, 2004, doi: 10.1115/1.1688377.

[67] Y. G. Mittal, P. Kamble, G. Gote, Y. Patil, A. K. Mehta, and K. P. Karunakaran, "A novel analytical model for screw extrusion of thermoplastic ABS with emphasis on additive manufacturing," *Manufacturing Letters*, vol. 35, pp. 652–657, 2023. doi: 10.1016/j.mfglet.2023.08.054. [Online]. Available: https://www.sciencedirect.com/science/article/pii/S2213846323001116

[68] R. M. Griffith, "Fully Developed Flow in Screw Extruders. Theoretical and Experimental Study," *Ind. Eng. Chem. Fund.*, vol. 1, no. 3, pp. 180–187, 1962, doi: 10.1021/i160003a004.

[69] C. Abeykoon, A. L. Kelly, E. C. Brown, and P. D. Coates, "The effect of materials, process settings and screw geometry on energy consumption and melt temperature in single screw extrusion," *Applied Energy*, vol. 180, pp. 880–894, 2016. doi: 10.1016/j.apenergy.2016.07.014. [Online]. Available: https://www.sciencedirect.com/science/article/pii/S0306261916309552

[70] R. W. Nelson, D. Chan, B. Yang, and L. J. Lee, "Dynamic behavior of a single screw plasticating extruder part I: Experimental study," *Polymer Engineering & Science*, vol. 26, no. 2, pp. 144–151, 1986, doi: 10.1002/pen.760260206.

[71] G. Barera, S. Dul, and A. Pegoretti, "Screw Extrusion Additive Manufacturing of Carbon Fiber Reinforced PA6 Tools," *J. of Materi Eng and Perform*, vol. 32, no. 21, pp. 9579–9597, 2023. doi: 10.1007/s11665-023-08238-0. [Online]. Available: https://link.springer.com/article/10.1007/s11665-023-08238-0

[72] S.-C. Chen. "Performance of gear pumps in single screw plasticating extrusion process - ProQuest." Accessed: Jan. 1, 2025. [Online]. Available: https://www.proquest.com/openview/e43e7000484ac8372c477b87ef46ac22/1?pq-origsite=gscholar&cbl=18750&diss=y

[73] H. T. Pham and K. S. Hyun, "Gear pump assisted extrusion," *Polymer Engineering & Science*, vol. 32, no. 7, pp. 488–493, 1992, doi: 10.1002/pen.760320706.

[74] V. G. de Bie, M. A. Hulsen, and P. D. Anderson, "Finite Element Modeling of a Viscous Fluid Flowing through an External Gear Pump," *Macro Theory & Simulations*, vol. 30, no. 1, 2021, Art. no. 2000060. doi: 10.1002/mats.202000060. [Online]. Available: https://onlinelibrary.wiley.com/doi/full/10.1002/mats.202000060

[75] P. M. Schäfer, *Consolidation of carbon fiber reinforced polyamide 6 tapes using laser-assisted tape placement,* 1st ed. München: Verlag Dr. Hut, 2018.

[76] T. Mulholland, S. Goris, J. Boxleitner, T. Osswald, and N. Rudolph, "Process-Induced Fiber Orientation in Fused Filament Fabrication," *J. Compos. Sci.*, vol. 2, no. 3, p. 45, 2018, doi: 10.3390/jcs2030045.

[77] B. P. Heller, D. E. Smith, and D. A. Jack, "Planar deposition flow modeling of fiber filled composites in large area additive manufacturing," *Additive Manufacturing*, vol. 25, pp. 227–238, 2019. doi: 10.1016/j.addma.2018.10.031. [Online]. Available: https://www.sciencedirect.com/science/article/pii/S2214860418306651

[78] B. P. Heller, D. E. Smith, and D. A. Jack, "Effects of extrudate swell and nozzle geometry on fiber orientation in Fused Filament Fabrication nozzle flow," *Additive Manufacturing*, vol. 12, pp. 252–264, 2016. doi: 10.1016/j.addma.2016.06.005. [Online]. Available: https://www.sciencedirect.com/science/article/pii/S2214860416301166

[79] Z. Wang and D. E. Smith, "A Fully Coupled Simulation of Planar Deposition Flow and Fiber Orientation in Polymer Composites Additive Manufacturing," *Materials (Basel, Switzerland)*, early access. doi: 10.3390/ma14102596.

[80] Z. Wang, "A numerical study on the predicted fiber orientation of large area extrusion deposition additive manufactured composites," *Polym. Compos.*, vol. 43, no. 10, pp. 6862–6876, 2022, doi: 10.1002/pc.26731.

[81] Z. Wang and D. E. Smith, "Numerical analysis of screw swirling effects on fiber orientation in large area additive manufacturing polymer composite deposition," *Composites Part B: Engineering*, vol. 177, p. 107284, 2019. doi: 10.1016/j.compositesb.2019.107284. [Online]. Available: https://www.sciencedirect.com/science/article/pii/S1359836819307814

[82] G. B. Jeffery, "The motion of ellipsoidal particles immersed in a viscous fluid," *Proc. R. Soc. Lond. A*, vol. 102, no. 715, pp. 161–179, 1922, doi: 10.1098/rspa.1922.0078.

[83] P. Pibulchinda, E. Barocio, A. J. Favaloro, and R. B. Pipes, "Influence of printing conditions on the extrudate shape and fiber orientation in extrusion deposition additive manufacturing," *Composites Part B: Engineering*, vol. 261, p. 110793, 2023, doi: 10.1016/j.compositesb.2023.110793.

[84] A. McPherson, *Introduction to Macromolecular Crystallography,* 2nd ed. Hoboken, N.J: Wiley, 2009. [Online]. Available: https://onlinelibrary.wiley.com/doi/book/10.1002/9780470391518

[85] O. Schwarz, F. W. Ebeling, H. Huberth, F. Richter, H. Schirber, and N. Schlör, *Kunststoffkunde: Aufbau, Eigenschaften, Verarbeitung, Anwendungen der Thermoplaste, Duroplaste und Elastomere,* 10th ed. Würzburg: Vogel Business Media, 1987. [Online]. Available: https://ebooks.ciando.com/book/index.cfm/bok_ID/2007045

[86] N. Kocic, "Bestimmung des Keimbildungsexponenten für die Kristallisation von Polymeren durch nicht-isotherme DSC-Analysen: Doctoralthesis," Universität Würzburg. [Online]. Available: https://opus.bibliothek.uni-wuerzburg.de/frontdoor/index/index/docId/11395

[87] C. R. Choe and K. H. Lee, "Nonisothermal crystallization kinetics of poly(etheretherketone) (PEEK)," *Polym. Eng. Sci.*, vol. 29, no. 12, pp. 801–805, 1989, doi: 10.1002/pen.760291208.

[88] *Polyamide* (Kunststoff-Handbuch / Hrsg. Gerhard W. Becker 3, Technische Thermoplaste / hrsg. von Ludwig Bottenbruch 4). München: Hanser, 1998.

[89] H. W. Starkweather and R. E. Brooks, "Effect of spherulites on the mechanical properties of nylon 66," *J. Appl. Polym. Sci.*, vol. 1, no. 2, pp. 236–239, 1959, doi: 10.1002/app.1959.070010214.

[90] L. H. Sperling, *Introduction to Physical Polymer Science*. Hoboken, NJ: Wiley, 2005. [Online]. Available: https://onlinelibrary.wiley.com/doi/book/10.1002/0471757128

[91] C. N. Velisaris and J. C. Seferis, "Crystallization kinetics of polyetheretherketone (peek) matrices," *Polym. Eng. Sci.*, vol. 26, no. 22, pp. 1574–1581, 1986, doi: 10.1002/pen.760262208.

[92] A. T. Lorenzo, M. L. Arnal, J. Albuerne, and A. J. Müller, "DSC isothermal polymer crystallization kinetics measurements and the use of the Avrami equation to fit the data: Guidelines to avoid common problems," *Polymer Testing*, vol. 26, no. 2, pp. 222–231, 2007, doi: 10.1016/j.polymertesting.2006.10.005.

[93] J. Zhang *et al.,* "The effect of cooling rates on crystallization and low-velocity impact behaviour of carbon fibre reinforced poly(aryl ether ketone) composites," *Composites Part B: Engineering*, vol. 254, p. 110569, 2023. doi: 10.1016/j.compositesb.2023.110569. [Online]. Available: https://www.sciencedirect.com/science/article/pii/S1359836823000720

[94] G. W. Ehrenstein, *Faserverbund-Kunststoffe: Werkstoffe - Verarbeitung - Eigenschaften,* 2nd ed. München, Wien: Hanser, 2006.

[95] J. R. Sarasua, P. M. Remiro, and J. Pouyet, "Effects of thermal history on mechanical behavior of PEEK and its short-fiber composites," *Polym. Compos.*, vol. 17, no. 3, pp. 468–477, 1996. doi: 10.1002/pc.10635. [Online]. Available: https://4spepublications.onlinelibrary.wiley.com/doi/10.1002/pc.10635

[96] K. Yang and Y. Zhao, "Interfacial crystallization behavior and properties of T1100-grade carbon fiber reinforced PEEK composites," *Composites Communications*, vol. 52, p. 102133, 2024. doi: 10.1016/j.coco.2024.102133. [Online]. Available: https://www.sciencedirect.com/science/article/pii/S2452213924003243

[97] L. Martineau, F. Chabert, B. Boniface, and G. Bernhart, "Effect of interfacial crystalline growth on autohesion of PEEK," *International Journal of Adhesion and Adhesives*, vol. 89, pp. 82–87, 2019. doi: 10.1016/j.ijadhadh.2018.11.013. [Online]. Available: https://www.sciencedirect.com/science/article/pii/S0143749618302720

[98] T. Ozawa, "Kinetics of non-isothermal crystallization," *Polymer*, vol. 12, no. 3, pp. 150–158, 1971. doi: 10.1016/0032-3861(71)90041-3. [Online]. Available: https://www.sciencedirect.com/science/article/pii/0032386171900413

[99] P. Sajkiewicz, L. Carpaneto, and A. Wasiak, "Application of the Ozawa model to non-isothermal crystallization of poly(ethylene terephthalate)," *Polymer*, vol. 42, no. 12, pp. 5365–5370, 2001, doi: 10.1016/S0032-3861(00)00934-4.

[100] M. C. Tobin, "Theory of phase transition kinetics with growth site impingement. I. Homogeneous nucleation," *J. Polym. Sci. Polym. Phys. Ed.*, vol. 12, no. 2, pp. 399–406, 1974. doi: 10.1002/pol.1974.180120212. [Online]. Available: https://onlinelibrary.wiley.com/doi/10.1002/pol.1974.180120212?msockid=2ddb791f72ee6f5c05f26d9173426e30

[101] K. Nakamura, T. Watanabe, K. Katayama, and T. Amano, "Some aspects of nonisothermal crystallization of polymers. I. Relationship between crystallization temperature, crystallinity, and cooling conditions," *J. Appl. Polym. Sci.*, vol. 16, no. 5, pp. 1077–1091, 1972, doi: 10.1002/app.1972.070160503.

[102] M. C. Tobin, "The theory of phase transition kinetics with growth site impingement. II. Heterogeneous nucleation," *Journal of Polymer Science: Polymer Physics Edition*, vol. 14, no. 12, pp. 2253–2257, 1976, doi: 10.1002/pol.1976.180141210.

[103] M. C. Tobin, "Theory of phase transition kinetics with growth site impingement. III. Mixed heterogeneous–homogeneous nucleation and nonintegral exponents of the time," *Journal of Polymer Science: Polymer Physics Edition*, vol. 15, no. 12, pp. 2269–2270, 1977, doi: 10.1002/pol.1977.180151217.

[104] A. Hammami and A. K. Mehrotra, "Re-examination of a proposed model for nonisothermal crystallization kinetics," *Polym. Eng. Sci.*, vol. 35, no. 2, pp. 170–172, 1995, doi: 10.1002/pen.760350208.

[105] R. Ledesma, C. Wohl, and B. Grimsley, "Crystallization kinetics analysis and modeling of aerospace PAEK materials," *Polymer Engineering & Science*, vol. 64, no. 8, pp. 3802–3816, 2024, doi: 10.1002/pen.26813.

[106] J. Cantrell *et al.,* "Experimental Characterization of the Mechanical Properties of 3D Printed ABS and Polycarbonate Parts," in *Advancement of Optical Methods in Experimental Mechanics, Volume 3: Proceedings of the 2016 Annual Conference on Experimental and Applied Mechanics* (Conference Proceedings of the Society for Experimental Mechanics Series), S. Yoshida, L. Lamberti, and C. Sciammarella, Eds., Cham, s.l.: Springer International Publishing, 2017, pp. 89–105.

[107] A. Bellini and S. Güçeri, "Mechanical characterization of parts fabricated using fused deposition modeling," *Rapid Prototyping Journal*, vol. 9, no. 4, pp. 252–264, 2003, doi: 10.1108/13552540310489631.

[108] C. A. Butler, R. L. Mccullough, R. Pitchumani, and J. W. Gillespie, "An Analysis of Mechanisms Governing Fusion Bonding of Thermoplastic Composites," *Journal of Thermoplastic Composite Materials*, vol. 11, no. 4, pp. 338–363, 1998, doi: 10.1177/089270579801100404.

[109] P. Dara and A. Loos, "Thermoplastic matrix composite processing model," 1985. [Online]. Available: https://www.semanticscholar.org/paper/Thermoplastic-matrix-composite-processing-model-Dara-Loos/b935691d33c125688392f6a62af3d085d3f87a86

[110] W. I. Lee and G. S. Springer, "A Model of the Manufacturing Process of Thermoplastic Matrix Composites," *Journal of Composite Materials*, vol. 21, no. 11, pp. 1017–1055, 2016, doi: 10.1177/002199838702101103.

[111] S. C. Mantell and G. S. Springer, "Manufacturing Process Models for Thermoplastic Composites," *Journal of Composite Materials*, vol. 26, no. 16, pp. 2348–2377, 1992, doi: 10.1177/002199839202601602.

[112] F. Yang and R. Pitchumani, "A fractal Cantor set based description of interlaminar contact evolution during thermoplastic composites processing," *Journal of Materials Science*, 2001. [Online]. Available: https://www.semanticscholar.org/paper/A-fractal-Cantor-set-based-description-of-contact-Yang-Pitchumani/04cb14e6877d13b27d73511c4207373d93d8916d

[113] F. Yang and R. Pitchumani, "Interlaminar contact development during thermoplastic fusion bonding," *Polym. Eng. Sci.*, vol. 42, no. 2, pp. 424–438, 2002, doi: 10.1002/pen.10960.

[114] P. G. de Gennes, "Reptation of a Polymer Chain in the Presence of Fixed Obstacles," *The Journal of Chemical Physics*, vol. 55, no. 2, pp. 572–579, 1971, doi: 10.1063/1.1675789.

[115] M. Doi and S. Edwards, *The theory of polymer dynamics*, 1986.

[116] O. A. Ezekoye, C. D. Lowman, M. T. Fahey, and A. G. Hulme-Lowe, "Polymer weld strength predictions using a thermal and polymer chain diffusion analysis," *Polym. Eng. Sci.*, vol. 38, no. 6, pp. 976–991, 1998, doi: 10.1002/pen.10266.

[117] F. Yang and R. Pitchumani, "Healing of Thermoplastic Polymers at an Interface under Nonisothermal Conditions," *Macromolecules*, vol. 35, no. 8, pp. 3213–3224, 2002, doi: 10.1021/ma010858o.

[118] R. P. Wool, "Polymer diffusion: Reptation and interdigitation," *Handbook of Adhesion: Second Edition*, pp. 341–344, 2005, doi: 10.1002/0470014229.ch15.

[119] D. Grewell and A. Benatar, "Welding of Plastics: Fundamentals and New Developments," *IPP*, vol. 22, no. 1, pp. 43–60, 2007, doi: 10.3139/217.0051.

[120] R. P. Wool, "Polymer entanglements," *Macromolecules*, vol. 26, no. 7, pp. 1564–1569, 1993, doi: 10.1021/ma00059a012.

[121] D. Parisi, J. Seo, R. P. Schaake, A. M. Rhoades, and R. H. Colby, "Shear-induced nematic phase in entangled rod-like PEEK melts," *Progress in Polymer Science*, vol. 112, p. 101323, 2021. doi: 10.1016/j.progpolymsci.2020.101323. [Online]. Available: https://www.sciencedirect.com/science/article/pii/S0079670020301167

[122] P. G. de Gennes and L. Leger, "Dynamics of Entangled Polymer Chains," *Annu. Rev. Phys. Chem.*, vol. 33, no. 1, pp. 49–61, 1982, doi: 10.1146/annurev.pc.33.100182.000405.

[123] T. G. Mezger, *The Rheology Handbook: 4th Edition,* 4th ed. (European Coatings TECH FILES). Hannover: Vincentz Network, 2014.

[124] J. D. Ferry, *Viscoelastic properties of polymers,* 3rd ed. New York, Chichester: Wiley, 1980.

[125] J. Bartolai, T. W. Simpson, and R. Xie, "Predicting strength of additively manufactured thermoplastic polymer parts produced using material extrusion," *Rapid Prototyping Journal*, vol. 24, no. 2, pp. 321–332, 2018.

[126] J. F. Vega, S. Rastogi, G. W. M. Peters, and H. E. H. Meijer, "Rheology and reptation of linear polymers. Ultrahigh molecular weight chain dynamics in the melt," *Journal of Rheology*, vol. 48, no. 3, pp. 663–678, 2004, doi: 10.1122/1.1718367.

[127] M. L. Mansfield, "Model of the glass transition," *The Journal of Chemical Physics*, vol. 103, no. 18, pp. 8124–8129, 1995, doi: 10.1063/1.470176.

[128] H. Vogel, "Das Temperaturabhangigkeitsgesetz der Viskositat von Flussigkeiten," *Physikalische Zeitschrift*, vol. 22, pp. 645–646, 1921. [Online]. Available: https://typeset.io/papers/das-temperaturabhangigkeitsgesetz-der-viskositat-von-obv8n2b6s2

[129] Garca-Coln, C. L. F. del, and Goldstein, "Theoretical basis for the Vogel-Fulcher-Tammann equation," *Physical review. B, Condensed matter*, vol. 40, no. 10, pp. 7040–7044, 1989, doi: 10.1103/physrevb.40.7040.

[130] C. M. Stokes-Griffin, S. Ehard, A. Kollmannsberger, P. Compston, and K. Drechsler, "A laser tape placement process for selective reinforcement of steel with CF/PA6 composites: Effects of surface preparation and laser angle," *Materials & Design*, vol. 116, pp. 545–553, 2017, doi: 10.1016/j.matdes.2016.12.013.

[131] P. Consul, K.-U. Beuerlein, G. Luzha, and K. Drechsler, "Effect of Extrusion Parameters on Short Fiber Alignment in Fused Filament Fabrication," *Polymers*, early access. doi: 10.3390/polym13152443.

[132] P. Consul, M. Feuchtgruber, B. Bauer, and K. Drechsler, "Influence of Extrusion Parameters on the Mechanical Properties of Slow Crystallizing Carbon Fiber-Reinforced PAEK in Large Format Additive Manufacturing," *Polymers*, early access. doi: 10.3390/polym16162364.

[133] P. Consul, A. Chaplin, N. Tagscherer, S. Zaremba, and K. Drechsler, "Interlaminar strength in large-scale additive manufacturing of slow crystallizing polyaryletherketone carbon composites," *Polym Int*, 2020, doi: 10.1002/pi.6168.

[134] R. Davies, N. Yi, P. McCutchion, and O. Ghita, "Mechanical property variance amongst vertical fused filament fabricated specimens via four different printing methods," *Polym Int*, vol. 70, no. 8, pp. 1073–1079, 2021, doi: 10.1002/pi.6172.

[135] N. Dencheva, Z. Denchev, M. J. Oliveira, and S. S. Funari, "Relationship between crystalline structure and mechanical behavior in isotropic and oriented polyamide 6," *J. Appl. Polym. Sci.*, vol. 103, no. 4, pp. 2242–2252, 2007, doi: 10.1002/app.25250.

[136] Y. Wang, J. D. Beard, K. E. Evans, and O. Ghita, "Unusual crystalline morphology of Poly Aryl Ether Ketones (PAEKs)," *RSC Adv.*, vol. 6, no. 4, pp. 3198–3209, 2016, doi: 10.1039/c5ra17110e.

[137] Y. Wang, B. Chen, K. E. Evans, and O. Ghita, "Novel fibre-like crystals in thin films of Poly Ether Ether Ketone (PEEK)," *Materials Letters*, vol. 184, pp. 112–118, 2016, doi: 10.1016/j.matlet.2016.08.024.

[138] C. A. Comelli, N. Yi, R. Davies, H. van der Pol, and O. Ghita, "Material extrusion thermal model mapped across polyetheretherketone isothermal and continuous cooling transformation charts," *Additive Manufacturing*, vol. 59, p. 103129, 2022, doi: 10.1016/j.addma.2022.103129.

[139] X. Ma, L. Wen, S. Wang, J. Xiao, W. Li, and X. Hou, "Inherent relationship between process parameters, crystallization and mechanical properties of continuous carbon fiber reinforced PEEK composites," *Defence Technology*, vol. 24, pp. 269–284, 2023, doi: 10.1016/j.dt.2022.04.010.

[140] T. J. Coogan and D. O. Kazmer, "Prediction of interlayer strength in material extrusion additive manufacturing," *Additive Manufacturing*, vol. 35, p. 101368, 2020, doi: 10.1016/j.addma.2020.101368.

[141] N. Tagscherer, P. Consul, I. L. Kottenstedde, H. Latiri, S. Zaremba, and K. Drechsler, "Investigation of nonisothermal fusion bonding for extrusion additive manufacturing of large structural parts," *Polym. Compos.*, vol. 42, no. 10, pp. 5209–5222, 2021, doi: 10.1002/pc.26216.

[142] W. Wu, P. Geng, G. Li, Di Zhao, H. Zhang, and J. Zhao, "Influence of Layer Thickness and Raster Angle on the Mechanical Properties of 3D-Printed PEEK and a Comparative Mechanical Study between PEEK and ABS," *Materials (Basel, Switzerland)*, vol. 8, no. 9, pp. 5834–5846, 2015, doi: 10.3390/ma8095271.

[143] C.-Y. Liaw, J. W. Tolbert, L. W. Chow, and M. Guvendiren, "Interlayer bonding strength of 3D printed PEEK specimens," *Soft matter*, vol. 17, no. 18, pp. 4775–4789, 2021, doi: 10.1039/D1SM00417D.

[144] M. Pastorek and A. Kovalcik, "Effects of thermal annealing as polymer processing step on poly(lactic acid)," *Materials and Manufacturing Processes*, vol. 33, no. 15, pp. 1674–1680, 2018, doi: 10.1080/10426914.2018.1453153.

[145] G. Yeh, R. Hosemann, J. Loboda-Čačković, and H. Čačković, "Annealing effects of polymers and their underlying molecular mechanisms," *Polymer*, vol. 17, no. 4, pp. 309–318, 1976, doi: 10.1016/0032-3861(76)90187-7.

[146] T. Wang, P. Consul, D. Bublitz, and K. Drechsler, "CONTINUOUS DIRECTED LASER PREHEATING OF BIG AREA ADDITIVE MANUFACTURING," *INTERNATIONAL CONFERENCE ON COMPOSITE MATERIALS*, vol. 23, 2023. [Online]. Available: https://iccm-central.org/Proceedings/ICCM23proceedings/papers/ICCM23_Full_Paper_9.pdf

[147] P. Han, A. Tofangchi, S. Zhang, A. Desphande, and K. Hsu, "Effect of in-process laser interface heating on strength isotropy of extrusion-based additively manufactured PEEK," *Procedia Manufacturing*, vol. 48, pp. 737–742, 2020. doi: 10.1016/j.promfg.2020.05.107. [Online]. Available: https://www.sciencedirect.com/science/article/pii/S2351978920315596

[148] N. Tagscherer, T. A. Osswald, and K. Drechsler, "Targeted Temperature Manipulation and Analysis of the Influence on Mechanical Properties in Large-Scale Extrusion Additive Manufacturing," *Applied Sciences*, vol. 12, no. 6, p. 2998, 2022, doi: 10.3390/app12062998.

A Publications

Journal Articles

[P1] P. Consul, A. Chaplin, N. Tagscherer, S. Zaremba, and K. Drechsler, "Interlaminar strength in large-scale additive manufacturing of slow crystallizing polyaryletherketone carbon composites," *Polym Int*, 2020, doi: 10.1002/pi.6168.

[P2] P. Consul, K.-U. Beuerlein, G. Luzha, and K. Drechsler, "Effect of Extrusion Parameters on Short Fiber Alignment in Fused Filament Fabrication," *Polymers*, early access. doi: 10.3390/polym13152443.

[P3] N. Tagscherer, P. Consul, I. L. Kottenstedde, H. Latiri, S. Zaremba, and K. Drechsler, "Investigation of nonisothermal fusion bonding for extrusion additive manufacturing of large structural parts," *Polym. Compos.*, vol. 42, no. 10, pp. 5209–5222, 2021, doi: 10.1002/pc.26216.

[P4] M. Feuchtgruber *et al.,* "Using carbon fiber tape to tailor the coefficient of thermal expansion in 3D-Printed composite tooling," *Journal of Thermoplastic Composite Materials*, 2024, Art. no. 08927057241264475, doi: 10.1177/08927057241264475.

[P5] P. Consul, M. Feuchtgruber, B. Bauer, and K. Drechsler, "Influence of Extrusion Parameters on the Mechanical Properties of Slow Crystallizing Carbon Fiber-Reinforced PAEK in Large Format Additive Manufacturing," *Polymers*, early access. doi: 10.3390/polym16162364.

Conference Papers

[K1] Sommacal, S, A Kingston, M Ploeckl, A Matschinski, P Consul, M Saadatfar, and P Compston. “3D Characterisation of Carbon Fibre Reinforced Composite Microstructure via X-Ray Computed Tomography.” ICCM22 2019, 4157–4168. 2019. Melbourne, VIC: Engineers Australia, 2019. https://search.informit.org/doi/10.3316/informit.895357239249951.

[K2] P. Consul, A. Chaplin, and K. Drechsler, "Big Area Additive Manufacturing of a Thermoplastic Tooling for a Large Thermoset Composite Structure," in 2020. [Online]. Available: https://mediatum.ub.tum.de/1593642

[K3] T. Wang, P. Consul, D. Bublitz, and K. Drechsler, "CONTINUOUS DIRECTED LASER PREHEATING OF BIG AREA ADDITIVE MANUFACTURING," *INTERNATIONAL CONFERENCE ON COMPOSITE MATERIALS*, vol. 23, 2023. [Online]. Available: https://iccm-central.org/Proceedings/ICCM23proceedings/papers/ICCM23_Full_Paper_9.pdf

B Supervised Student Theses

As part of the work at the Chair of Carbon Composites, the supervision of the following student theses was supported.

[S1] O. Stoffels, ”Additive Fertigungsverfahren - Bestimmung der Kristallisationskinetik des Hochleistungsthermoplasten PEEK”, Bachelor Thesis, Chair of Carbon Composites, TUM, 2018

[S2] A. Eris, ”Klassifizierung von Werkstoffeigenschaften für Composites mittels Clusteranalyse”, Bachelor Thesis, Chair of Carbon Composites, TUM, 2018

[S3] M. Feuchtgruber, ”Rheological Investigation of the Reptation Time and the Influence of Crystallization on the Viscosity of PEEK”, Semester Thesis, Chair of Carbon Composites, TUM, 2018

[S4] M. Keßler, ”Additive Fertigungsverfahren - Material- und Prozesscharakterisierung für PEEK im Fused Filament Fabrication Verfahren”, Semester Thesis, Chair of Carbon Composites, TUM, 2018

[S5] C. Marxer, “Layer fusion of amorphous polymers in fused filament fabrication based 3D printing”, Master Thesis, Chair of Carbon Composites, TUM, 2019

[S6] Q. Chang, ”Mechanisches Verhalten von 3D Gedruckten Thermoplasten bei Hohen Temperaturen”, Semester Thesis, Chair of Carbon Composites, TUM, 2019

[S7] X. Zhang, ”Mechanical Behaviour of 3D Printed Thermoplastics at High Temperatures”, Semester Thesis, Chair of Carbon Composites, TUM, 2019

[S8] M. Keßler, ”Additive Manufacturing - Modification of a Desktop Fused Filament Fabrication 3D Printer for High Performance Polymers”, Master Thesis, Chair of Carbon Composites, TUM, 2019

[S9] N. Zhou, ”Thermische Polymerdegradation von 3D-Druckmaterialien”, Bachelor Thesis, Chair of Carbon Composites, TUM, 2019

[S10] N. Novello, ”Thermal and Electrical Metamaterials by 3D Printing”, Bachelor Thesis, Chair of Carbon Composites, TUM, 2019

[S11] R. Li, ”Inbetriebnahme eines Werkzeugoberflächenprüfstandes für 3D gedruckte Werkzeuge”, Semester Thesis, Chair of Carbon Composites, TUM, 2019

[S12] M. Mateo Guarch, “Extrusionsbasierte Additive Fertigung von Groß Skalierten Gitterstrukturen”, Bachelor Thesis, Chair of Carbon Composites, TUM, 2020

[S13] F. Rivero Porras, ”Experimental Investigation of Inserts in Additively Manufactured Aerospace Parts”, Bachelor Thesis, Chair of Carbon Composites, TUM, 2020

[S14] P. Markou, ”Marktwachstum, Entwicklungstrends & Neue Regulierungen in der Luftfahrtindustrie”, Semester Thesis, Chair of Carbon Composites, TUM, 2020

[S15] K. Beuerlein, ”Faserorientierung in Materialextrusion Basierter Additiver Fertigung”, Bachelor Thesis, Chair of Carbon Composites, TUM, 2020

[S16] G. Luzha, “Prozessinduzierte Faserorientierung in der Additiven Fertigung durch Material Extrusion”, Semester Thesis, Chair of Carbon Composites, TUM, 2021

[S117] J. Xu, ”Large-scale additive manufacturing for aerospace tooling”, Semester Thesis, Chair of Carbon Composites, TUM, 2021

[S18] J. Xu, ”Oberflächenbeschichtungen zur Verbesserung der Standzeit von additiv gefertigten Formwerkzeugen für die Luftfahrt”, Master Thesis, Chair of Carbon Composites, TUM, 2022

[S19] S. Teske, ”Design and Fabrication of Recyclable Addi-tive Manufactured Multi-Piece Moulds for Composite eVTOL Components”, Master Thesis in Cooperation with Volocopter, Chair of Carbon Composites, TUM, 2022

[S20] M. Plagmann, ”Untersuchung der Kristallmorphologie in 3D gedruckten Thermoplasten”, Master Thesis, Chair of Carbon Composites, TUM, 2023

[S15] and [S16] where part of the peer reviewed publication [131], that is part of this dissertation in chapters 4.3.1 and 5.1. Images were also taken from [S20].

C Curriculum Vitae

Patrick Consul

Researcher, Engineer & Founder in the field of large format additive manufacturing and a background in business administration, focused on operations & supply chain management. In-depth understanding of aerospace applications of large format additive manufacturing and material behavior affected by manufacturing process. Broad network of machine OEMs and users of large format additive manufacturing in European aerospace and automotive industry.

Munich, Germany **linkedin.com/in/patrick-consul/**

Work Experience

09/2022 – present	**Co-Founder and Chief Executive Officer** LEAM Technologies GmbH • LEAM provides innovative temperature management solutions that enable unprecedented material performance in additive manufacturing. • Responsible for strategy, finance, marketing and sales. • LEAM has been awarded with an “Exist Transfer of Research” grant, the “Gründungspreis – Digitale Innovationen 2023” award and has been accepted into the “Business Incubation Centre” of the European Space Agency.
04/2022 – 08/2022	**Development Engineer** KraussMaffei Technologies GmbH, AM Innovation Center • Responsible for system market readiness and digitalization roadmap definition for large format additive manufacturing machines. • Project acquisition with new partners. • Process development and CAM programming of machines for proof of concept prior to market introduction.
2/2017 – 04/2022	**Researcher** Technical University of Munich, Chair of Carbon Composites

	• Research development for Additive Manufacturing focused on large format additive manufacturing for aerospace and automotive applications. Project planning and successful acquisition of a 6 research projects with a total budget of 6,5 Mio €. • Machine and equipment procurement in accordance to German public sector budget law including specialized lab equipment and a CEAD AM Flexbot for large format additive manufacturing. · • Research topic lead for „Machine Design & Automation“ for a team of eight, coordinating the institutes research on machine component design, subsystem communication & integration and machine programming & path planning for composite manufacturing processes. • Project management of European research projects and consortium coordination with five partners in four countries including contract negotiations, technical & financial reporting, risk management and work package scheduling

EDUCATION

06/2018 – Acceptance of this dissertation	**Mechanical Engineering, PhD** Technical University of Munich Dissertation on „Process-Property Relationships in Material Extrusion Additive Manufacturing“
10/2014 – 09/2017	**Automotive Engineering, Master of Science** Technical University of Munich Specialization: Fiber Composites
10/2013 – 02/2017	**Management and Technology, Bachelor of Science** Technical University of Munich Specialization: Operations & Supply Chain Management
10/2011 – 04/2015	**Mechanical Engineering & Management, Bachelor of Science** Technical University of Munich
09/2003 – 06/2011	Colegio Andino – German School Bogotá, Colombia Graduation: German Abitur